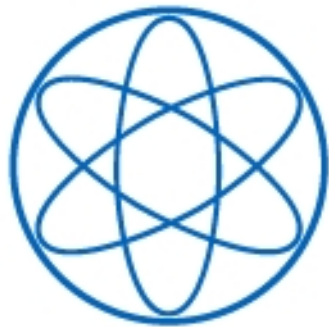


Technische Universität München

Physik Department E20

Molecular Nanoscience & Chemical Physics of Interfaces



Dynamics of Solid-State Effects probed by
Attosecond Photoemission

DISSERTATION

Martin Eduard Ulrich Schäffer

TECHNISCHE UNIVERSITÄT MÜNCHEN

Department E20

Molekulare Nanowissenschaften & Chemische Physik von
Grenzflächen

Dynamics of Solid-State Effects probed by Attosecond Photoemission

Martin Eduard Ulrich Schäffer

Vollständiger Abdruck der von der Fakultät für Physik der Technischen
Universität München zur Erlangung des akademischen Grades eines

Doktors der Naturwissenschaften (Dr. rer. nat.)

genehmigten Dissertation.

Vorsitzender: Prof. Dr. Ulrich Gerland
Prüfer der Dissertation: 1. Prof. Dr. Johannes Barth
2. Priv.-Doz. Dr. Hristo Iglev

Die Dissertation wurde am 13.12.2017 bei der Technischen Universität München
eingereicht und durch die Fakultät für Physik am 12.02.2018 angenommen.

Abstract

Previous experiments have demonstrated time delays of the order of attoseconds (1 as = 10^{-18} s) in photoemission. Different mechanisms have been suggested to explain these delays. This thesis investigates the possible influence of the band structure on the photoemission time evolution in solids. Attosecond streaking technology, a well-established tool of time-resolved photoelectron spectroscopy, has been applied to highly-oriented pyrolytic graphite (HOPG) and magnesium. From HOPG valence band streaking data acquired at the two XUV attosecond photon energies of 112 eV and 93 eV, a relative photoemission delay between two distinct features of the spectrum was retrieved. These signals mainly consist of electrons emitted from C2*s*-derived and C2*p*-derived states, respectively. The emission of the latter group of electrons is found to be delayed with respect to the former by ≈ 30 as on average for both XUV energies. The experimental results are interpreted based on a model relating the delays to the combined influences of the group velocity dispersion and the Eisenbud-Wigner-Smith (EWS) delay acquired upon traversing the graphite layers. In magnesium, the relative photoemission delay between Mg2*p* electrons (2*p*) and conduction band electrons (CB) was extracted from streaking spectrograms acquired at 135 eV and 145 eV. The choice of these energies was motivated by synchrotron data, which show a resonant enhancement of the photoelectron yield for ≈ 135 eV excitation energy, and by a theoretical model which predicts a minimum of the 2*p*-CB delay near this energy. The data acquired in the course of this thesis reveal a considerably smaller delay for 135 eV than in the comparative measurements at 145 eV. For both XUV energies, streaking scans have been performed in normal emission geometry, and for both $\pm 2^\circ$ and $\pm 20^\circ$ acceptance angle of the spectrometer. The enhancement of the acceptance angle increases the delay in the 135 eV experiment but has no significant effect for 145 eV, which could be explained by an excitation energy dependence of the surface contribution to the CB photoemission signal. A chirp analysis of the emitted electron wave packets supports the prediction that the dependence of the delay on excitation energy is linked to an interplay between resonant and non-resonant contributions to the CB photoemission.

Zusammenfassung

Bisherige Experimente haben Zeitverzögerungen in der Größenordnung von Attosekunden ($1 \text{ as} = 10^{-18} \text{ s}$) in der Photoemission nachgewiesen. Verschiedene Mechanismen wurden zur Erklärung dieser Zeitverzögerungen vorgeschlagen. Die vorliegende Dissertation untersucht den möglichen Einfluss der Bandstruktur auf die Zeitentwicklung der Photoemission. Attosecond Streaking, eine etablierte Messmethode der zeitaufgelösten Photoelektronenspektroskopie, wurde auf Proben aus hoch-orientiertem pyrolytischem Graphit (HOPG) und Magnesium angewandt. Aus den Streakingdaten des HOPG-Valenzbandes bei den XUV-Energien 112 eV und 93 eV wurden relative Emissionszeitverzögerungen zwischen zwei verschiedenen Teilen des Spektrums bestimmt. Das Signal des einen Beitrags ist hauptsächlich auf Emission aus $C2s$ -abgeleiteten, der des anderen hauptsächlich auf Emission aus $C2p$ -abgeleiteten Zuständen zurückzuführen. Die Emission des letztgenannten Beitrags ist relativ zu der des erstgenannten um durchschnittlich etwa 30 as verzögert. Das Ergebnis wird mithilfe eines theoretischen Modells interpretiert, das die gemessenen Emissionsverzögerungen durch kombinierten Einfluss der Dispersion der Gruppengeschwindigkeit und der beim Transport durch die Graphit-Schichten auftretenden Eisenbud-Wigner-Smith-Zeitverzögerung (EWS) erklärt. Mithilfe der an Magnesium durchgeführten Streakingmessungen bei 135 eV und 145 eV wurde die relative Emissionsverzögerung zwischen $Mg2p$ Rumpfelektronen ($2p$) und Leitungsbandelektronen (CB) bestimmt. Die Wahl der Anregungsenergien war durch Synchrotron-Daten, die eine resonante Verstärkung des Photoelektronensignals für Energien nahe 135 eV zeigten, und durch die theoretische Vorhersage eines Minimums des $2p$ -CB Zeitversatzes in Energiebereich um 135 eV, motiviert. Die im Lauf dieser Dissertation aufgenommenen Daten zeigen für 135 eV eine deutlich kleinere Emissionszeitverzögerung als für 145 eV. Für beide Photonenenergien wurden die Messungen in senkrechter Emission durchgeführt, und Streaking-Spektrogramme wurden sowohl für Akzeptanzwinkel im Flugzeitspektrometer von $\pm 2^\circ$ als auch für $\pm 20^\circ$ aufgenommen. Dabei wurde entdeckt, dass bei 135 eV die Vergrößerung des Akzeptanzwinkels auch eine Vergrößerung des Zeitversatzes bedingt, während die Änderung des Akzeptanzwinkels bei 145 eV ohne signifikanten Effekt bleibt. Dieses Resultat konnte durch eine Abhängigkeit des Oberflächenanteils am CB-Photoemissionssignal von der Anregungsenergie erklärt werden. Das Ergebnis einer Untersuchung des Chirps der emittierten Elektronenwellenpakete stärkt die Vermutung, dass die Energieabhängigkeit der Emissionszeitverzögerung sich mit einem Wechselspiel aus resonanten und nicht-resonanten Beiträgen zum CB-Photoemissionssignal erklären lässt.

Contents

1	Introduction	3
2	Fundamentals of Attosecond Physics	7
2.1	High harmonic generation(HHG) in noble gases	7
2.2	Introduction to attosecond streaking	12
2.2.1	Attosecond streaking technique	12
2.2.2	Streaking spectroscopy from solid surfaces	15
3	Experimental Methods	23
3.1	Few-cycle femtosecond NIR pulse production	23
3.1.1	The FP3 laser setup	24
3.1.2	The FP2 laser setup	26
3.2	Streaking spectroscopy beamline	27
3.2.1	Overview	27
3.2.2	High harmonic generation and attosecond pulses	28
3.2.3	Surface science apparatus	31
3.2.4	Time-of-flight (TOF) spectrometry	34
3.3	Streaking data evaluation	37
3.3.1	Background subtraction methods	37
3.3.2	Attosecond retrieval	38
3.4	Scanning tunneling microscopy (STM)	39
4	Attosecond streaking spectroscopy on HOPG	41
4.1	Material characteristics	42
4.1.1	Crystal structure	42
4.1.2	Interactions with NIR light	44
4.1.3	Bandstructure and valence band spectrum	47
4.2	Valence band streaking spectroscopy	51
4.2.1	Streaking study at 112 eV XUV energy	51
4.2.2	Streaking study at 93 eV XUV energy	54
4.3	Theory	59

4.4	Tungsten adsorbates on HOPG	64
4.5	Summary and outlook	66
5	Attosecond photoemission timing on magnesium	69
5.1	Background and motivation	69
5.2	Conduction band synchrotron data	74
5.2.1	General evaluation	75
5.2.2	Surface state emission characteristics	76
5.3	Conduction band XUV spectroscopy	78
5.4	Magnesium attosecond streaking	79
5.4.1	Sample preparation and characterization	79
5.4.2	Streaking measurement details	81
5.4.3	Streaking results at 135eV excitation energy	82
5.4.4	Streaking results at 145eV excitation energy	89
5.4.5	Discussion of the experimental results	93
5.5	Conclusion	97
6	Summary and Outlook	99

Chapter 1

Introduction

The availability of attosecond light sources makes it possible to study ultrafast electron dynamics on their natural time scale (1 as = 10^{-18} s). In attosecond photoemission experiments, it has been shown that the photoelectron is ejected into the vacuum not instantaneously after photoexcitation, but only after a finite emission delay of the order of attoseconds. Such delays have for example been observed in experiments on solid-state samples [1–10], molecules and nanoparticles [9, 11–13], and on atoms in the gas phase [14–20]. The discovery of finite time effects in photoemission triggered the development of several theoretical models to rationalize and interpret the photoemission time evolution [11, 19, 21–27]. To date, there are several alternative experimental approaches to access the temporal information on the attosecond scale. Besides attosecond streaking [28–30], the technique used for all attosecond experiments of this thesis, angular streaking [31], transverse streaking [32] and reconstruction of attosecond harmonic beating by interference of two-photon transitions (RABBITT) [33–35] are some of the established methods. Different detailed reviews of the above and further experiments, theories and techniques give deeper insight into this rapidly expanding interesting field of attosecond physics [13, 36, 37]. However, despite the continuous progress in this domain, several open questions and experimental limitations still remain challenging. In particular, the question of the origin of the mentioned photoemission delays has been causing controversy.

This thesis aims at deepening the understanding of photoemission from solids in the time domain, with emphasis on the possible influence of band structure effects. Hence, attosecond experiments have been performed to track the temporal evolution of photoelectrons excited from the valence band states of graphite, and from the Mg2*p* core level and the conduction band of magnesium. The question whether and to what extent band structure influences the photoemission timing has been addressed in previous work. In Ref. [4], the authors distinguish electron-

electron scattering and screening effects on the time evolution of photoelectrons excited from Ni3*d* and Cu3*d* orbitals by attosecond pulse trains. Another experiment which also employed attosecond pulse trains demonstrates that the lifetime of the photoexcited state from Ni(111) is strongly increased when the final state coincides with a short-lived excited state, and links an observed strong dependence of this lifetime on the emission angle to the final-state band dispersion [5]. In a different study, an attosecond interferometry technique with attosecond pulse trains has been applied to Ag(111) and Au(111), and a strong dependence of measured photoemission delays on the excitation energy was observed, which was attributed to final-state effects [6]. In an attosecond streaking experiment on WSe₂, the photoemission from four distinct levels is observed to be time-ordered with increasing initial-state angular momentum [7]. The measured relative emission time delays are explained by propagation and intra-atomic interactions; a significant influence of the angular momentum on the timing is suggested. A theoretical study of resonant charge transfer in collisions of H⁻ ions with a Cu(111) surface stated that the influence of the projected band gap in copper on the charge transfer depends crucially on the interaction time, i.e. the ion-surface collision velocity [38, 39]. The effect of the band gap becomes negligible at large velocities, which might mean that the interaction time is too short for the transferred electron to probe the band structure. The suggested dependence of the influence of projected band gaps on the interaction time in resonant charge transfer was indeed observed in Li⁺ ion scattering off an Ag(100) surface [40].

In the first main project of the present work, attosecond streaking experiments were conducted on highly-oriented pyrolytic graphite (HOPG) and the timing of the HOPG valence band photoemission signal was investigated at the two pump photon energies of 93 eV and 112 eV. At these energies, the valence band spectrum exhibits two partially resolved peaks. By band structure considerations and from X-ray photoemission spectroscopy (XPS) and X-ray emission spectroscopy (XES) data, the peak at lower binding energy could be identified as derived from primarily C2*p* states and the peak at higher binding energy could be assigned to mainly C2*s* states. The measurement of the relative photoemission timing between the two peak features in this thesis yields a significant time delay of the photoemission from the peak at lower binding energy with respect to the emission from the peak at higher binding energy for both photon energies. Motivated by this experimental result, a theoretical description has been developed by Christoph Lemell [41]. In this model, the origin of the delays is related to an interplay of group velocity dispersion and the Eisenbud-Wigner-Smith (EWS) delay of the photoelectron wave packet accumulated during transport through the graphite layers.

Another project pursued in this thesis aimed to achieve 2D films of tungsten which would allow for streaking measurements on this 2D system. This work was motivated by the idea to disentangle propagation effects on photoemission timing by comparison of streaking data from 2D tungsten to the large data basis available for 3D [2, 3, 8, 9]. Following this approach, 2D nanoclusters of tungsten have been deposited on an HOPG sample. The successful preparation of the clusters was demonstrated and characterized by scanning tunneling microscopy (STM) methods.

Theoretical calculations predict the interplay of direct surface emission and so-called resonant bulk emission to be one of the main sources of photoemission delays of conduction band electrons in metals [26]. Photoexcitation of a conduction band electron from an atom deep inside the bulk is only efficient if the energy of the exciting photon matches with a vertical interband transition. If it does, the corresponding emission signal will be strong. This process will henceforth be called resonant bulk emission. On the contrary, if the photon energy does not match, the bulk contribution to the conduction band photoemission will be weak and the signal will be dominated by electrons which are emitted directly from the surface when the electron initial state couples directly to a continuum state. The authors calculated the photoemission time delay of core state electrons with respect to conduction band electrons as a function of excitation energy in the XUV range and predict a strong minimum at ≈ 135 eV which is explained by the energy-dependent bulk emission efficiency. Synchrotron measurements from magnesium show a very strong maximum of the conduction band photoelectron yield around this same energy [42]. The parabolic dispersion of the bulk states visible in these data indicates that vertical interband transitions at this energy occur close to the edge of the first Brillouin zone. The group velocity of the photoexcited electron deep in the bulk is proportional to the slope of the final-state band, which becomes small near the zone edge. Motivated by these considerations, streaking spectroscopy has been exploited in the second main project of this thesis to study the photoemission timing of magnesium in this energy range. Streaking measurements have been performed for two different pump energies, one chosen equal to the resonant energy observed in both theoretical model and synchrotron data, and the other 10 eV beyond the resonance. The experimental results show a significant effect in both delay and wave packet chirp for the resonant energy, which is diminished in the comparative measurements at the reference energy, thus indicating a band structure influence on the photoemission timing.

Within this thesis as well, experimental contributions have been made to several further attosecond projects, which are not detailed in this work. By adsorbing iodine atoms on W(110) and using the photoemission signal from the $I4d$ core level as a reference clock for varying iodine layer density and extrapolating the influence of the adlayer on the timing from tungsten to zero, a big step was made towards absolute photoemission timing [43]. Unprecedented spectral resolution of 1.8 eV (FWHM) in attosecond streaking was achieved in an experiment on tungsten and gallium arsenide [44, 45]. Contribution to the acquisition of attosecond streaking data at 112 eV and 135 eV on tungsten significantly extended the streaking data basis of this material at varying excitation energy [46].

The content of this thesis is organized as follows. The second chapter elucidates the fundamentals of attosecond physics, which form the basis for the experiments. The third chapter describes the details of the experimental setup which was employed in this work. The HOPG projects are discussed in the fourth chapter, and the magnesium experiment forms the content of the fifth chapter. Finally, the sixth chapter is devoted to a summary and outlook.

Chapter 2

Fundamentals of Attosecond Physics

The generation of isolated UV and XUV laser pulses in the sub-femtosecond regime forms the basis for attosecond metrology. The first part of this chapter provides an introduction to the concept of high harmonic generation (HHG) in inert gases, a powerful tool for the production of attosecond pulses. The remainder of the chapter is devoted to the description of the attosecond streaking method which was used throughout this thesis to investigate the characteristics of the photoemission process in the time domain.

2.1 High harmonic generation(HHG) in noble gases

In classical physics, a particle can never cross a potential barrier, if the height of the barrier exceeds the particle energy. However, quantum mechanics predicts that for a barrier of finite width and height, the particle can still overcome the wall with a certain probability. This so-called tunnel effect was first discovered in 1897 in electron field emission in vacuum [47]. The tunneling probability is calculated from basic quantum mechanics and decays exponentially with both width and height. Particles can tunnel through barriers of finite height and width. An electron in an unperturbed atom is bound by the Coulomb potential of infinite range and tunneling is forbidden. Upon application of strong electric fields to the atom, it is possible to deform the potential in such a way that the Coulomb barrier becomes finite. This leads to a non-vanishing tunnel probability for the electrons. In 1987, it has been demonstrated that atoms in the gas phase, which are exposed to highly-intense linearly polarized laser pulses, emit a very distinctive radiation spectrum [48]. This spectrum consists of a line series at energies equal to odd multiples of the fundamental frequency of the stimulating laser field and is called high-harmonic radiation. A schematic high-harmonic spectrum is shown in Fig. 2.1. The signal intensity decays exponentially with increasing photon energy for

low orders and then stays constant over a rather broad energy interval before it finally falls off exponentially to zero [49].

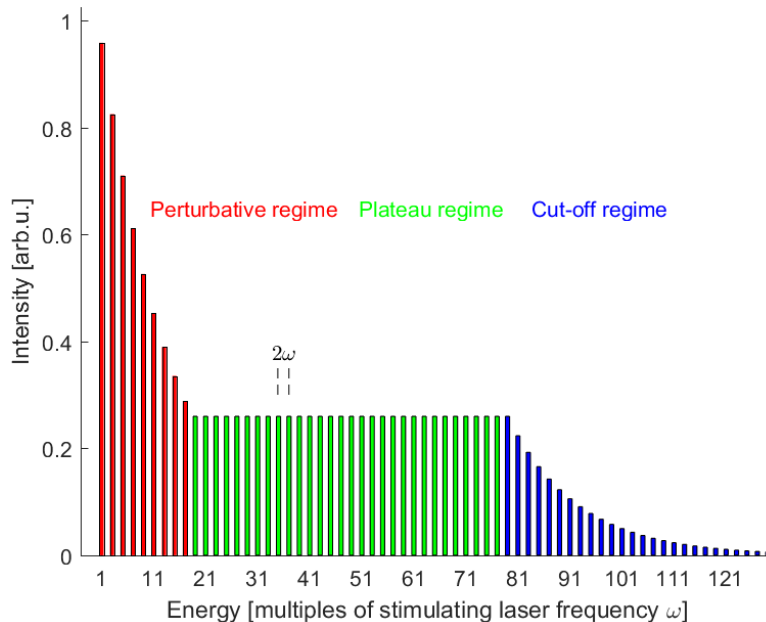


Figure 2.1: Schematic illustration of high-harmonic spectrum excited in atomic gas by a highly-intense laser field.

The mechanism of the high-harmonic generation (HHG) is based on tunneling of the electron through the Coulomb barrier distorted by the electric field of the driving laser pulse. The HHG quantum-mechanical phenomenon can to some extent be intuitively understood in terms of a semi-classical three-step model [49], which shall be described below and illustrated in Fig. 2.2.

1) Distortion of the atomic Coulomb potential and tunneling of an outer-shell electron into the continuum

In the first step of the semi-classical picture, the Coulomb potential of the atom is strongly perturbed by the laser field, such that a weakly bound outer-shell electron can tunnel into the vacuum. This tunneling process is triggered most efficiently near the extrema of the laser field, where the intensity is the highest and the distortion of the atomic potential is the strongest.

2) Acceleration of the tunneled electron in the laser field

Once ejected into the vacuum, the electron is then accelerated away from its parent ion by the laser field. One quarter-cycle of the laser oscillation later, the laser field changes sign and the electron is accelerated back. On its roundtrip in the laser field, the electron has gained kinetic energy, whose precise amount depends crucially on the phase of the laser field at the moment of tunneling.

3) Recombination of the electron with the parent ion and release of the excess energy

With a certain probability, the electron can recombine with the parent ion. Quantization rules dictate that recombination is efficient only for electrons whose acquired energy equals multiples of the fundamental laser frequency, where only odd multiples are allowed due to the inversion symmetry of the gas phase. The excess energy is then released by the atom as a photon.

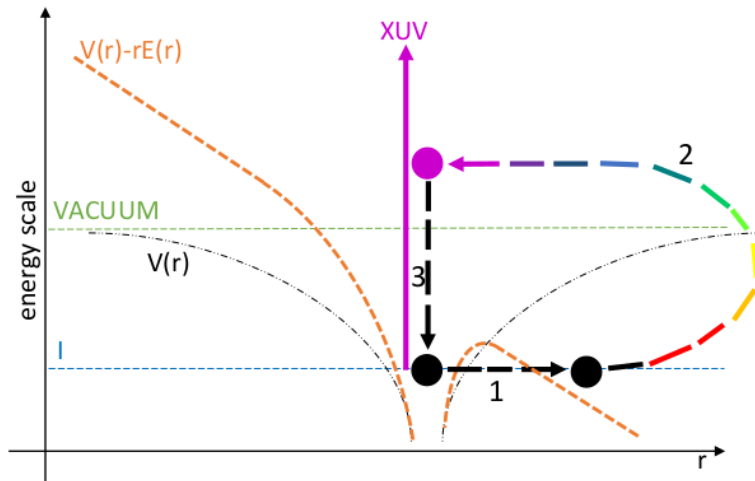


Figure 2.2: Semi-classical model of HHG [49]. 1) Distortion of the Coulomb-potential $V(r)$ by the laser field $-rE(r)$. Tunneling of an electron bound by the ionization potential I into the continuum. 2) Electron kinetic energy gain in round-trip through the laser field, indicated by the color map along the trajectory. 3) Excess energy release via XUV photon upon electron recombination with parent ion.

The duration of the journey of the electron in the laser field is only one half-cycle of the laser oscillation or even less. The created high-harmonic light bursts can thus be significantly shorter than half of the period of the driving laser. The plateau in

the high-harmonic spectrum arises from the interference of HHG in all half-cycles comprised in the laser pulse. For the applications of this work, it is desirable to extract a short, high-energetic single pulse from the high-harmonic radiation. The existence of the cut-off region stems from the fact that the maximum energy the electron can return to the parent ion is finite, and linked to the trajectories which are launched near the strongest maximum of the laser pulse. Classical analysis of the electron trajectories shows that the highest energy is transferred to the electrons which tunnel at $\omega t = 167^\circ$ before the maximum of the highest field oscillation [49]. The precise cut-off energy can be calculated within a full quantum-mechanical treatment, see [50]. Therein, the authors obtain

$$E_{cut-off} \simeq 3.17U_p + I_p \times f(I_p, U_p), \quad (2.1)$$

where I_p is the ionization potential of the atom, $U_p = e^2 E_0^2 / 4m\omega^2$ is the ponderomotive potential, which represents the cycle-averaged kinetic energy which the electron gains during its roundtrip in the electric field of the laser pulse. E_0 therein is the maximum amplitude of the electric field of the driving laser. Then, f is a function of the ionization potential and ponderomotive potential, which reduces to $f = 1.32$ in the limit $I_p \ll U_p$. Under the experimental conditions typical for this thesis, laser intensities up to 10^{15} W/cm² were employed in HHG generation from Neon. Accordingly, $U_p \approx 40$ eV and $I_p = 21.6$ eV, and therefore generates cut-off energies of up to 155 eV. However, generating XUV flux high enough to conduct streaking experiments with sufficient statistics, is challenging already for photon energies of 135 eV and higher. In the course of this work, by optimizing the experimental parameters in HHG, it has been possible to perform streaking spectroscopy even at 145 eV, as will be discussed below.

If the laser pulse comprises many optical cycles, there will be many comparably strong field maxima. The cut-off region will hence be formed upon interference of the trajectories launched at $\omega t = -167^\circ$ from these field maxima and the cut-off will be strongly modulated. Conversely, in the limit of a single-cycle pulse, there will be a unique global field maximum, the photons with the highest energy will thus originate from a unique moment of time, and hence, this situation will correspond to a completely flat cut-off. In practice, the single-cycle limit is hard to obtain, but already two-cycle (or slightly shorter) pulses can be routinely achieved. For such short pulses, the value of the carrier-envelope phase (CEP) becomes a very decisive parameter, as demonstrated in Fig. 2.3. The shape of the laser pulse is strongly influenced by the CEP. It is instructive to compare two extreme cases. For a CEP-value of $\phi = 0^\circ$, the pulse exhibits cosine-shape as drawn in Fig. 2.3a and shows a unique global field maximum, such that the creation of the highest-energy photons is uniquely localized in time and accordingly, the cut-off region

of the spectrum in the lower part of Fig. 2.3d will be flat. In this case, a nicely isolated short pulse can be extracted from the spectrum via spectral filtering, which is accomplished by using multilayer mirrors whose bandpass-reflection properties, such as FWHM and central energy, can be tuned, as will be discussed in the next chapter. For $\phi = 90^\circ$, in contrast, the cut-off is modulated as highlighted in the upper of Fig. 2.3d by the interference of the trajectories launched near two equally pronounced field maxima and thus, only a double-pulse can be filtered. In this case, the pulse assumes sine form like in Fig. 2.3b.

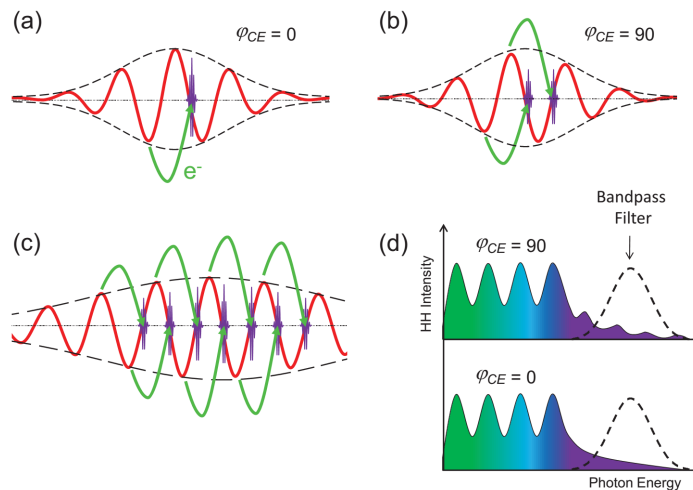


Figure 2.3: Carrier-envelope phase (CEP) of the driving laser pulse ϕ crucially influences the high-harmonic spectrum. For $\phi = 0^\circ$, there exists a unique global field maximum of the generated pulse as shown in a). In this case, the electron trajectories which lead to the emission of the highest-energy photons are tied to a unique moment of time and hence the cut-off region is flat and a single isolated pulse can be filtered as seen in lower part of d). For the symmetry resemblance, the incoming laser pulse is referred to as a cosine waveform. For $\phi = 90^\circ$, a sine wave-form appears and there are two field maxima which contribute equally to the highest-energy photon generation, as shown in b), such that the cut-off is modulated and only a double-pulse can be filtered, as displayed in the upper part of d). In c) a many-cycle pulse is shown for comparison. The green curved arrows indicate electron tunneling and recombination processes. Figure adapted from Ref. [2].

In general, for a given value of the CEP, the cut-off will be modulated to a certain degree and the filtered pulse will contain a so-called satellite, which is most pronounced for a sine pulse and vanishes for a cosine pulse. The CEP value $\phi = 0^\circ$ is

defined such that the modulations of the cut-off vanish. Since the characteristics of the filtered pulse depend very strongly on the CEP value, and the laser pulse exhibits inherent shot-to-shot fluctuations of the CEP, it is indispensable to stabilize the phase during the experiment. This wave-form control is described in the next chapter. In fact, the considerations drawn before hold true for an isolated atom. For an ensemble of atoms in the gas phase, as it is the case within this work, laser focusing and dispersion from the cloud of freed electrons lead to dephasing, which thus needs to be carefully taken care of by tuning the accessible experimental parameters as interaction length, focussing, and gas pressure. An important geometric property of HHG is the small and order-dependent divergence angle of the high-harmonic radiation, which is $\theta_n \approx \theta/\sqrt{n}$, where n is the HH order and θ the divergence of the driving laser [51, 52]. This property enables spatial separation of the high-harmonic components from the fundamental frequency, which is necessary for the experiments conducted in this work. Within the current discussion, only HHG in atomic gases was considered, because these were used as sources for HHG during the experiments in the course of this thesis. In recent years, a profound number of experiments have demonstrated HHG in solid targets as well [53–57], and theory on this more complex phenomenon has been developed [58–62]. The elucidation of HHG is concluded here and the chapter continues with the discussion on the attosecond streaking technique. The experimental key points of HHG optimization which were crucial in the measurements in this thesis will be discussed in the next chapter.

2.2 Introduction to attosecond streaking

In this section, the principle of attosecond streaking is reviewed with special emphasis put on the streaking on metallic surfaces, which is of direct relevance for this thesis. In the first part of the section, the technique is described in detail, while the second part discusses the peculiarities of its application to a surface.

2.2.1 Attosecond streaking technique

If a photon is absorbed by an isolated atom, it can photoexcite an electron from an energy level in the atom into the vacuum, provided that the photon energy $\hbar\omega$ exceeds the binding energy E_B of the electron. The electron then escapes from the atom with kinetic energy $E_{kin} = \hbar\omega - E_B$. In attosecond streaking, an electron is excited from the atom by an XUV attosecond pulse in the presence of the NIR laser field, which was used in the first place for the generation of the attosecond pulses via HHG. Once the electron is promoted into the continuum, it feels the time-dependent electric field of the NIR radiation and is accelerated or decelerated.

In principle, the NIR field might already influence the initial state of the electron inside the atom, but this influence is neglected throughout this thesis, as justified by the strong-field approximation.

Classical derivation of the laser field-induced electron energy shift

For a linearly polarized NIR field as used in this work, the photoexcited electron undergoes a change of its momentum component parallel to the laser field, which is derived from the classical equation of motion $m\dot{z} = -eE(t)$ ¹. As the femtosecond field oscillates very fast in time, this change crucially depends on the moment of photoionization τ . The total shift of the parallel momentum component $\Delta p_z(\tau)$ can be written in the form

$$\Delta p_z(\tau) = m\dot{z} = -e \int_{\tau}^{\infty} E(t) dt = -eA_C(\tau), \quad (2.2)$$

where the so-called Coulomb gauge has been invoked, for which the vector potential of the laser field $A_C(t)$ is simply given by the integral of the electric field. The electric field of the NIR radiation can be written in the convenient form

$$E(t) = E_0(t) \cos(\omega t + \phi_{CE}), \quad (2.3)$$

where $E_0(t)$ is the pulse envelope, and ϕ_{CE} is the carrier-envelope phase (CEP) introduced above. Only electrons that escape into the vacuum during the finite duration of the NIR laser pulse experience a net change of their momentum. In the adiabatic limit, where $\dot{E}_0 \ll E_0\omega$, Eq.2.2 leads to

$$\Delta p_z(\tau) = \frac{eE_0(\tau)}{\omega} \sin(\omega\tau + \phi_{CE}) = \sqrt{4U_p(\tau)m} \sin(\omega\tau + \phi_{CE}). \quad (2.4)$$

After the NIR field is extinguished, the final kinetic energy $E_{kin,f} = p_f^2/2m$ of the electron can be calculated in terms of the initial kinetic energy at the moment of photoexcitation, $E_{kin,i}$, by use of Eq.2.4, and by invoking the cosine theorem in the form $p_f^2 = p_i^2 + 2p_f\Delta p_z(\tau) \cos\theta - \Delta p_z(\tau)^2$ as follows [63]:

$$E_{kin,f} \approx E_{kin,i} + 2U_p(\tau) \cos 2\theta \sin^2(\omega\tau + \phi_{CE}) + \sqrt{8U_p(\tau)E_{kin,i}} \cos\theta \sin(\omega\tau + \phi_{CE}), \quad (2.5)$$

where θ denotes the angle between laser polarization and the final momentum vector of the electron. Obviously, the final electron kinetic energy $E_{kin,f}$ depends strongly on θ , and hence on the geometry of the experiment. In the course of this

¹The polarization of the laser field can be fixed along the z -axis without any loss of generality.

thesis, the photoelectron detector has been aligned such that it predominantly detects electrons with momentum parallel to the polarization, i.e. $\theta = 0^\circ$. This alignment shall be called the parallel detection scheme. The applied NIR laser intensities were of the order of $\sim 10^{12} \text{W/cm}^2$ or less, at a central wavelength of $\lambda \sim 750 \text{nm}$. The relevant kinetic energies of the detected photoelectrons were in the range of $50 \text{eV} - 150 \text{eV}$. Under these experimental conditions, $U_p \sim 50 \text{meV} \ll E_{kin,f}$. Hence, for $\theta = 0^\circ$, Eq.2.5 reduces to

$$\Delta E_{kin}(\tau) \approx \sqrt{8U_p(\tau)E_{kin,i}} \sin(\omega\tau + \phi_{CE}). \quad (2.6)$$

In the parallel detection scheme, recording the spectrum of photoelectrons as a function of τ thus results in a direct map of the vector potential A onto the electric field. Indeed, these photoelectron spectra are at the heart of the work in this thesis, and will commonly be referred to as streaking spectrograms and the associated technique as streaking spectroscopy. While the value of τ is not known, a scan over τ is still feasible by variation of the delay between the XUV ionizing field and the NIR laser field. More precisely, the delay between the arrival times of the two laser fields at the atom is tuned by introducing a propagation length difference between the two pulses and then gradually changing the latter. The precise method is thoroughly explained in the next chapter. From such acquired spectrograms, not only information about the NIR field, but also about the XUV field and the temporal characteristics of the photoemission process can be retrieved, as will be elucidated below.

Quantum-mechanical wave-packet description

So far, the electron has been treated as a point-like particle. More precisely, however, the electron will be photoemitted as a wave-packet, on which the temporal structure of the exciting attosecond pulse, and of the emission process, is imprinted. One of the key properties of the emerging electron wave-packet is its time-frequency dependence. This so-called chirp will manifest itself in the streaking spectrogram in a characteristic way. The wave function of the electron, $\Psi(t)$, obeys the time-dependent Schrödinger's equation

$$i\frac{\partial\Psi(t)}{\partial t} = \hat{H}(t)\Psi(t). \quad (2.7)$$

In the single-active electron approximation, the time-dependent Hamilton operator $\hat{H}(t)$ can be written in atomic units as follows

$$\hat{H} = \frac{1}{2} \left(\hat{p} + \hat{A}(t) \right)^2 + \hat{V}(\hat{r}) + \hat{E}_{XUV}(t) \cdot \hat{r}, \quad (2.8)$$

with the operators of the laser field vector potential \hat{A} , the ionizing XUV field \hat{E}_{XUV} , the momentum operator \hat{p} and position operator \hat{r} , and the effective potential of the parent ion \hat{V} . Assuming that only electrons with momentum parallel to the laser polarization are detected, and writing the XUV field in the way $\hat{E}_{XUV}(t) = E_{XUV}(t)e^{-i\omega_{XUV}t}$ with the pulse envelope E_{XUV} and the central frequency ω_{XUV} , the transition amplitude for the final momentum state p can be written as a function of the XUV-NIR delay τ as follows [29, 64, 65]:

$$c(p, \tau) = -i \int_{-\infty}^{\infty} dt E_{XUV}(t + \tau) M(p + A(t)) e^{i\Phi_v(p,t)} e^{ip^2/2} e^{-ip_i^2/2}, \quad (2.9)$$

with the transition-matrix element M , the initial momentum p_i and the Volkov phase-modulation, which is given as [66]

$$\Phi_v(p, t) = - \int_t^{\infty} ds \left(pA(s) + \frac{1}{2}A^2(s) \right). \quad (2.10)$$

Under the assumption that the matrix elements exhibit a weak dependence on the energy, the electron wave packet $\Phi(t)$ can be written as $\Phi(t) = f(t)e^{-(p_i^2/2)t}$, with comprising the temporal evolution of the XUV pulse and the matrix elements contained in the function f . In this way, the streaking spectrum $P(E, \tau)$ is constructed as

$$P(E, \tau) = |c(p, \tau)|^2 = \left| -i \int_{-\infty}^{\infty} dt f(t) e^{i\Phi_v(p,t)} e^{ip^2/2} e^{-ip_i^2/2} \right|^2. \quad (2.11)$$

Suitable parametrizations for $f(t)$ and $A(t)$ are discussed in the next chapter.

2.2.2 Streaking spectroscopy from solid surfaces

So far, the streaking of an electron from an isolated atom was discussed. This approximation holds for atoms in the gas phase. Within this thesis, however, streaking spectroscopy has been applied to solid samples, whereby the description of the streaking process must take into account several important phenomena that are absent in the case of an isolated atom. These include inelastic scattering and the resulting finite escape depth of the photoexcited electrons, the initial state characteristics of the electrons, the role of the penetration depth of the NIR field into the solid, and band structure effects such as band dispersion and group velocity. After a general description of the process of attosecond streaking from surfaces, the just mentioned topics are discussed one by one.

Attosecond streaking from solids

To understand the streaking process from solid surfaces, it is necessary to comprehend the mechanism of photoemission in the first place. To this end, it is instructive to follow a classical approach, which is based on three subsequent steps [67]. Firstly, the electron is excited by the XUV pulse from an initial band state $E_i(\vec{k}_i)$ into a final band state $E_f(\vec{k}_f)$. While dispersion is very small for core states, it can be significant for valence states. The probability of the transition $i \rightarrow f$ is given by the transition dipole matrix elements (TDME). The transition has to obey energy conservation $E_i(\vec{k}_i) + \hbar\omega = E_f(\vec{k}_f)$, where ω is the XUV carrier frequency, and momentum conservation in the form $\vec{k}_i + \vec{G} = \vec{k}_f$, where \vec{G} is a vector of the reciprocal lattice of the crystal². The excited electron is then supposed to travel to the surface at its group velocity. It is however not clear if band structure is well-established on this ultrashort time scale, and hence the meaning of group velocity is questionable. This issue will be further addressed in course of this thesis.

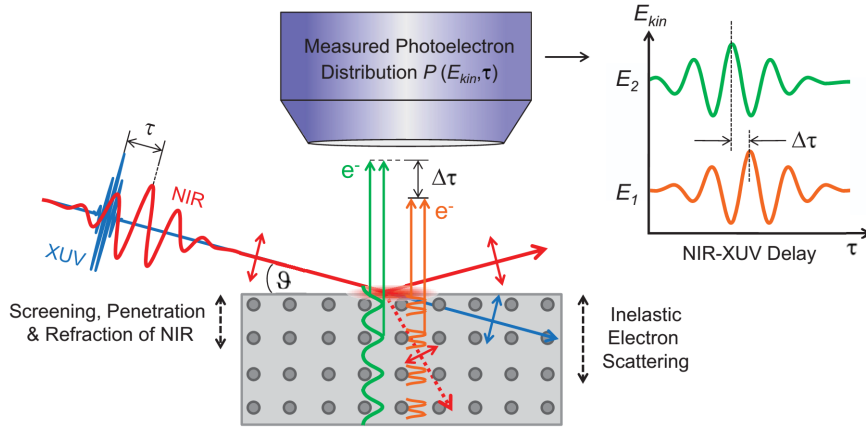


Figure 2.4: Streaking from solids. NIR and XUV pulses hit the sample under grazing incidence. The XUV pulses excite electrons from different electronic states, as drawn for core states and valence band states in orange/green color, respectively. The electrons propagate towards the surface in a possibly spatially inhomogeneous NIR streaking field. A streaking spectrogram is recorded, where a temporal offset τ between the streaking curves, here between green and orange, is related to the photoemission timing delay between those electrons. The timing is sensitive to the NIR field penetration and refraction, to inelastic electron scattering, possibly to group velocity effects and to the initial state characteristics. Figure from [2].

²In the XUV spectral range, the photon momentum is negligible.

Upon arrival at the surface-vacuum interface, the electron can be emitted into the vacuum, provided that its kinetic energy is larger than the work function. In the emission process, due to broken translational invariance in the direction perpendicular to the surface, only the momentum component parallel to the surface is conserved. Certainly, this classical description is insufficient and needs to be replaced by a rigorous quantum-mechanical treatment. Here, the TDME is calculated in terms of the overlap between bulk Bloch states and "time-reversed LEED states" (low energy electron diffraction). On the quantum-mechanical electron wave-packet, the temporal structure of the exciting XUV pulse and of all interactions between electron and solid are imprinted.

After this theoretical discussion, a look shall be taken at a schematic view of the concept of streaking from solids which is adopted in this work and displayed in Fig. 2.4. The attosecond XUV and few-femtosecond NIR fields hit the surface of the solid co-axially at a grazing angle. The XUV field photoexcites electrons inside the solid, which then propagate to the surface and are emitted into the vacuum in the presence of the NIR streaking field. The spectrometer is aligned such that it predominantly detects those photoelectrons which were released perpendicular to the surface. By gradually changing the relative delay between the arrival times of the NIR and XUV fields at the surface, and recording a photoelectron spectrum at each delay step, a streaking spectrogram is acquired. Photoelectrons are excited from rather delocalized valence band states and from stronger localized shallow core states, as indicated in green and orange color in Fig. 2.4, respectively.

As explained earlier in this section, the kinetic energy shift of the electron crucially depends on the phase of the vector potential at the moment in which the electron starts to "feel" the NIR laser field. If electrons from different levels experience the NIR at different times, their streaking curves will be shifted with respect to each other, as indicated on the right-hand side of the current figure. Assuming that the NIR field does not penetrate the surface, this moment is just the moment of emission into the vacuum, and then the relative shift in the streaking curves can be interpreted as the relative photoemission timing delay. However, in general, the NIR can penetrate a certain distance into the solid, and the penetration depth, as well as the relative strength of the laser field inside the sample, must be carefully taken into account to allow for a correct interpretation. The role of the penetration depth of the NIR field will be discussed further at a later stage. For any relative emission time delay between electrons excited from different energy levels, the different escape depths are also of importance as detailed below.

Inelastic scattering and escape depth

When the electron is photoexcited inside the solid and travels towards the surface, it may experience inelastic scattering events, which change both its energy and momentum. In the absence of scattering, the photoemission from a generic state in the electronic structure of the solid would manifest itself as a peak in the spectrum, which is broadened by unresolved vibrational structures, analyzer resolution, lifetimes and the line width of the exciting photon. A scattered electron, however, which leaves the solid with reduced kinetic energy, will contribute to the inelastic background at the low-energy side of the peak. The photoemission signal I obtained from electrons of given energy as a function of the escape depth x can be written as

$$I \sim e^{-x/\lambda \cos \theta}, \quad (2.12)$$

where θ is the emission angle of the electron with respect to the surface normal, and λ is the so-called inelastic mean free path (IMFP).

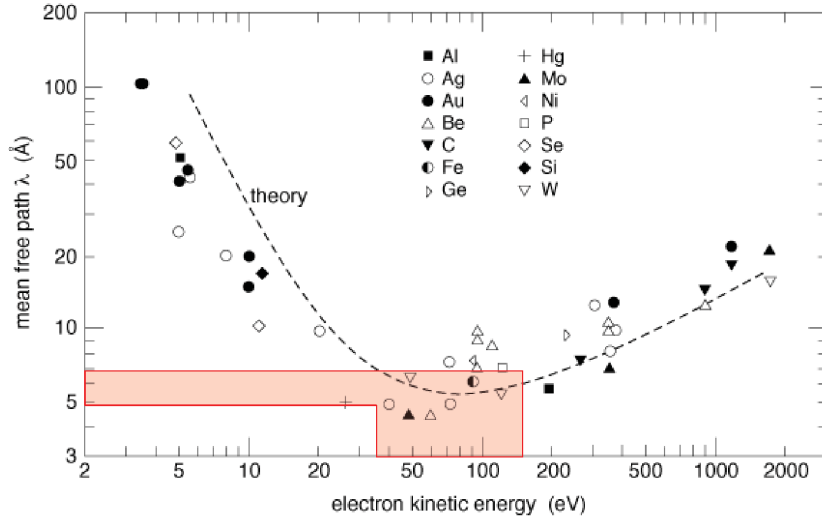


Figure 2.5: The inelastic mean free path (IMFP) of electrons as a function of the kinetic energy for different materials. The IMFP follows a largely "universal" curve. The experimentally relevant range is here indicated in orange. Taken from Ref. [68].

As inferred from Fig. 2.5, for the kinetic energies relevant in this work, λ is of the order of a few Å, which amounts to only a few atomic layers. This renders photoemission spectroscopy a very surface sensitive method. In the discussion on relative photoemission timing, the IMFP of electrons emerging from specific

levels plays an important role. In particular, the ratio of the IMFP to the group velocity gives a rough estimate of the propagation and thus the emission time. Here, however, it has to be noted that it is not a priori clear that band structure effects such as group velocity are really a predominant cause for photoemission timing delays in solids. Therefore, one driving force for this thesis is the attempt to better understand the role of band structure in photoemission timing.

Penetration of the NIR field

Under the assumption that the NIR streaking field does not penetrate into the sample, the photoexcited electrons will only feel the field at the moment of emission into the vacuum, and in this case, any offset between the streaking traces of electrons from different levels will be directly linked to the relative photoemission time delay between those electrons. Due to the finite penetration depth of NIR frequencies into solids, this assumption is never strictly correct, and even though it can often still provide a good approximation, the validity has to be carefully checked in each experiment.

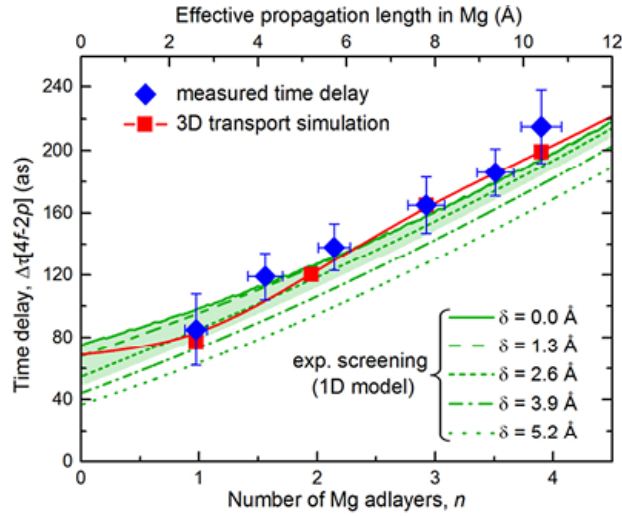


Figure 2.6: Blue icons show relative photoemission timing delay between electrons emitted from W 4f and Mg 2p states as a function of Mg(0001) film thickness. Time delays predicted by a 1D simulation of the photoelectron release dynamics for different screening lengths δ of the NIR field at the magnesium-to-vacuum interface are shown in green. Red squares indicate time delays derived from a full 3D electron transport model, the red line serves as guide to the eyes only. Taken from Ref. [69]

The penetration of the optical field into the solid depends on the electronic properties of the material. The electrons in the solid will screen the laser field, and the efficiency of the screening depends strongly on the material and the frequency of the field. The most important experiments presented in this thesis have been carried out on Mg(0001) samples, and for this case, instructive studies have been performed prior to this work on the screening depth of the NIR into the magnesium bulk [69]. Moreover, streaking spectroscopy has also previously been applied to hybrid Mg-W samples. These samples consist of a W(110) substrate on which very thin adsorbates of Mg(0001) have been deposited by evaporation from a Mg-filled crucible. For different numbers of atomic adlayers of magnesium, streaking spectrograms have been acquired, from which the relative offset in time between the streaking traces of electrons emerging from the tungsten 4f level and the magnesium 2p level have been extracted, as presented by the blue diamonds in Fig. 2.6. To give an estimate of the screening length of the NIR field at the Mg surface, a one-dimensional electron transport simulation has been performed in which the penetrating field component parallel to the surface normal, $E(z)$, is modeled as

$$E(z) \sim e^{-(z-z_{im})/\delta}, \quad (2.13)$$

where z_{im} denotes the location of the plane of image charges [70] and δ the screening length. The parameters of the simulation are then fitted such that the model reproduces the measured temporal offsets in the best possible way.

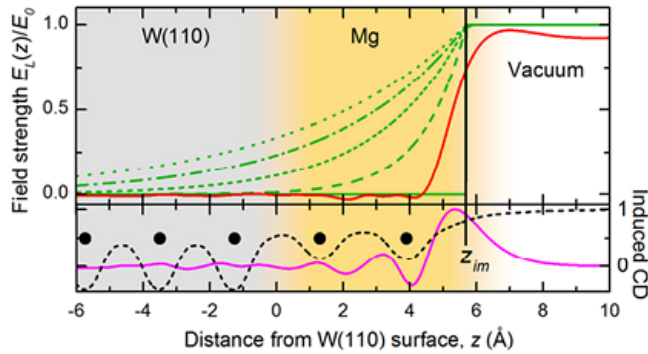


Figure 2.7: The upper panel of the figure illustrates the different screening scenarios displayed in Fig. 2.6. The red line describes the spatial variation of the electric field at the interface as predicted by TDDFT calculations. The lower panel depicts the NIR-induced charge density (CD) at the metal-vacuum interface at the maximum of the laser pulse derived by TDDFT (magenta line). The position of the dynamic image plane is indicated by the black solid line. The black line shows the lattice potential (averaged parallel to the crystal surface) employed in the DFT calculations. Taken from Ref. [69].

As shown by the green lines in Fig. 2.6, the model agrees well with the experimental data for $\delta \sim 0 - 3\text{\AA}$, which is less than the perpendicular lattice constant of Mg(0001). This implies that the NIR field is very efficiently screened already within the first atomic layer. In addition to the phenomenological 1D-model, a three-dimensional transport model was employed which shows good agreement with the experimental data as well (red squares in Fig. 2.6). Within this model, the screening process was investigated by time-dependent density-functional theory (TDDFT). This led to the conclusion that the laser field is already completely screened at the topmost atomic layer, in agreement with the conclusion based on the comparison between experimental data and phenomenological 1D model discussed above. The results of the TDDFT analysis are shown in Fig. 2.7. It appears that for a free-electron-like material such as in magnesium, the assumption that the NIR does not significantly penetrate into the solid is justified, as the screening length is found to be smaller than the lattice spacing. In this case, the temporal offsets between the streaking curves of different levels can then be reliably interpreted as relative photoemission timing delays.

Chapter 3

Experimental Methods

This chapter describes the setup and techniques used for the experiments within this work. Streaking spectroscopy of solids combines laser technology and surface science. Up-to-date laser technology enables efficient production of few-cycle femtosecond NIR laser pulses, generation and characterization of high harmonics of the NIR frequency and the extraction of isolated attosecond XUV pulses from the high-harmonic spectrum. In the field of surface science, refined techniques for sample preparation and characterization, the ability to maintain an ultra-high-vacuum environment (UHV) to prevent contamination of the sample surface by the residual gas, and high-performance detection schemes for the photoelectrons which are emitted from the sample upon excitation by the XUV light are well-established. The present chapter addresses each of these aspects and furthermore elucidates how the temporal information can be obtained from the streaking spectrogram by means of a MATLAB based retrieval code. It concludes with a brief introduction to scanning tunneling microscopy, a technique employed in a separate study on deposition of tungsten on highly-oriented graphite, as discussed later in this thesis.

3.1 Few-cycle femtosecond NIR pulse production

As discussed in the previous chapter, very short, high-intensity phase-controlled laser pulses are required for efficient generation of high-harmonic spectra with high-energetic and unmodulated cut-off region, from which well-isolated attosecond pulses can be extracted. Highly-intense laser pulses are needed to trigger the strongly nonlinear process of HHG. Phase-stability is crucial since the streaking experiments require a well-defined CEP and the HHG spectrum is highly sensitive to the value of the latter. This section introduces the two distinct yet in many regards similar production units which were employed in the course of this thesis for the generation of phase-stable few-cycle femtosecond NIR pulses.

3.1.1 The FP3 laser setup

A schematic overview of the setup which was employed for attosecond streaking experiments with XUV energies at 145 eV is shown in Fig. 3.1 and the constituting components and their function is briefly discussed below. Further information about the setup can be found in Refs. [71, 72].

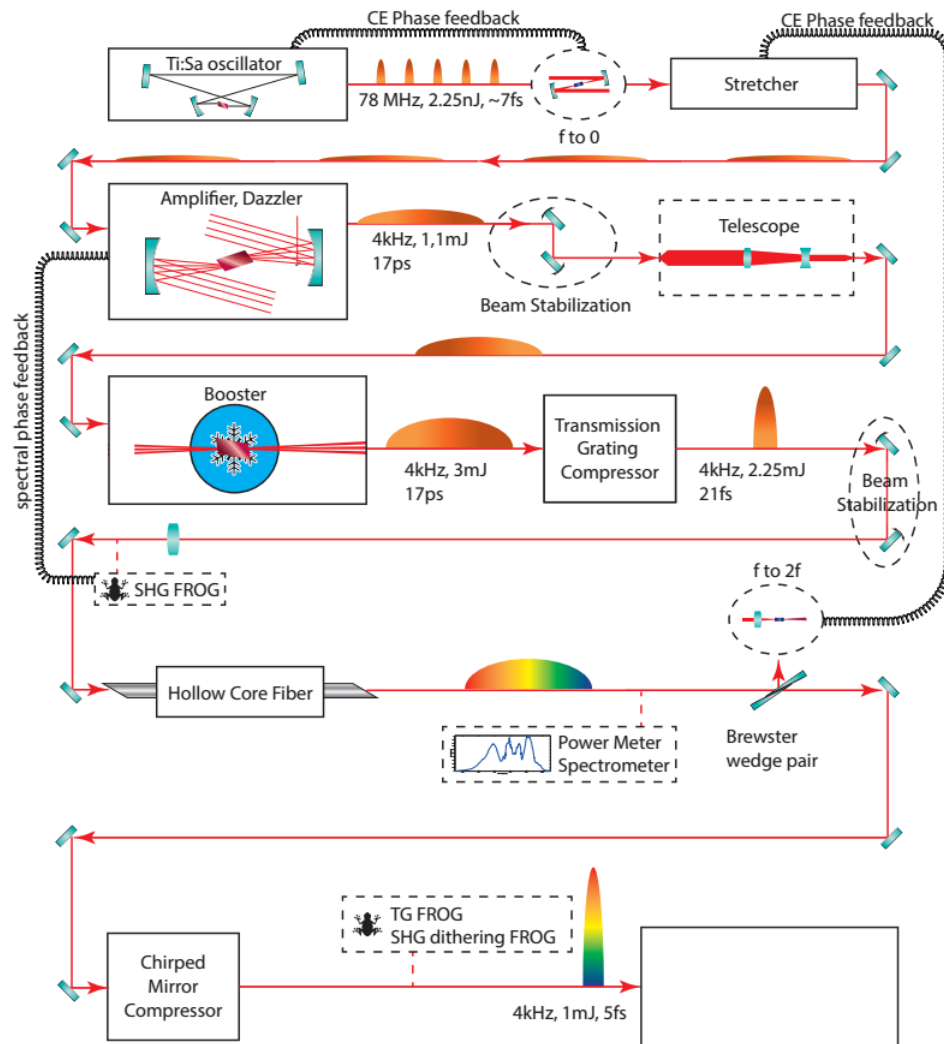


Figure 3.1: FP3 laser setup. See the text for description of the components and their function. Taken from Ref. [9].

Oscillator In the first stage, low-energetic femtosecond pulses are produced in a Kerr lens mode-locked titanium-doped sapphire oscillator (Femtolasers Rainbow). The oscillator is pumped by a continuous-wave (CW) frequency-doubled Nd:YVO4 laser (Coherent Verdi V6) operated at ~ 3.9 W, and produces laser pulses at a repetition rate of 80 MHz with pulse durations around 7 fs and pulse energies around 3 nJ. Even though the duration of these pulses is already short enough for applications, the pulse energy and power are far too low for efficient HHG. The CEP of the pulses from the oscillator is controlled via a feedback loop based on difference-frequency generation (DFG). Spectral broadening is achieved via self-phase modulation by focussing the pulses into a periodically-poled lithium-niobate crystal (PPLN)[73]. The then formed spectral overlap of the DFG signal with the primary spectrum contains the carrier-envelope offset frequency f_{CEO} . This frequency is used as feedback signal to modulate the pump laser power via an acousto-optical modulator (AOM).

Pulse amplification For efficient HHG, the pulse power and energy produced in the oscillator have to be raised by several orders of magnitude. In the present laser setup, the amplification is achieved in two subsequent stages with Ti:Sa crystals and is based on chirped-pulse amplification (CPA) [74]. Before reaching the first amplification stage, the pulses from the oscillator are stretched to around 17 ps by traversing two times a SF57 glass block of 13.5 cm length. This stretch is necessary to prevent crystal damage due to very high laser power. The stretched pulses are then guided multiple times through the Ti:Sa, which is cooled to 178 K and pumped by a 532 nm laser at 300 ns pulse length and 32 W power. After four passes, they are guided to a Pockels cell where the repetition rate is decreased from 80 MHz to 4 kHz. After the Pockels cell, the pulses run another five passes through the Ti:Sa and then leave the first amplification stage at pulse energies around 1.1 mJ. As the next step, the pulses are sent to the second amplification stage, the so-called booster, which comprises a three-pass Ti:Sa setup pumped by two mode-locked lasers at 532 nm (ETNA HP by Thales). The Ti:Sa crystal is cooled down to 58 K, which is a much lower temperature than in the first stage and reduces thermal effects such as lensing. As a result, the pulse energy has increased to 2.5 - 3.0 mJ.

Compression The pulse duration after the second amplification stage is 17 ps. A transmission grating scheme [75] is used to compress the pulses to 21 fs, which are then sent to a hollow-core fiber (HCF) filled with Neon. In the fiber, self-phase modulation leads to strong spectral broadening. The spectral range of the spectrum at the fiber exit is 400 nm-1100 nm, with pulse energy of about 1 mJ and pulse duration of 5 fs and less. The CEP of the pulses is stabilized using an

f-2f-scheme which is coupled to a motorized double-prism stage in front of the first amplification stage. This feedback loop then ensures control and stabilization of the CEP.

3.1.2 The FP2 laser setup

For a large part of the attosecond streaking studies conducted in this thesis, the laser setup FP2 was used. The schematic view of the setup is shown in Fig. 3.2.

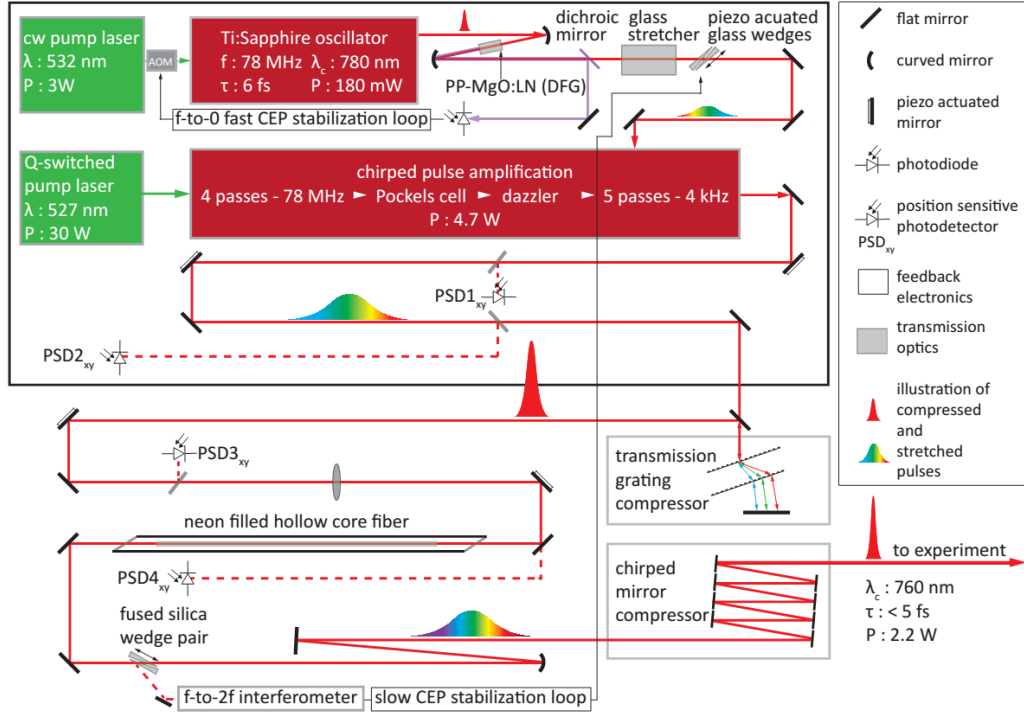


Figure 3.2: FP2 laser setup. Taken from Ref. [71]

The setup differs from the FP3 unit in the following aspects. The oscillator produces pulses of ~ 6 fs and ~ 3 nJ at a repetition rate of 78 MHz. The carrier-envelope offset frequency f_{CEO} is fed to an acousto-optical frequency shifter (AOFS) to stabilize the frequency comb of the oscillator and hence maintain CEP stability [76]. The Pockels cell output is 3 kHz rather than 4 kHz, and FP2 holds only one multi-pass Ti-Sa amplification stage. The final output after the HCF is 4 fs, 0.4 mJ, 550 - 1000 nm. The FP2 unit generates shorter pulses than FP3, but at considerably lower power. Still, it was possible in course of this work to perform high-quality streaking measurements up to 135 eV XUV energy. Further information about the FP2 setup can be found in Refs. [71, 72].

3.2 Streaking spectroscopy beamline

This section provides a description of the beamline, which was used throughout this thesis for the attosecond experiments [77]. After providing an overview of the whole setup, all of its relevant parts are discussed one by one. Further information can be found in Refs. [2, 77, 78].

3.2.1 Overview

A schematic view of the beamline is displayed in Fig. 3.3. The whole apparatus consists of five main components. The high-intensity NIR pulses enter the HHG chamber from the right and produce high harmonic radiation in the gas target. The NIR light co-propagates with the generated XUV field to the beam analysis chamber, where the spectrum of the XUV beam is characterized. The two colors then traverse the filter chamber, where they are spatially separated before they enter the experimental chamber, where the streaking spectroscopy experiments take place.

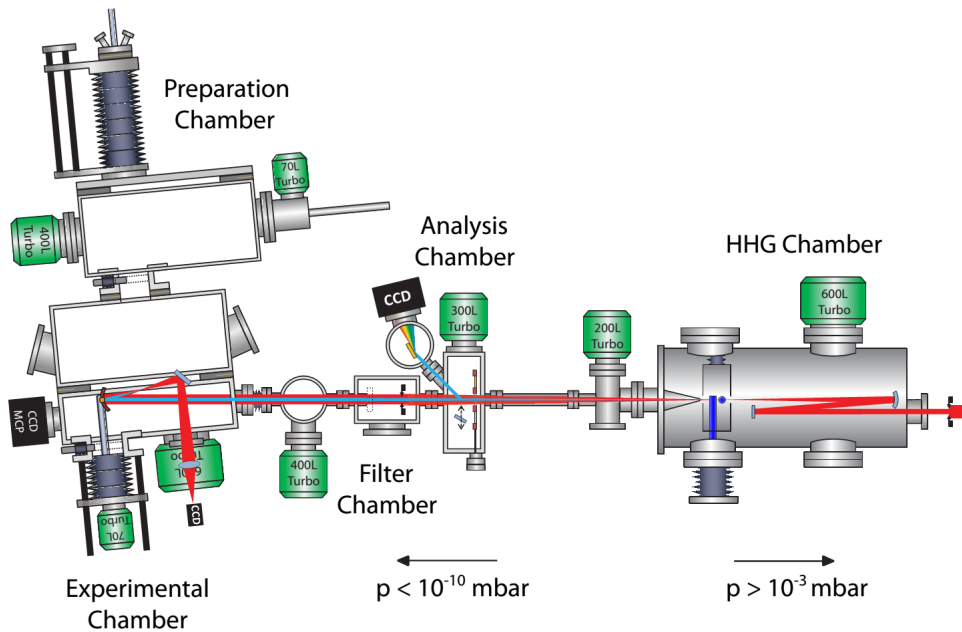


Figure 3.3: The streaking beamline [77]. Beam path from right to left. Figure from Ref. [2].

Also attached to the experimental chamber is the preparation chamber, which is used for preparation and characterization of the well-defined surface structures on

which attosecond experiments are performed. The experimental and preparation chambers are separated by a gate valve, to protect the experimental chamber from contamination due to the comparably higher pressure in the preparation chamber during sample fabrications.

3.2.2 High harmonic generation and attosecond pulses

High harmonic generation and characterization A schematic draw of the HHG setup is shown in Fig. 3.4 below [77]. The compressed NIR laser pulses trigger the generation of high-harmonic radiation via upconversion in neon, which is kept at constant pressure in a steel or ceramic target by a flow control valve. The beam enters the HHG chamber from the right through the iris A1, which is used to tune the laser intensity in the target, and impinges onto a flat silver mirror M1, which reflects the beam onto the focussing mirror M2. M2 focusses the beam into the neon gas target T, which can be moved in 3d.

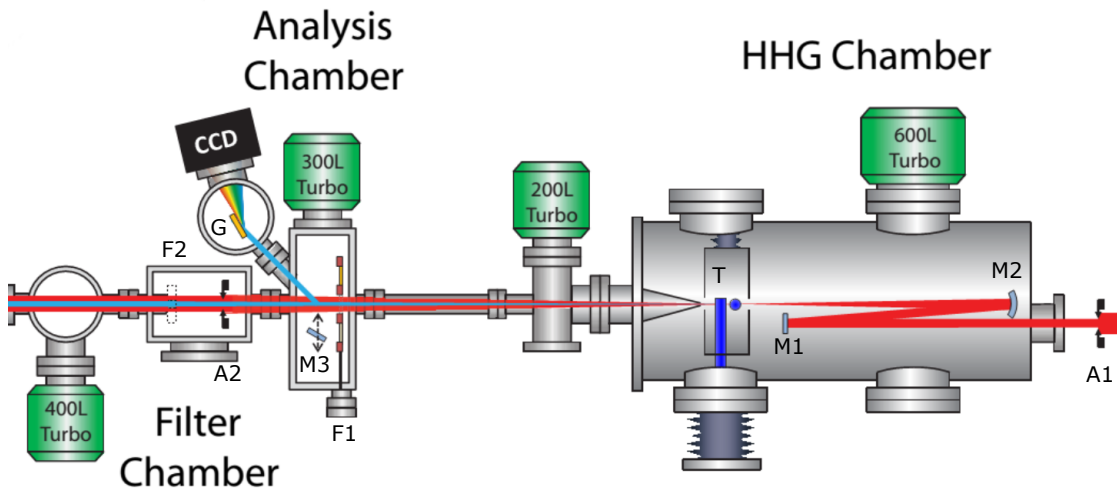


Figure 3.4: High harmonic generation and characterization unit. See text for details. Modified from [2].

The typical neon pressures are in the range of 150 - 250 mbar, and the stabilization of the pressure is mandatory, since the spectral shape and the overall flux crucially depends on the gas pressure [3]. After leaving the target, the NIR beam and the produced HH radiation propagate to the beam analysis chamber which contains a filter slider F1 and a flat silver mirror M3. F1 contains zirconium and palladium filters of several 100nm, which block the NIR light, and M3 reflects the XUV onto an ultrathin gold grating G, which spatially resolves the HH spectrum. A

CCD camera images the spectrum in real time and this spectrum is used for the optimization of the XUV flux and the cut-off region.

Beam separation After this analysis, the NIR light is unblocked and propagates together with the XUV beam into the filter chamber, where an iris A2 tunes the intensity of the IR to suitable values for the streaking experiments, which is 10^{10} - 10^{12} W/cm², and a pellicle F2 is used to spatially separate the two fields. The pellicle consists of an outer and an inner circular filter, arranged coaxially, such that the inner filter only transmits XUV, and the outer filter only transmits NIR. After passing a differential pumping stage, the light enters the surface science station, where a background pressure of 1×10^{-10} mbar or less is maintained. The beam path from the target to the surface science station is shown in more detail in Fig. 3.5. After passing the pellicle filters, the beam hits a double mirror assembly, which reflects the beam onto the sample, and the excited photoelectrons are then detected in the time-of-flight spectrometer (TOF).

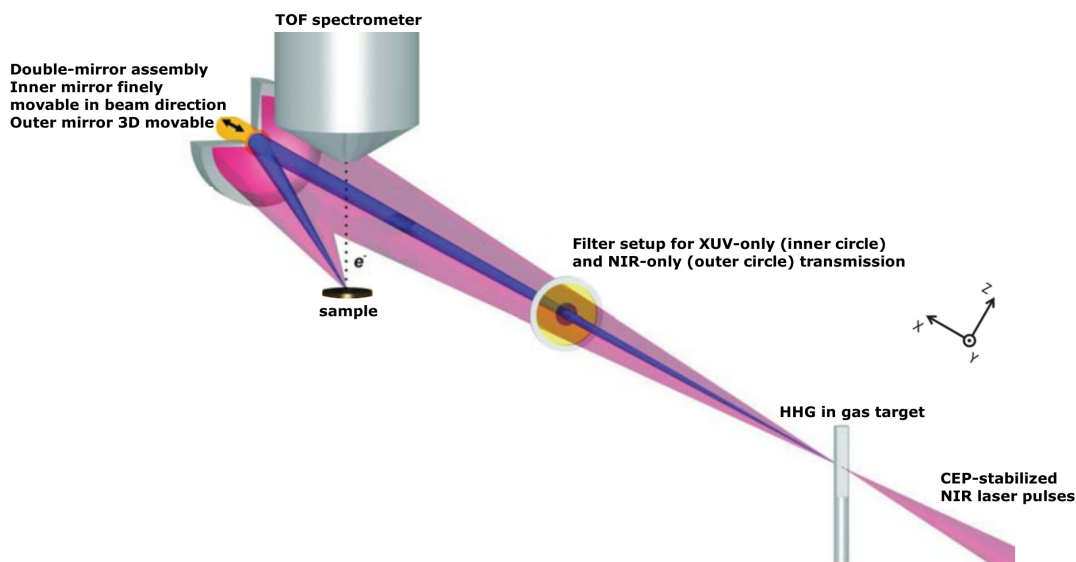


Figure 3.5: Beam path from the HHG set-up to the sample surface. The NIR light is drawn in red, while the XUV light is represented in blue. Modified from Ref. [1].

Attosecond pulse selection by multi-layer mirrors The double mirror is at the heart of the streaking technology. As shown in Fig. 3.5, it consists of an inner and an outer mirror, which are aligned coaxially. The outer mirror reflects the NIR streaking field onto the sample, whereas the purpose of the inner mirror is the selection of the isolated attosecond XUV pulses from the impinging high har-

monic spectrum. The delay between the arrival times of NIR and XUV fields at the sample surface is controlled by moving the inner mirror with respect to the outer mirror along the beam direction in well-defined steps. The movement of the XUV mirror is controlled via a nanometer-piezo-stage, and typical delay steps are 150 - 250 as. The XUV pulse selection is achieved by using multi-layered mirrors which reflect in the XUV spectral range. The central energy and bandwidth of the reflection can be tuned precisely by variation of the sophisticated layered structures. Recently, there has been tremendous progress in the field of these multilayer mirrors [44, 79, 80]. In the experiments presented in this thesis, four different mirrors have been used. For the magnesium studies, mirrors reflecting at 135 eV (3 eV FWHM) and 145 eV (3 eV FWHM) have been employed. The streaking spectroscopy on highly-oriented pyrolytic graphite has been done with 93 eV (4.5 eV FWHM) and 112 eV (5 eV FWHM). These mirrors will be discussed in more detail in the respective chapters. Besides the just mentioned projects, in course of this work a characterization of a reflector of unprecedented narrow bandwidth has been performed with the streaking method on GaAs samples [44]. In Fig. 3.6, the optical data of this mirror are shown. On the left panel, the bandwidth of 1.8eV and the central XUV energy of 112.6eV are demonstrated, and on the right panel, the signal obtained from photoelectrons excited by this radiation from a Gallium 3d level is illustrated. Clearly, the agreement between targeted and achieved reflectivity profile is very good.

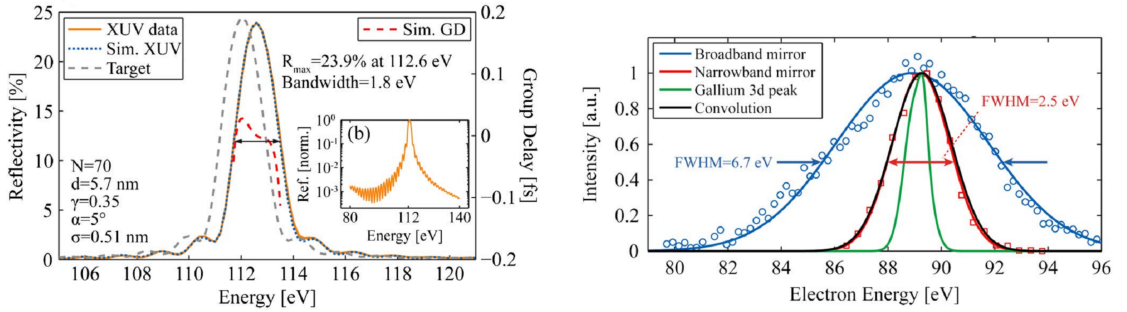


Figure 3.6: Narrow-bandwidth XUV reflector. Left figure: Targeted (grey) vs. measured (orange) reflectivity together with the simulated group delay (red). Right figure: Photoelectron signal from Gallium 3d level as excited by this narrow-bandwidth radiation [44].

After defining the XUV central energy suitable for the experiment, and after insertion of the corresponding multi-layer mirror into the double mirror set-up, the HHG spectrum must be tuned such that the targeted XUV energy lies well within the flat cut-off of the spectrum. Tuning is accomplished by adjusting the neon

gas pressure in the target, the dispersion of the NIR beam via a pair of fused-silica wedges, the CEP of the NIR and the NIR intensity in the target. Finally, well-isolated XUV pulses can be filtered by the multi-layer reflector and streaking spectrograms are acquired by recording photoelectron spectra from the sample as excited by the XUV pulse in the presence of the NIR field, as a function of the delay between NIR and XUV.

3.2.3 Surface science apparatus

The surface science station consists of two large vacuum vessels, the experiment and the preparation chamber, which are coaxially aligned and connected via a vacuum gate valve [77]. The two chambers are continuously pumped by strong turbo-molecular pumps to maintain a base pressure in the 10^{-11} mbar range and are equipped with mass spectrometers to analyze and monitor the composition of the residual gas. The chambers are shown in Fig. 3.7 below.

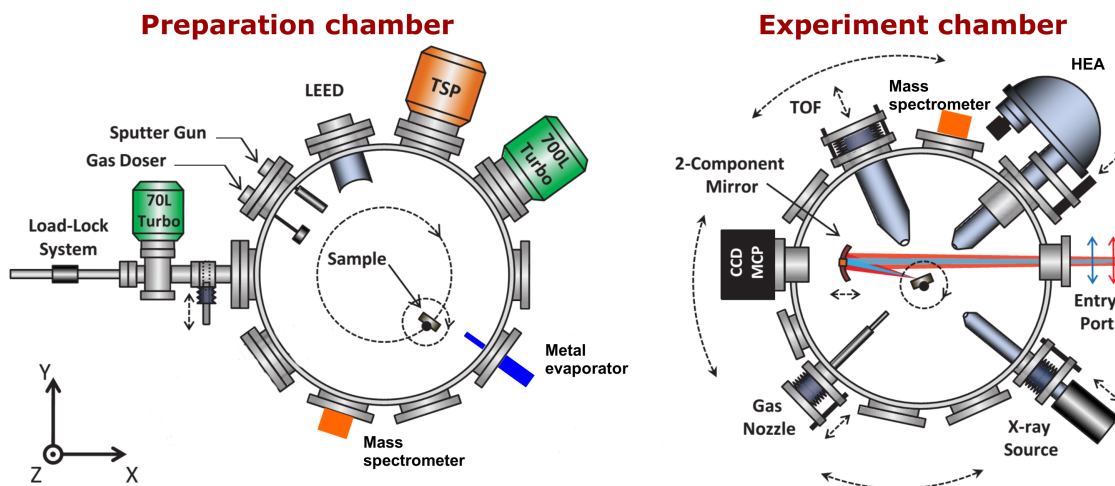


Figure 3.7: The preparation and experiment chamber of the surface science station. Both chambers are aligned coaxially. The sample resides on a manipulator arm which can rotate and thus be placed in front of the desired equipment. See text for description of the indicated components attached to the chambers. Figure modified from Ref. [2].

Preparation chamber The samples are mounted on a manipulator arm, which is connected to the preparation chamber and can be rotated such that the different analytical tools inside the chamber can be conveniently approached. The arm can be moved along the chamber axis to transfer the sample to the measurement

chamber. It can be manipulated in 3d. The samples can be cooled to cryogenic temperatures by liquid nitrogen and helium, and heated by radiative heating and electron bombardment to temperatures up to 2500 K. A load lock system is attached to the preparation chamber, as seen in the sketch on the left of Fig. 3.7. This enables to transfer the samples to the chamber without breaking the vacuum. The chamber is further equipped with a gas dosing system, which supplies high-purity helium, argon, hydrogen and oxygen. A sputter gun is used to clean the sample surface by ion bombardment. The low-energy electron diffraction (LEED) apparatus can be employed to check the surface structure and long-range order of the samples. The titanium sublimation pump (TSP) with an attached cryo-trap enables to maintain pressures in the low 10^{-11} mbar range. Metal or molecule evaporators can be attached to deposit thin metallic films or molecules *in situ*. As indicated on the left of Fig. 3.7, only metal evaporators have been used in the course of this thesis: A Knudsen-cell for the evaporation of magnesium and a ribbon-evaporator for tungsten, which will be described in more detail in the sections on the respective studies.

Experiment chamber The measurement chamber used for the attosecond streaking experiments, is equipped with an Al- K_α and Mg- K_α non-monochromatic X-ray source. This source, in combination with the hemispherical electron analyzer (HEA), allows stationary X-ray photoelectron spectroscopy (XPS) experiments. The HEA can in principle also be used for time-resolved XUVPS. However, only the time-of-flight (TOF) spectrometer (Stefan Kaesdorf, Geräte für Forschung und Industrie) has been used throughout this thesis to record the photoelectron spectra for the streaking spectrograms, because the XUV photon flux available in the period of this thesis was not sufficient yet to obtain good enough signal-to-noise ratios in an HEA experiment. The gas nozzle provides the opportunity for gas phase experiments. The CCD camera is employed to check the XUV mode. The two-component mirror is used to reflect the beam through a window out of the chamber onto another CCD camera, as an aid to align the temporal and spatial overlap of NIR and XUV fields. The double-mirror assembly serves to filter isolated XUV pulses from the cut-off of the HHG spectrum, to focus the NIR and XUV onto the sample and to tune the relative time delay between the arrival times of the XUV and NIR pulses at the sample surface, as already discussed previously.

During the period of this thesis, the chamber has additionally been equipped with a magnetic field compensation. In principle, the photoelectron trajectories between surface and TOF detector can be altered by residual magnetic fields of the earth and local sources. This effect will be different for electrons of different kinetic energies and can hence influence the retrieved photoemission timing. To

examine this effect quantitatively, an assembly of Helmholtz coils was mounted around the surface science station as shown in Fig. 3.8, to produce magnetic field strengths that compensate the residual fields. To this purpose, the sample holder at the end of the manipulator has been equipped with a set of small probe coils to measure the present fields at the measurement position of the sample. The current flowing through the band cables is then adjusted to compensate these fields. Attosecond streaking measurements have been performed on the well-established systems tungsten and magnesium, and data sets with and without active magnetic field compensation have been acquired. It has been shown that there is no significant effect of the magnetic fields on the retrieved time delay in the kinetic energy range relevant to the attosecond experiments which were performed in this thesis. The compensation procedure and the performed time-resolved measurements are presented in Ref. [81].

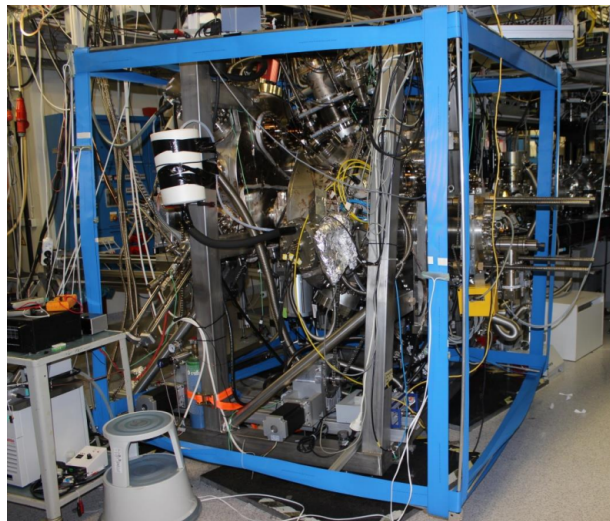


Figure 3.8: Coils of blue 64-pin band cables spanned around the surface science station in all three spatial directions for magnetic field compensation during attosecond streaking. From Ref. [81].

3.2.4 Time-of-flight (TOF) spectrometry

In this thesis, the kinetic energy distribution of the photoelectrons has been measured by the Käs Dorf TOF spectrometer mentioned before. In this spectrometer, the electrons travel a well-defined distance d in a field-free drift tube before they reach the detector. The time of detection t is measured with respect to a trigger signal which is precisely locked to the laser pulse. Through the relationship

$$E_{kin} = \frac{md^2}{2t^2}, \quad (3.1)$$

the time is directly linked to the kinetic energy E_{kin} of the electrons, under the assumption that the electrons do not experience any acceleration on their way into the spectrometer after the NIR-field is extinguished. This is not strictly satisfied, because the sample and the detector might have different work functions and hence the electron is accelerated due to the resulting potential difference. However, this offset is constant, and negligible for kinetic energy larger than 10eV , as satisfied for all experiments relevant for this thesis. The energy resolution ΔE_{kin} of the spectrometer and the transformation rule from TOF to kinetic energy are immediately obtained as the following analytic functions

$$\begin{aligned} \Delta E_{kin} &= \sqrt{\frac{2}{m}} \frac{2}{d} \Delta t E_{kin}^{3/2} \\ N(E_{kin}) &= N(t) \left| \frac{dt}{dE_{kin}} \right| = \frac{t^3}{md^2} \end{aligned} \quad (3.2)$$

where Δt is the temporal resolution of the TOF spectrometer, which is about 100 ps for the system used here. The default angular acceptance of the used Kaesdorf spectrometer is $\pm 2^\circ$. For the situations where the obtained electron flux was too low to obtain meaningful statistics in a streaking experiment, the transmission of the Kaesdorf spectrometer could be increased by applying kinetic energy dependent potentials to the built-in electrostatic lens. A maximal acceptance angle of $\pm 22^\circ$ was possible for lens voltages of up to 900 V. In this case, however, the analytic expressions above are not valid anymore and instead, trajectories had been solved numerically [2]. Results are shown in Fig. 3.9.

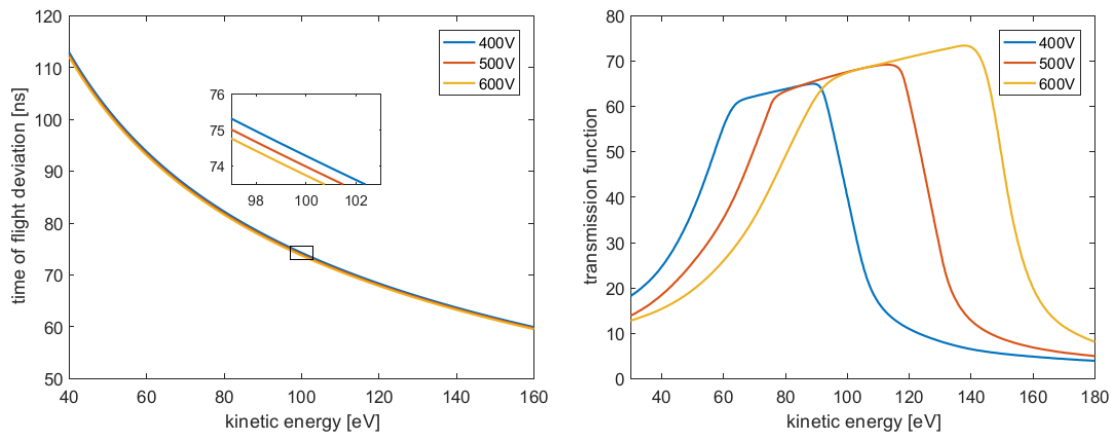


Figure 3.9: TOF to energy conversion and transmission functions of the employed spectrometer for different values of the electrostatic lens voltage.

Apparently, for any given lens voltage, the transmission function exhibits a plateau with relatively sharp falling and rising edges. As long as the kinetic energy of the photoelectron emerging from a certain level in the system under consideration lies well within the range of the plateau, the transmission is nearly constant over the corresponding peak region. However, if the peak region lies on one of the edges of the transmission curve, the magnification for different parts of electron signal is not the same. For the situation of a chirped XUV pulse, which implies chirped outgoing electron wave packets, this leads to a measurement artifact. Contributions to the signal, which are emitted at different times, are magnified differently [2]. This results in a change of the deduced photoemission timing, which can be very pronounced [8]. In general, the photoemission timing is compared for electrons emerging from a core state, and electrons emitted from the conduction band states, respectively. Due to the energy separation of these levels of several tens of eV, it is impossible to achieve similar transmission efficiency for the photoemission signal from both levels. In particular, one will always find at least one peak located on an edge of the transmission curve. This is highlighted below for the case of measurements on the Mg (0001) surface at an XUV photon energy of 145 eV.

For the higher voltage of 900 V, the signal from the conduction band states resides on the plateau, while the 2p region coincides with an edge of the transmission curve. On the contrary, for the lower voltage of 475 V, the 2p emission signal is transmitted homogeneously, while the conduction band emission appears on the edge. The laser systems operate at repetition rates of 3 kHz and 4 kHz, respectively, which implies a minimum time of $250\mu\text{s}$ between subsequent shots.

This temporal window is easily sufficient to implement a lens switch electronics to set the lens voltage to 900 V every even and to 475 V every odd shot. In this way, two streaking spectrograms are acquired. Only the streaking trace which was recorded in constant transmission is selected from the spectrograms, and these two traces are then combined to obtain the final spectrogram from which the relative timing can be retrieved. This electronics was already operational before this thesis, and could be used. However, studies on magnesium and generally for any situation where one of the levels has much lower cross-section than the other one, this procedure is not practical. If the high voltage at the MCP is ramped up sufficiently to acquire enough signal from the weak level, the strong level runs into saturation. This issue has been tackled by designing a shot-to-shot switching electronics for the MCP voltage. Therefore, it became possible to switch MCP voltage and electrostatic lens voltage shot-to-shot which enables to optimize the count-rates for the two levels independently and avoid both the transmission edge and the saturation problems. The successful operation of this switching electronics is illustrated in Fig. 3.10 and 3.11. It has been used in the course of this thesis for the acquisition of streaking data from magnesium with large acceptance angle, at XUV photon energies 135 eV and 145 eV.

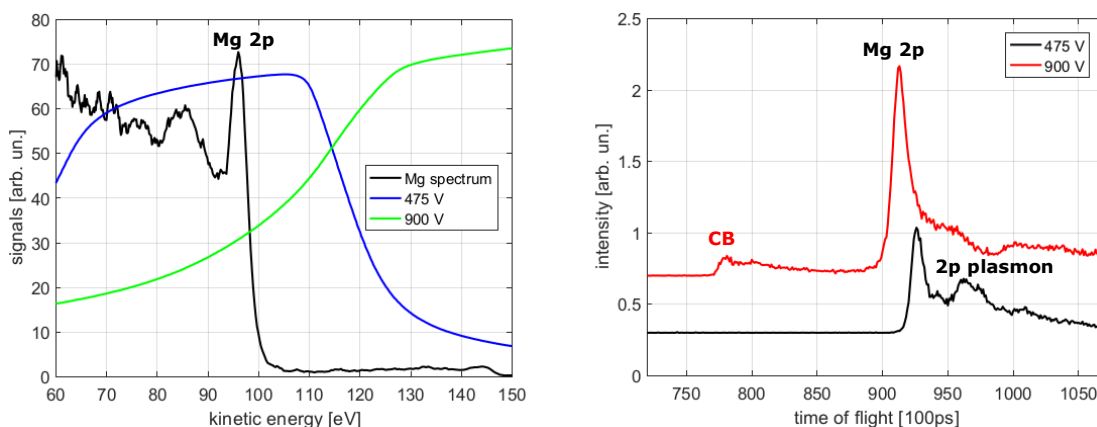


Figure 3.10: Mg(0001). (145 eV XUV). Left: magnesium XUV spectrum excited by 145 eV attosecond XUV pulses is shown together with the transmission curves for two lens voltages which are chosen to uniformly magnify the 2p and the conduction band region, respectively. Right: Lens voltages of 475 V and 900 V. At 900 V, the conduction band region is significantly magnified, while the Mg 2p region is saturated. At 475 eV, the valence band signal is not discernible, while the 2p region is nicely resolved. The 900 V spectrum is shifted to shorter flight times with respect to the 475 V spectrum.

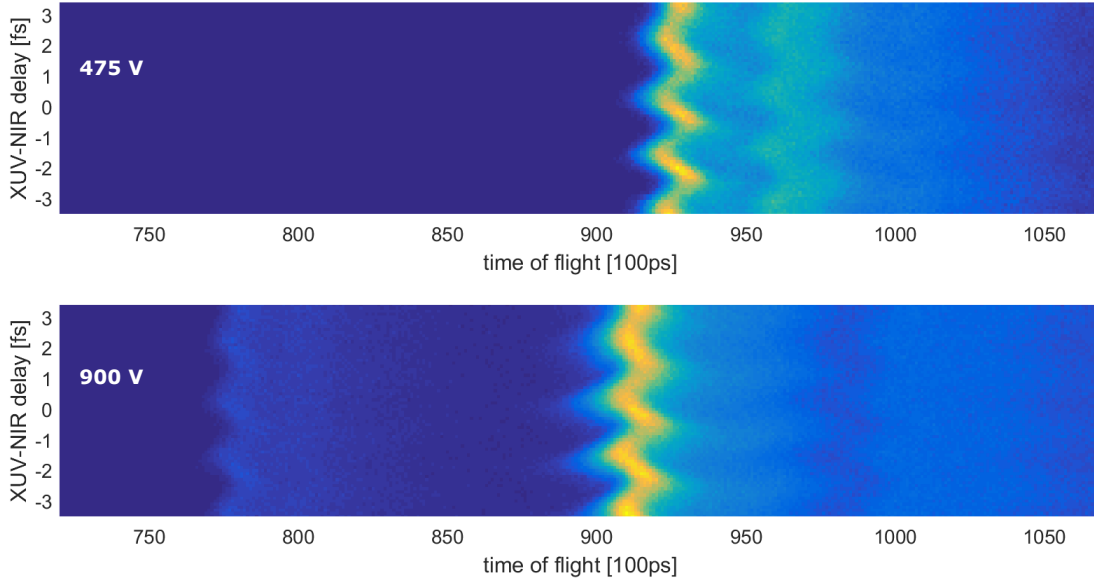


Figure 3.11: Mg(0001) at 145 eV XUV central energy. Lens voltages of 475 V and 900 V. Comparison of the streaking spectrograms for the two settings.

3.3 Streaking data evaluation

In the acquired streaking spectrograms, the properties of the XUV attosecond and NIR femtosecond pulses as well as of the outgoing electron wave packets and of the temporal structure of the photoemission process itself are encoded. This section describes the methodology to decipher this information. After the streaking spectrogram has been recorded, the TOF data are converted from the time to the energy domain, as it was already indicated in Sec.3.2.4. Afterwards, the signal from the inelastically scattered electrons is subtracted from the spectrogram, as will be discussed in Sec.3.3.1 below. From the background-corrected spectrograms, the important parameters of the XUV and NIR pulses and the attosecond photoemission delays are retrieved by a MATLAB algorithm which is based on the solutions to the time-dependent Schrödinger's equation. This algorithm will be described in Sec.3.3.2.

3.3.1 Background subtraction methods

Two background subtraction techniques have been employed and their results were juxtaposed to check for consistency. One approach is based on the removal of a Shirley background, which stands as a well-established procedure in stationary

photoemission spectroscopy and was introduced by Shirley in 1972 [82]. In this approach, a constant electron energy loss function is assumed and the background signal at a given kinetic energy of the electrons is calculated to be proportional to the integrated photoelectron signal at higher energies. In this thesis, the range of interest of an individual photoelectron spectrum includes up to two major peaks, which typically originate from photoemission from a shallow core level and the valence band, and the region in between. Therefore, the background has been subtracted by a splitted-Shirley method, which has been proven useful [2] and been extensively discussed [3]. The splitted method is defined by removal of the Shirley background for the spectral regions of all major peaks independently. The second approach which has been followed in this thesis is instead a differential method. Under the assumption, that the inelastically scattered electrons are not coherent with the primary electrons and thus the background spectrum does not change with the XUV-NIR delay, the background signal can be removed from the spectrogram by calculating the derivative of the spectrogram along the delay axis [83]. More precisely, this assumption is at stake, as it has been shown that plasmon loss lines in magnesium show streaking as much as the primary 2p state signal does, which implies that the plasmon signal adds coherently to the primary signal.

3.3.2 Attosecond retrieval

After the background has been subtracted from the spectrogram, the spectrogram is analyzed in several steps. The analysis algorithm is a fitting routine based on the solutions of the time-dependent Schrödinger's equation, designed to retrieve NIR and pulse properties such as chirp, duration, width and photoemission time delays.

Center-of-Energy estimates To obtain fitting results of good quality, it is necessary to provide starting values for the fit parameters for the properties of the laser fields, especially for the vector potential of the NIR. To this end, it is convenient to use a first-moments approach, in which, for each delay step in the streaking spectrogram, the center-of-energy (COE) of the relevant peaks is determined. For each peak, the shift of the COE in energy as a function of delay reads

$$\Delta E(\tau) = \frac{\int P(E, \tau) E dE}{\int P(E, \tau) dE}. \quad (3.3)$$

$P(E, \tau)$ is the amplitude at energy E and delay τ , as written in Eq.2.11, and where the integrals are calculated over the spectral range of the peak. Thereafter, a sinusoidal Gaussian-enveloped function is fitted to the set of COE points, to retrieve the vector potential of the NIR.

Quantum-mechanical retrieval Now, as introduced in the last chapter, it is necessary to pick parametrizations for the function $f(t)$, which incorporates temporal evolution of the XUV pulse and the matrix elements of the electronic transitions, and the vector potential $A(t)$ of the NIR field. These are parametrized as Gaussian

$$\begin{aligned} f(t) &= \sqrt{f_0} \times e^{-4\ln 2(t/\tau_{XUV})^2} \times e^{ibt^2} \\ A(t) &= A_0 \times e^{-4\ln 2(t/\tau_{NIR})^2} \times \sin(\omega_{NIR}t + \phi_{CE}), \end{aligned} \quad (3.4)$$

where A_0 is the amplitude of the potential, b is the chirp of the outgoing electron wave packet, ω_{NIR} the NIR carrier frequency, τ_{NIR} and τ_{XUV} are the temporal width of the pulses and ϕ_{CE} is the carrier-envelope phase (CEP). The parameters are then optimized such that the fit reproduces the spectrogram best. The whole retrieval has been implemented in a MATLAB environment [83]. It provides a user-friendly graphical user interface and enables fast and reliable data analysis, as batch processing is available and the results for all relevant parameters is saved in a way convenient for post-processing.

3.4 Scanning tunneling microscopy (STM)

In 1982, Binnig and Rohrer measured the tunnel current of electrons between a conducting surface and a metallic tip induced by an applied bias to be exponentially dependent on the vacuum gap width [84]. This discovery paved the way for their invention of scanning tunneling microscopy (STM) [85]. In this method, the surface is scanned by a metallic tip and a bias is applied between tip and surface. The tunneling current is recorded as a function of position and the topological and electronic structure on the surface is imaged with atomic resolution. The microscopy can be run in different modes, among which the so-called constant-current and the constant-height mode are the most prominent. In the constant-current mode, upon scanning the surface, the tunneling current is kept constant by continuously re-adjusting the tip-surface distance. In the constant-height mode, the surface is scanned at a fixed tip-surface distance. The tunneling current I also depends on the magnitude and sign of the applied bias V . Recording the tunneling current as a function of the bias allows one to obtain the dI/dV -relation from which detailed information on the electronic structure and density of states can be inferred. This so-called scanning tunneling spectroscopy (STS) method was first discussed in 1985 by Selloni et al. [86]. In the course of this thesis, STM and STS have been used to characterize highly-oriented pyrolytic graphite (HOPG) and tungsten deposits on the latter. To this end, a low-temperature STM has been used. The setup is shown in Fig. 3.12.

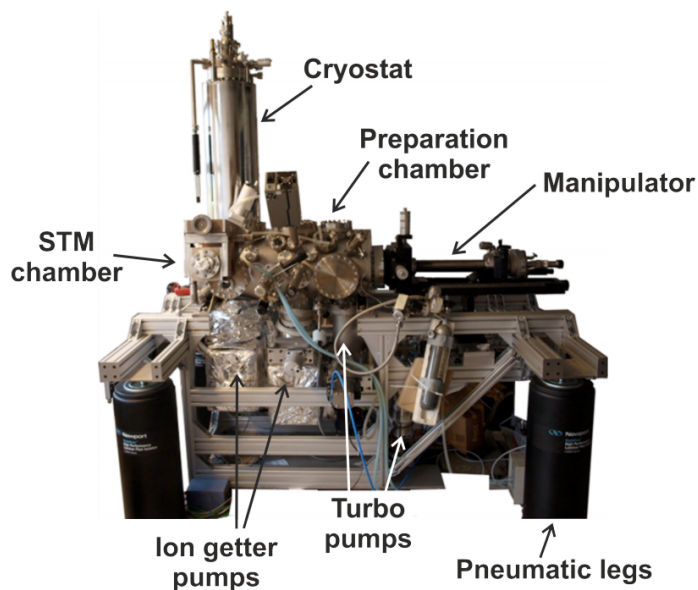


Figure 3.12: The low-temperature STM setup. Taken from Ref. [87].

The STM operation relies crucially on the presence of pneumatic legs to decouple the very sensitive apparatus from external vibrations. The setup consists of two chambers which are pumped down by turbo molecular pumps and ion getter pumps and are connected via a vacuum gate valve. On the left of Fig. 3.12, the chamber housing the STM itself and the cryostat mounted on top of the chamber are visible. The manipulator shown on the right end of the figure is used to hold the sample and to transfer it from the preparation chamber to the STM chamber. Metal and molecule evaporators can be connected to the preparation chamber to enable *in situ* deposition of adsorbates. The samples can be transferred into the preparation chamber via a load lock system, so that the chamber vacuum is not broken upon sample exchange. This setup was used in this work to record the data that are described later in this thesis, concerning the initial stage of growth of metallic tungsten on highly-oriented pyrolytic graphite.

Chapter 4

Attosecond streaking spectroscopy on HOPG

One of the major tasks of this thesis was the investigation of the temporal characteristics of photoemission from the valence band of highly oriented pyrolytic graphite (HOPG). Attosecond streaking measurements have been performed at the XUV photon energies of 93 eV (4.5 eV FWHM) and 112 eV (5 eV FWHM). For these excitation energies and bandwidths, the valence band photoelectron spectrum shows two partially resolved peaks. A time delay between the photoemission signals of the lower binding energy peak and the higher binding energy peak was measured. The present chapter describes the crystal structure of HOPG and addresses the response of the material to incident near-infrared light. It reviews previous time-independent spectroscopy and band structure results obtained for HOPG and identifies the relevant transitions which contribute to the two peaks seen in the photoemission signal. In the light of these considerations, the outcome of the attosecond measurements performed in this work is elucidated. In particular, the results are compared to a theoretical model for attosecond streaking from HOPG proposed by Christoph Lemell which yields good agreement with the experimental data of this thesis [41]. The interpretation of photoemission delays in solids is hampered by the entanglement of various possible sources, such as the propagation delay arising from the finite travel times of electrons inside the solid before photoemission. This contribution is absent for atoms in the gas phase and strongly suppressed for monolayers and two-dimensional clusters. Studies of the latter would allow deconvolving the propagation contribution. Significant streaking data are available for three-dimensional tungsten [2, 3, 8, 9]. In this thesis, ultrathin films of tungsten have been deposited on HOPG and characterized by STM, and the successful realization of a two-dimensional system has been demonstrated. This experiment forms the basis for possible future 2D experiments on tungsten and is discussed in the last section of this chapter.

4.1 Material characteristics

This section gives insight into the material properties of HOPG. The crystal structure of HOPG and optical properties of the material in the NIR spectral range are reviewed and the band structure of the material is discussed.

4.1.1 Crystal structure

Carbon exists in different allotropes, of which diamond, fullerenes, the strictly two-dimensional graphene and graphite are prominent examples. The experiment presented in this chapter has been carried out on highly oriented pyrolytic graphite (HOPG) [88, 89]. HOPG forms a stack of carbon layers, where each layer exhibits the honeycomb graphene lattice structure and the tilt of adjacent layers is less than 1° .

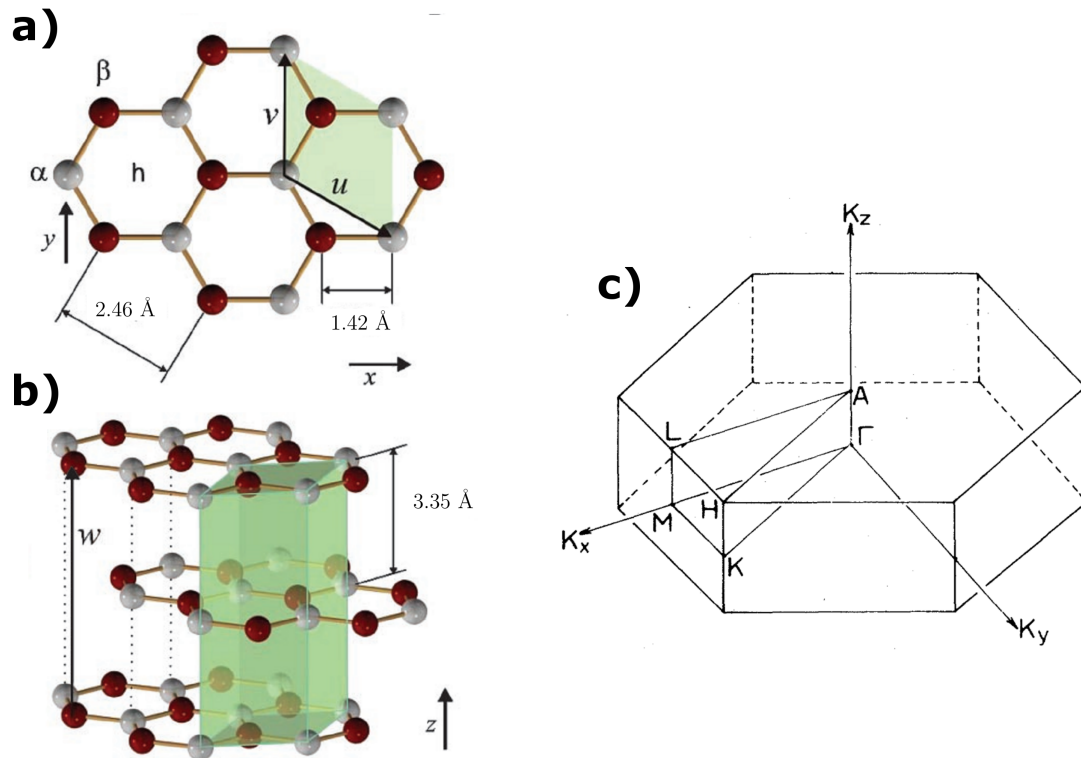


Figure 4.1: Crystalline structure of HOPG. For details, see the text. The panels a) and b) show the real-space lattice. Figure is taken from Ref. [90]. a) Top view of the surface layer. The unit cell of the hexagonal lattice is shaded in green. b) Perspective view, showing the layered structure. Panel c) illustrates the first Brillouin zone of HOPG. Figure is taken from Ref. [91].

The material does not occur in nature and is typically produced by stress recrystallization, as first described in Ref. [92]. The crystalline structure of HOPG is shown in Fig. 4.1. In the real space, HOPG is described by the hexagonal Bravais lattice with a two-point basis, as displayed in the panels a) and b). The hexagonal surface lattice is defined by two unit vectors, u and v , in the XY-plane with a length of 2.46 Å and an angle of 120°. The basis of the lattice is given by a pair of carbon atoms, displayed in white and red, respectively, with a distance of 1.42 Å. The lattice is thus formed as a honeycomb web of hexagons. The distance between layers is 2.36 times the next-neighbor distance of atoms within one layer, and the bond between atoms from different layers is weak. The white atoms (α) are directly above a white atom in the plane directly underneath at a distance of 3.35 Å; the red atoms (β) are over centers of the hexagons underneath (h). The third unit cell vector w is parallel to the z-axis with a length of 6.69 Å. The corresponding first Brillouin zone of HOPG is shown in panel c). The streaking experiments on HOPG which were performed in the course of this thesis were conducted in normal emission geometry such that predominantly electrons emitted perpendicular to the surface, i.e. in the Γ -A direction, were detected.

A further important property of the different phases of carbon is the configuration of the valence electrons. The ground state configuration of a single carbon atom is $1s^2 2s^2 2p^2$, but this configuration may change in condensed matter. In graphite, for instance, one of the $2s$ -electrons of the atom is lifted to a $2p$ orbital, such that one of the $2p$ -electrons is then found in a p_z state and the three electrons in $2s$, $2p_x$ and $2p_y$ form hybrid states which lay in the (x-y)-plane. This configuration is called sp^2 -hybridization. It distinguishes graphite from the phase of diamond which exhibits sp^3 -hybridization. In previous works, HOPG has been investigated by scanning tunneling microscopy (STM) and atomic-force microscopy (AFM) experiments and the surface of HOPG is an established standard for the calibration of STM and AFM setups [93, 94]. HOPG is also used for the production of X-ray monochromators [95]. As seen from Fig. 4.1, adjacent honeycomb planes are shifted with respect to each other in such a way that there are two distinguishable types of atoms: Half of the atoms have nearest neighbors along the direction perpendicular to the honeycomb sheets (white, α), and the other half of the atoms only have next-to-nearest neighbors (red, β) and sit in the center of hexagons of the nearest planes. Hence, there exist two axes in the direction perpendicular to the surface with one atom per layer and one atom per two layers, respectively. This crystal structure leads to a different electronic density of states (DOS) near the white and red atoms, respectively. An STM picture yields a triangular pattern of the red atoms rather than the true hexagonal surface lattice because it probes the DOS of the sample, which is larger near the red atoms. On the contrary, an

AFM picture will unravel the complete honeycomb pattern, because it is sensitive to the van-der-Waals interactions between the atoms of the sample and the tip, which are of similar strengths for atoms from the red and white group. Fig. 4.2 shows STM and AFM pictures of HOPG, and hexagons of white and red atoms are placed into the figures to ease identification [90]. The triangular pattern returned by the STM picture and the fully-resolved hexagonal structure seen in the AFM are clearly discernible.

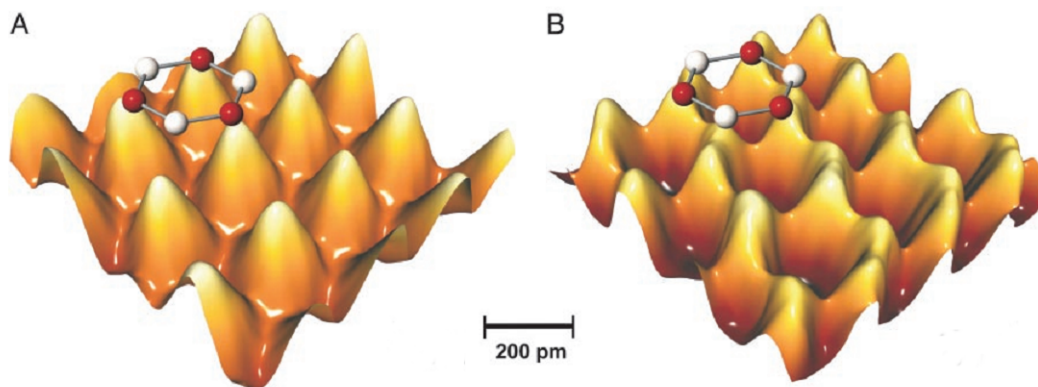


Figure 4.2: (A) STM image of graphite. The basis in the hexagonal unit cell of graphite consists of one white and one red atom, but STM shows only the red atoms, which form a trigonal lattice. (B) AFM image of graphite. The complete hexagonal carbon rings are visible. Modified from Ref. [90].

HOPG samples of very good quality are commercially available, and surface preparation methods are well-established. The bonds between adjacent basal planes in HOPG are small due to the weak π -bonds formed between atoms of adjacent layers, while the σ -bonds between atoms of the same layer are very strong. A well-defined clean surface can thus be obtained by sticking adhesive tape on the sample surface and pulling it off slowly. This so-called cleaving procedure peels off a few layers and the resulting surface shows the clean and well-defined honeycomb structure. In the experiments of the present work, the sample was cleaved ex-situ, transferred to UHV and annealed for 60 minutes at 500 K.

4.1.2 Interactions with NIR light

To interpret the results obtained in the streaking experiments on HOPG, it is crucial to understand the interaction between the HOPG substrate and the NIR streaking field. In the geometry applied for the experiments in this work, the incident NIR light wave was linearly polarized in the plane given by the direction

of incidence and surface normal, and the angle of incidence against the surface normal was 75° - 79° . The surface of the used HOPG crystal was parallel to the basal planes. The electric field of the NIR pulses can be decomposed into its components perpendicular and parallel to the surface normal. Due to the anisotropy of the crystal structure of graphite, as described above, the penetration depth of the light will be different for the two components. The high conductance parallel to the layers will lead to a rather efficient screening of the field component perpendicular to the surface normal, while screening of the parallel component will be hampered by the very low conductance in this direction.

Experimental and theoretical studies on the optical functions of HOPG exposed to NIR light are reported in Refs. [96, 97]. The authors showed that for light polarized parallel to the graphite layers, the optical response is metallic, while the material behaves like a semimetal for perpendicularly polarized light. For the latter, light penetrates deeply into the solid to depths of several μm , exceeding by far the emission depth of the photoelectrons of few \AA [98]. This is in contrast to free-electron materials like magnesium, for which screening lengths of the NIR of less than one atomic spacing have been demonstrated in attosecond experiments [69]. As a result of refraction of the incident beam at the vacuum-graphite interface, the electric field component parallel to the surface normal will be decreased inside the solid. Still, it has to be carefully taken into account, since the NIR streaking field reaches the deeper layers quasi-instantaneously¹ and probes the photoelectrons directly at their parent atom. This motivates to treat the system to some extent as an ensemble of two-dimensional hexagonal layers rather than a three-dimensional solid. In particular, electron transport is expected to play a negligible role in attosecond photoemission delays. At high intensities of the NIR involved in streaking experiments, photoelectrons are excited from the investigated surface by above-threshold ionization (ATI). In this highly nonlinear process of ATI, the photoelectron is created by multi-photon absorption [99]. The energy of the ATI electrons can easily exceed several tens of eV. The excitation of ATI electrons by NIR femtosecond pulses was investigated elsewhere [100]. ATI electrons need not be taken into consideration for the streaking experiments performed in this thesis. By tuning the NIR intensity and optimizing the streaking alignment, streaking amplitudes of several eV have been obtained while keeping the maximum energy of the ATI signal way below the energy of the XUV-induced photoelectrons.

Furthermore, it has been demonstrated that laser fields at high fluences and after long exposure times can induce changes in electronic and lattice structure of HOPG [101]. Here it has been shown that excitation of the HOPG surface by 10^4 NIR

¹Light traverses the interatomic distance of HOPG in 1 as.

laser pulses of 80 fs duration, at fluences² of the order of 60 mJ/cm² and above lead to slight inward displacement of surface layer atoms by 0.5 Å and to a change of hybridization to sp³. It was stressed that the obtained configuration is not identical to diamond but was claimed to be a unique phase induced by the femtosecond excitation. This phase was characterized by scanning tunneling microscopy (STM) and spectroscopy (STS) and thus discriminated from the usual HOPG structure. STM pictures displayed in Fig. 4.3 show the excitation as bright circular domains (BCD).

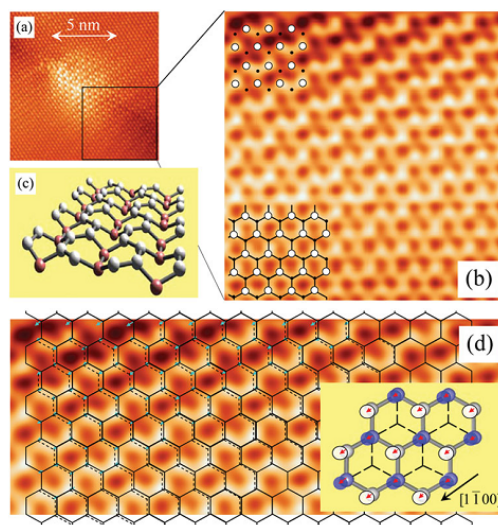


Figure 4.3: (a) A typical STM image of the HOPG surface acquired after excitation with 10^4 laser pulses, at fluence of 64 mJ/cm². Images were acquired with a Pt-Ir tip at a voltage of +100 mV. (b) The image acquired at a voltage of -40 mV for the region shown by a rectangle in (a) with an expanded scale. (c) A schematic model for the laser-altered configurations in the BCD. (d) Displacement of the center of each protrusion in the upper half of (b). The solid honeycomb lattice represents the original carbon-atom site on the pristine surface. The dotted lattice is formed by combining the centers of observed protrusions. Taken from Ref. [101].

In principle, the described effect can result in a change of the temporal characteristics of photoemission. However, under the experimental conditions of the measurements of the thesis, the effect can be neglected. In Ref. [101], no structural changes have been observed in the surface for fluences less than 60 mJ/cm² even for 10^6 laser pulses. The laser intensity in the HOPG experiments of this thesis never exceeded 10^{10} W/cm². Given the pulse durations of 5 fs and less, the

²Fluence is the optical energy per unit area delivered by the laser pulse.

fluence was thus kept well below 0.05 mJ/cm^2 . In another study, conducted with laser pulses of 150 fs duration at fluences of 4 mJ/cm^2 the observation of laser-induced periodic surface structures (LIPSS) was reported on multi-layer graphene samples [102].

4.1.3 Bandstructure and valence band spectrum

Knowledge of the bandstructure of HOPG, in particular for high final-state energies, and understanding of the details of the valence band photoelectron spectrum is mandatory for the interpretation of streaking data. This section contains a discussion of experimental and theoretical results obtained elsewhere, which will give insight into the characteristics of both band structure and valence band photoemission spectrum of HOPG.

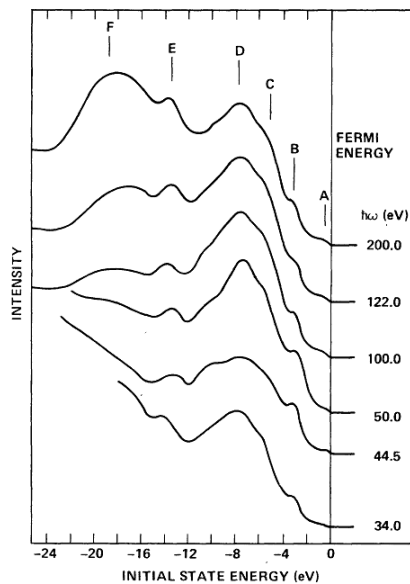


Figure 4.4: Photoemission spectra for different XUV energies of the graphite valence band at varied excitation energy [103]. The labels A-F highlight the prominent features of the spectrum in Ref. [103] to relate to the discussion therein.

In a previous study, the photoemission spectrum of graphite was investigated by ultraviolet photoemission spectroscopy for varying photon energies in the range of 30-200 eV [103]. The angle of incidence for the light was 75° to the surface normal, the polarization vector was in the plane spanned by incident light and surface normal, and a cylindrical mirror analyzer (CMA) was used. The graphite

valence band spectra of Ref. [103] are shown in Fig. 4.4, and consist of several distinct features whose relative intensities depend rather strongly on the excitation energy. The prominent features are labeled A-F and their origin can be understood by band structure considerations and complementary spectroscopic studies. It is instructive to study the valence region by X-ray-emission spectroscopy (XES).

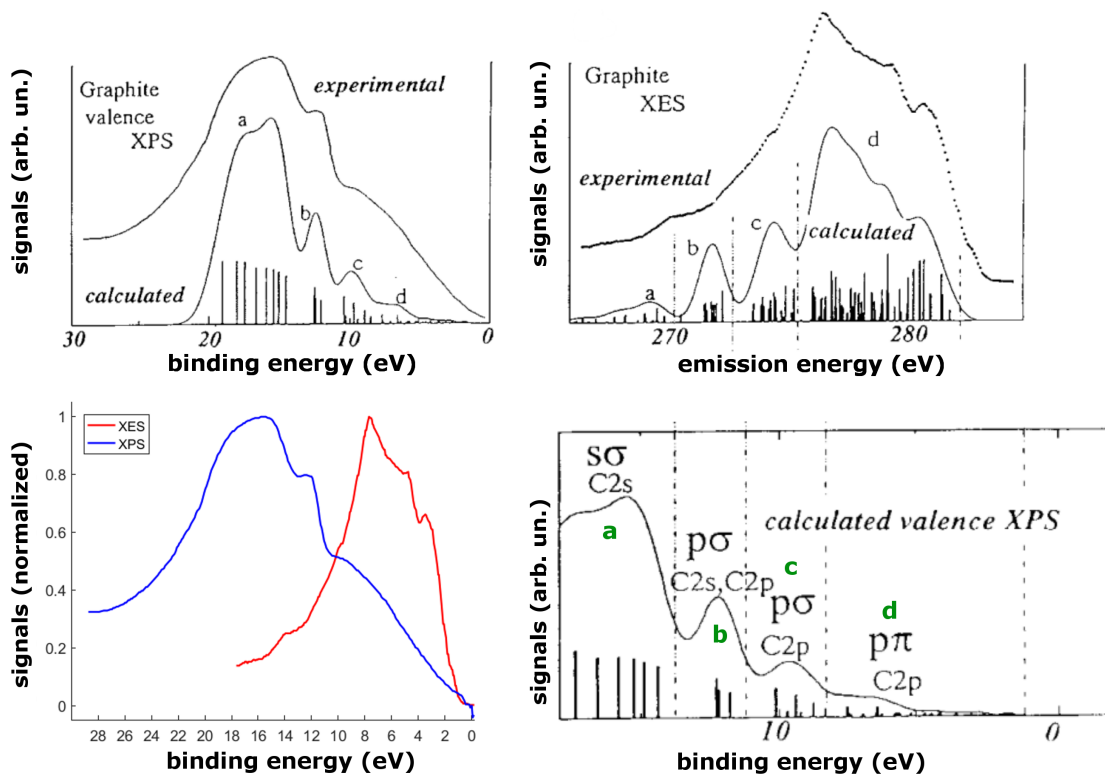


Figure 4.5: XES and XPS spectra from graphite. Upper left/right panel: Experimental and calculated XPS/XES spectra [104]. Lower left: Experimental spectra on merged energy axis for better comparison. Lower right: Assignment of orbital character to the individual peaks in the spectrum, adapted from Ref. [104].

XES is sensitive to p -states much more than s -states, due to the dipole selection rule for $p \rightarrow s$ transitions. Further, for energies far from the ionization threshold, XPS is much more sensitive to the s -states of graphite, on account of the very low ionization cross-sections of the p -states with respect to the s -states. Hence, the combination of XPS and XES spectra of graphite allows to distinguish between contributions of s - and p -character, respectively. Moreover, density-functional theory (DFT) is a valuable quantum-mechanical tool to investigate the electronic structure of many-body systems [105–107]. By DFT calculations, XPS and C- K_α

XES spectra from graphite were analyzed and interpreted [104]. The authors were thus able to disentangle p - and s -derived contributions to the valence band. As shown in the upper panels of Fig. 4.5, the valence band spectrum exhibits four distinct features which are labeled a-d. Their relative intensity is very different for the XES spectrum on the right and the XPS spectrum on the left, respectively, as rationalized above. By comparing the XES and XPS experimental curves directly on a merged energy axis, as illustrated in the lower left panel of Fig. 4.5, it can be seen that the part of the spectrum from 0-10 eV binding energy consists mainly of p -derived density with lower contribution from s states, while the part from 12-30 eV is dominated by s -derived density.

By the quantitative DFT analysis, it was possible to identify the orbital characteristics of all four features a-d [104], as shown in the lower right panel of Fig. 4.5. Feature a is assigned to the $2s$ -orbital, while b is a mix of $2p$ and $2s$ and c and d derive from $2p$ -orbitals. In a more recent work, Lechner et al. were able to distinguish the $2p_z$ density of states (DOS) in HOPG from the $2sp_{xy}$ DOS via band structure calculations using ab initio level calculations for different Hamiltonians [108]. They performed calculations using the method of all-electron Gaussian-type functions (GTF), and also delivered another set of calculations employing projector augmented wave (PAW) basis sets. The results for both the projected band structure and the DOS are shown in Fig. 4.6 below.

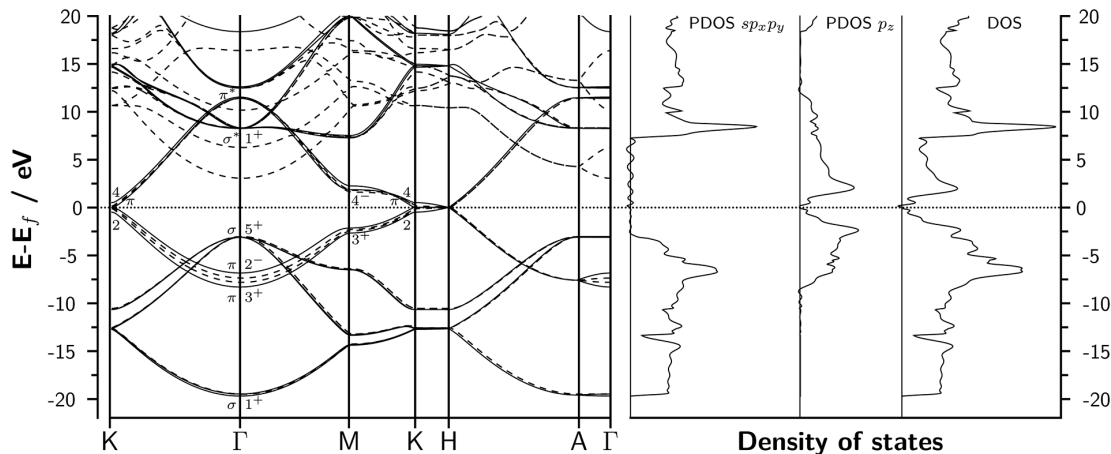


Figure 4.6: Band structures and density of states (DOS) of HOPG obtained at the PBE level. Left panel: Calculated band structures with GTF (full lines) and PAW (dashed lines). Right panel: Projected density of states on the $2s2p_x2p_y$ AOs (PDOS $sp_x p_y$) and on the p_z AOs (PDOS p_z) and total density of states (DOS) [108].

By inspection of the right panel of Fig. 4.6, the p_z projected DOS extends only from 0-7 eV, while the $2s2p_x2p_y$ projected DOS extends from 3-20 eV and beyond. As explained in the previous chapter, the assembly of the time-of-flight spectrometer allows tuning the acceptance angle between $\pm 2^\circ$ and $\pm 22.5^\circ$. Due to the anisotropy of the photoemission from the valence band, changing the acceptance angle will affect the detected signal and hence can influence the timing. Therefore, the anisotropy of the valence band photoemission must be taken into account. An angle-resolved photoelectron spectroscopy study (ARPES) has revealed the energy dispersion of different contributions to the valence bands of HOPG [91].

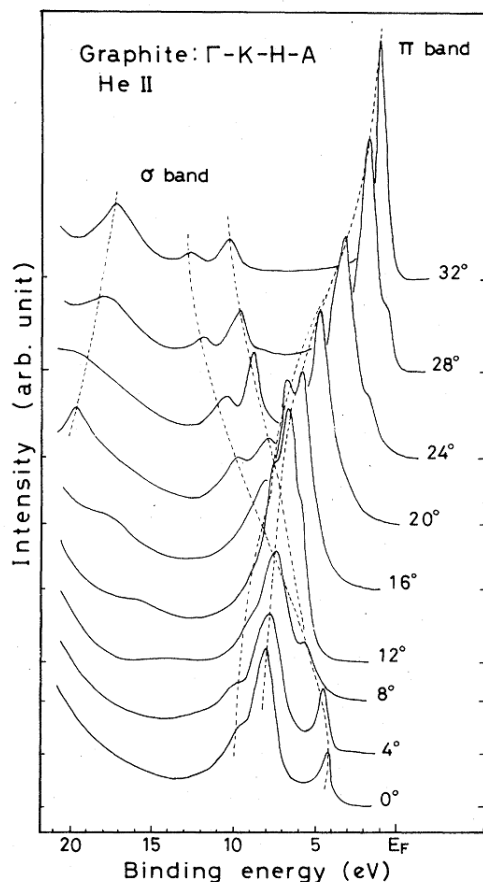


Figure 4.7: ARPES spectra (He II, 40.8 eV) acquired from HOPG in Γ KHA-plane with angles were measured with respect to the optical axis of HOPG [91].

The result is displayed in Fig. 4.7. Apparently, the spectrum measured by the TOF in default setting ($\pm 2^\circ$) will resemble an average of the curves recorded at 0° and 4° , while for increased angle will be the weighted average of all curves up to the

acceptance angle used in the experiment. Certainly, this conclusion can be only approximately correct, since the excitation energies in the streaking experiments are much higher than the He II excitation. Nevertheless, the discussion presented above will be of use in the next section to identify the spectral features observed in the streaking spectrograms and to interpret the retrieved results.

4.2 Valence band streaking spectroscopy

4.2.1 Streaking study at 112 eV XUV energy

In the preparation of the attosecond experiment, the commercial HOPG sample (MaTecK) was cleaved ex-situ with scotch tape, transferred into the ultra-high vacuum and annealed at 500 K for 60 minutes. The maximum reflectance of the XUV mirror used in this attosecond experiment was centered at the energy 112 eV with a bandwidth of 5 eV FWHM. The angle of incidence of the laser beam with the surface normal was 75° and the TOF spectrometer was aligned parallel to the surface normal.

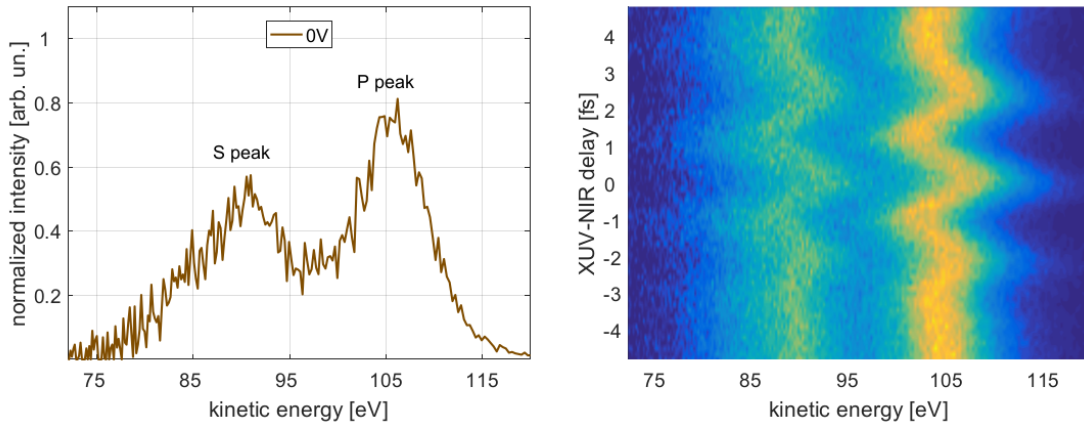


Figure 4.8: HOPG streaking (112 eV XUV energy). Streaking data on the valence band at 112 eV XUV excitation energy (5 eV FWHM). Left panel: NIR+XUV spectrum. right panel: Streaking spectrogram acquired with 150 as sampling interval and 25 s integration time.

The acceptance angle of the TOF spectrometer was set equal to $\pm 2^\circ$, such that predominantly electrons emitted along the surface normal, in Γ -A direction, are collected. Measurements with small acceptance angle are favorable from a theorist's point of view. Then, in good approximation, only one emission direction needs to be taken into account. In total 21 streaking scans have been recorded

and Fig. 4.8 shows a representative streaking spectrogram from this set, together with NIR-dressed XUV spectrum. The spectrum shows two partially resolved peak structures. In the light of the discussion of Sect. 4.1.3, the relevant spectral contributions to the two peaks could be identified. The peak at lower binding energy contains contributions from the bottom of the π -bands ($2p_z$), and from the maximum of the dispersing σ -band (mainly $2p_{xy}$). The peak at higher binding energy stems exclusively from the σ -band. On the bottom of this band, the $2s$ -contribution dominates. Throughout the rest of this chapter, the peaks at lower and higher kinetic energy will for brevity be addressed as S and P peak, respectively, as indicated in the left panel of Fig. 4.8. From the measured streaking spectrograms, the temporal information has been extracted by the retrieval procedure described in Ch. 2. For the HOPG project throughout, the photoemission timing will be discussed in terms of the P-S delay, which is defined as the difference between P peak delay and S peak delay. This convention implies that the P-S delay is counted positively if the emission from the P peak occurs later. For all streaking scans, the exposure time of the sample to the NIR between subsequent annealings did not exceed two hours, as justified in the next section reporting the 93 eV experiment. The intensity varied within $5 \times 10^7 - 6 \times 10^9 \text{ W/m}^2$. The data analysis will be presented in the following.

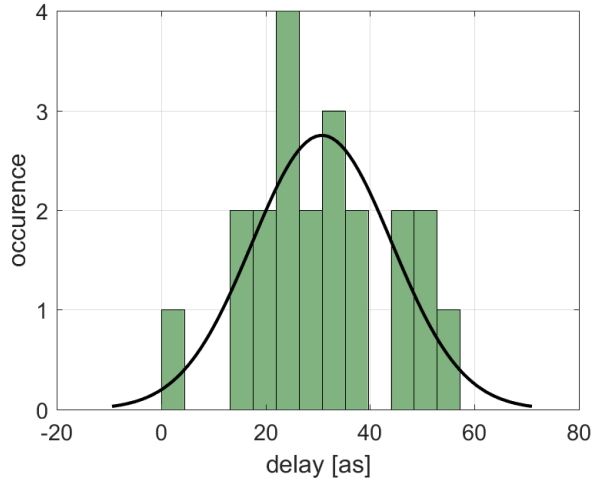


Figure 4.9: HOPG streaking (112 eV XUV energy). Photoemission P-S delay. Black curve shows the normal distribution fit which results in an average delay value of 31 ± 13 as.

All streaking spectrograms yield positive delay, i.e. the photoemission from the s region takes place first. The delay evaluation is shown in the histogram of

Fig. 4.9. The normal distribution fit of these data yields an average P-S delay value of 31 ± 13 as, where the error of 13 as is taken as the half width of the Gaussian distribution fit. This concept to define error bars is adopted in this thesis throughout. The photoemission delay is the key number in this HOPG experiment. Further insight into the temporal dynamics can be gained by an analysis of the chirp of the outgoing electron wave packets, i.e. of the time-dependence of the frequency of the detected photoemission signal.

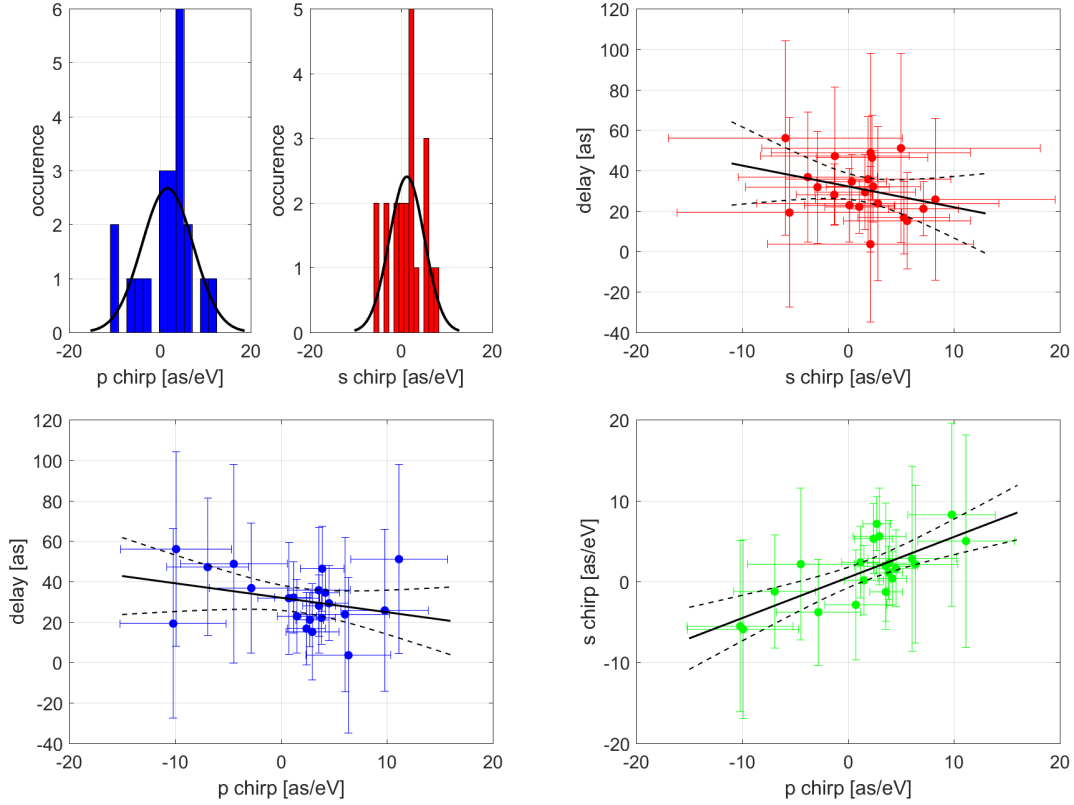


Figure 4.10: HOPG streaking (112 eV XUV energy). Chirp correlations results. Upper left panel: Statistical analysis of the chirp results for the P and S spectral features yield (2 ± 6) as/eV for the P and (1 ± 4) as/eV for the S peak. Upper right and lower two panels: Chirp-chirp and chirp-delay correlations. The black solid lines show the fitting result of the linear regression model. Dashed black lines show the 95%-confidence interval. This confidence interval is constructed such that it contains the true value of the slope with a probability of 95 %. This definition will be used to fit linear trends throughout this thesis.

The chirp signature can in principle provide information about the relative emis-

sion timing of different spectral portions of the signal within the S and P peak, respectively, which are not spectrally resolved due to the bandwidth of the XUV light. For example, a positive chirp means that the frequency of the detected signal increases with time, i.e. electrons with higher kinetic energy arrive later. The chirps of the electron wave packets were evaluated in the retrieval algorithm for both S and P peak by assigning a fit parameter for the chirp to both wave packets independently. This way, it has been taken into account that differences in the time evolution of electrons from different spectral regions will result in a difference of the retrieved chirps. The statistical analysis is shown in the upper left panel of Fig. 4.10. The mean chirps for the two peaks are equal within experimental accuracy, and very small.

The exciting XUV photon wave packet may as well exhibit an intrinsic chirp. The XUV chirp may be induced by a residual chirp of the NIR field upon HHG in the gas target, and by the reflection process from the multi-layer XUV mirror which singles out the isolated attosecond pulse from the HH radiation cut-off. This temporal structure of the XUV wavepacket will be encoded in the temporal signature of the photoexcited electron wave packet. The electron wave packet chirp contains entangled contributions from the temporal structure of the XUV pulse and from the photoemission process itself, which were not distinguishable within this project. In the chirp evaluation of the 112 eV graphite study, the correlations of the two chirp values with each other and the correlations of the chirps with the photoemission delay have been examined. These correlations are displayed in the upper right and the lower panels of Fig. 4.10. For each spectrogram, the chirps of the S and P peak are equal, within the limits of accuracy of the measurements. The trend lines representing the linear regression result suggest to the eye a dependence of the retrieved photoemission delay on the chirp values. However, on a 5%-significance level, there is no significant chirp-dependence of the delay in this study. The finite chirp-chirp correlation seen in the lower right panel of Fig. 4.10 reflects the fact, that the chirps of both the S and P features are almost identical for each recorded spectrogram.

4.2.2 Streaking study at 93 eV XUV energy

Further HOPG streaking measurements have been carried out at the attosecond XUV central energy of 93 eV with a bandwidth of 4.5 eV FWHM. There, the same geometry as in the 112 eV study has been adopted, with the TOF spectrometer aligned parallel to the surface normal of the sample. The electrostatic lens of the TOF spectrometer was operated at 200V. At this voltage, the acceptance angle is approximately $\pm 6^\circ$. A representative streaking spectrogram recorded at 93 eV is displayed in Fig. 4.11. Due to the higher acceptance angle, compared to

the 112 eV experiment, the peak at lower binding energy, the so-called P peak, contains more contributions from electrons with finite momentum components perpendicular to the surface normal, i.e. not only from the bottom of the $2p_z$ - π -band and maximum of the $2s2p_{xy}$ - σ -band, but from more extended regions of the bands. Seven streaking scans have been continuously recorded over a period of more than four hours.

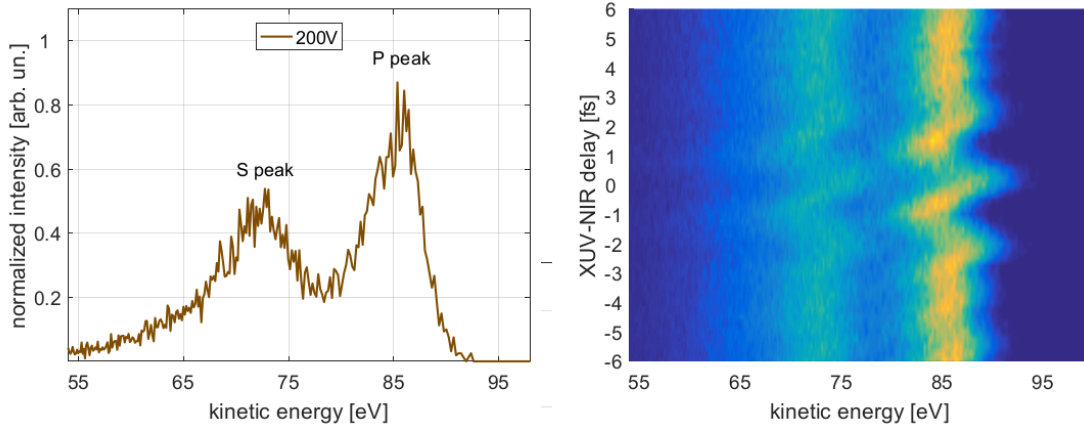


Figure 4.11: HOPG streaking (93 eV XUV energy). Streaking data on the valence band at 93 eV XUV excitation energy (4.5 eV FWHM). Left panel: NIR+XUV spectrum. right panel: Streaking spectrogram acquired with 150 as sampling interval and 18 s integration time.

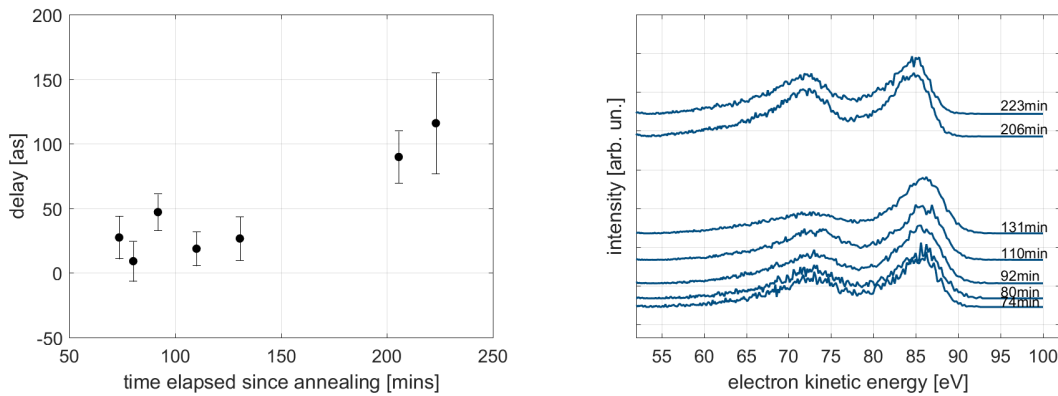


Figure 4.12: HOPG streaking (93 eV XUV energy). Left panel: P-S delay vs. time elapsed from sample preparation. Right panel: Valence band spectrum vs. time.

The sample was not annealed during the data acquisition. In this way, possible change of spectrum and/or retrieved photoemission delay over time were investigated. Both the delay and the valence band spectral shape show profound changes over time for $t \geq 120$ mins. In Fig. 4.12, valence band spectrum, and photoemission delay are displayed versus time. There is no significant change of the P-S delay with time for exposure times of less than 150 mins, but the two scans recorded after more than three and a half hours show a massively increased delay. The first five spectrograms yield an average P-S delay of about 30 as, while a delay around 100 as is retrieved for the last two streaking scans. Inspection of the valence band spectra displayed in the right panel of Fig. 4.12 shows that the first four spectra do not feature any change. But already the scan recorded after 130 mins exhibits a decrease of relative intensity of the S peak, and the last two spectra show a very strong increase in relative S peak intensity and a slight shift of the P peak to lower kinetic energy. The significant increase in delay and spectral shape might either be due to contamination of the surface or due to changes in the electronic structure due to the NIR femtosecond streaking field. As discussed earlier, bond formation and change in hybridization to sp^3 as reported in Ref. [101], are in principle not expected to occur for the present experimental parameters. Fig. 4.13 shows valence band photoemission spectra obtained at 130 eV photon energy to compare between clean HOPG and graphite oxide [109].

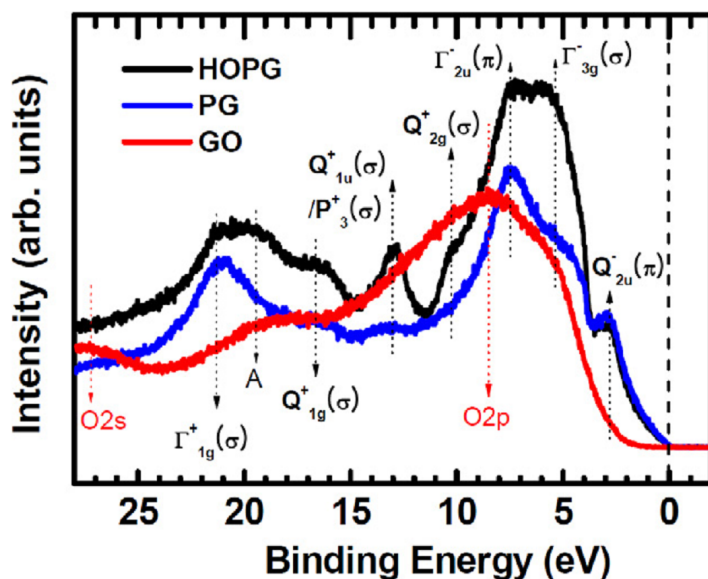


Figure 4.13: Valence band photoemission spectra from pristine graphite (PG), HOPG and graphite oxide (GO). Figure taken from Ref. [109].

With respect to the HOPG spectrum, the higher binding energy peak region at ≈ 20 eV is strongly suppressed. Notably, a further peak appears at ≈ 27 eV binding energy, which derives from the O2s level. A similar structural change might be indicated in the fifth spectrum of the present streaking experiment, but not in the last two spectra. The two last scans are disregarded in the statistics, due to contaminated and/or degraded surface. The analysis of the remaining spectrograms is elucidated below. Fig. 4.14 illustrates the statistical analysis for the P-S delay. Within error bars, the obtained average value of 26 as is equal to the 112 eV result of 31 as. Therefore, it is concluded that the P-S delay is positive in all HOPG streaking measurements conducted in this work.

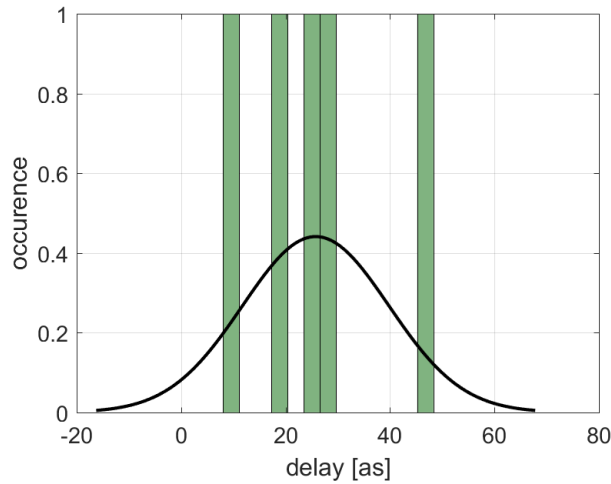


Figure 4.14: HOPG streaking (93 eV XUV energy). Photoemission P-S delay. Black curve shows the normal distribution fit which results in an average delay value of 26 ± 14 as.

The chirp evaluation result for the S and P peak feature is displayed in Fig. 4.15. The retrieved chirps for the two peaks are equal within experimental accuracy, the values are spread around 40 as/eV and the error is small. It is instructive to examine both the correlations of the two chirp values with each other and the correlations of the chirps with the P-S delay. The chirps of the two features are correlated, which is straightforward as those values are almost identical in each scan. This suggests that the temporal structure within the two spectral regions is not strongly different. Importantly, the chirps show no significant correlations with the P-S delay. The fact that in both the 93 eV and 112 eV study, the chirps of both regions are almost identical to each other, underlines the conjecture that there is no observable difference in the temporal structure of the photoemission

within each of the two sets of states. However, the averaged signal from the S peak photoemission is advanced in time with respect to the P peak emission, as found in both studies.

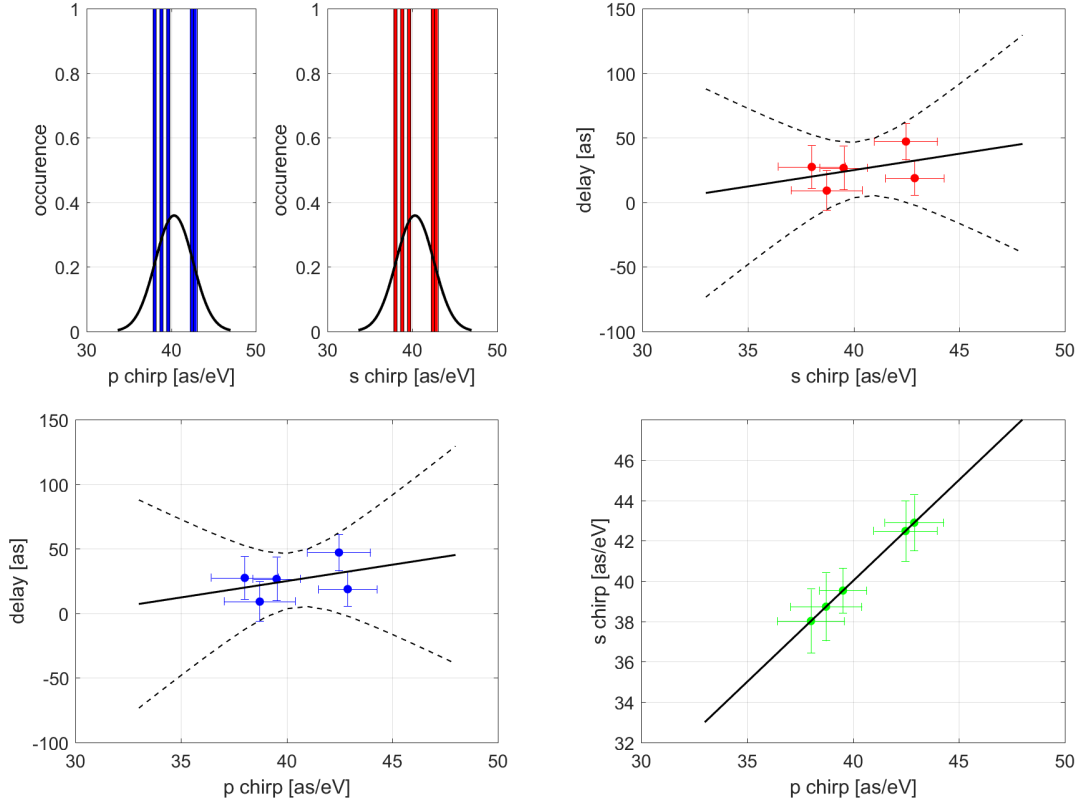


Figure 4.15: HOPG streaking (93 eV XUV energy). Chirp correlations results. Upper left panel: Statistical analysis of the chirp results for P and S peak yield the value of (40 ± 3) as/eV for both features. Upper right and lower two panels: Chirp-chirp and chirp-delay correlations. The black solid lines show the fitting result of the linear regression model. Dashed black lines show the 95%-confidence interval, see comment in the caption of Fig. 4.10.

4.3 Theory

Motivated by the experimental results presented in the previous section, a theoretical model has been proposed by Christoph Lemell [41], to describe and calculate the photoemission process from the HOPG valence band in the time domain. Within this effort, several possible contributions to the photoemission timing have been discussed within our cooperation. A detailed review of theoretical work on these different effects can be found in Ref. [36]. In the context of HOPG, electron transport, Coulomb-laser coupling (CLC), and Eisenbud-Wigner-Smith delay (EWS) were discussed. Due to the lack of efficient screening of the NIR field in the direction along the surface normal of HOPG, laser effects inside the material need to be considered. The different concepts will be presented one by one below, and the foundation and preliminary results of the theoretical work on HOPG will be presented and discussed thereafter.

Electron transport Emission time delays might be caused by propagation effects. The electron inelastic mean free path (IMFP) is known for HOPG to be 4-7 Å for kinetic energies around 100 eV [98].

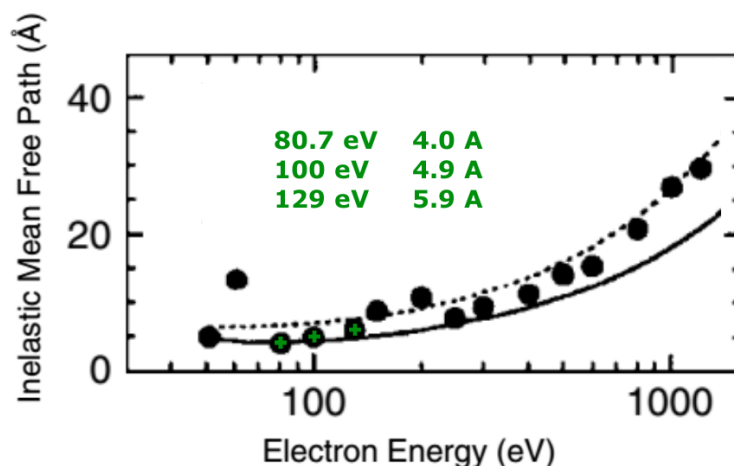


Figure 4.16: Inelastic mean free path (IMFP) of graphite. Solid black circles represent values determined from elastic-peak electron spectroscopy (EPES). Highlighted in green are those values which were obtained in the relevant energy range. IMFP values calculated from Penn algorithm by use of the energy-loss function of graphite are shown as solid line. IMFP results as calculated from the TPP-2M predictive equation proposed by Tanuma, Powell and Penn [110], are displayed in the dotted curve. Graph and caption modified from Ref. [98].

Experimental and theoretical data on the IMFP of HOPG are shown in Fig. 4.16 as a function of electron kinetic energy. In a free-electron picture, the average propagation time of an electron with kinetic energy E between excitation by the XUV pulse and photoemission into the vacuum can then be estimated as the quotient of the IMFP and the velocity $v = \sqrt{2E/m_e}$. Because the energy-dependence of the IMFP is negligible around 100 eV, this approach yields a delayed emission of the electrons which emerge from the levels at higher binding energy by about 5 as, i.e. a result with the sign opposite to the experimental results. In solids, the band structure leads to the modification of the electron velocity with respect to the free-electron case, and the resulting group velocity dispersion might lead to a significant effect on the photoemission timing. It is expected that crystal-structure effects should become less important for higher energies. For graphite, however, the influence could be larger than for other materials due to the stacking of 2D structures which results in free-electron motion only within the layers. DFT has been employed for ab initio calculations of the band structure of HOPG and the group velocity dispersion was derived [41]. The results for the group velocity are displayed in Fig. 4.17.

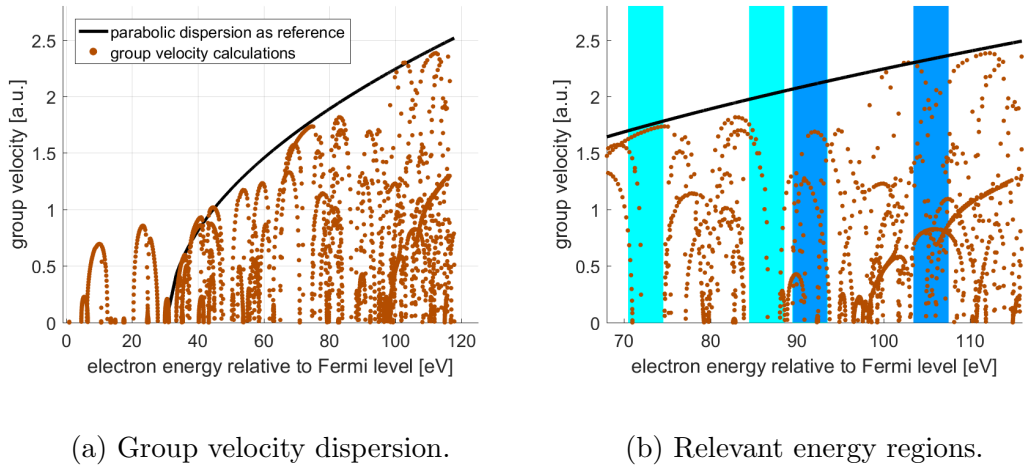


Figure 4.17: Electron group velocity in HOPG Γ -A direction calculated from ab initio band structure [41]. a) Group velocity results together with a parabolic dispersion curve as a guide to the eye and experimentally relevant regions shaded in grey. b) Shaded regions from left to right: S and P peak regions for 93 eV XUV energy (cyan) and S and P for 112 eV (blue).

From inspection of Fig. 4.17a), there is strong deviation of the dispersion from the free-electron parabola for energies ≈ 90 eV. As apparent from Fig. 4.13, the binding energies for the S and P peak maxima are located at 20.5 eV and 6.5

eV, respectively. Therefore, in Fig. 4.17b), as a guide for the eye, the location of the peak maxima are indicated by cyan shaded areas for 93 eV excitation energy and by blue areas for 112 eV excitation energy, respectively. By inspection of the graphs, it can then be expected that for 112 eV excitation energy, the averaged velocity for the S peak is lower than for the P peak. On the contrary, for 93 eV, the P peak photoelectrons are suggested to be significantly slower, on average, than the S peak electrons.

By comparison with the experimental data of this thesis, that suggests that group velocity dispersion can constructively contribute to forming of the delay in the 93 eV experiment, but would lead a contribution of opposite sign for the 112 eV scenario. The chirp analysis in the 93 eV and 112 eV data has found no significant difference between the chirps of S peak and P peak, respectively. Such difference is expected, however, if group velocity plays an important role, i.e. if electrons at slightly different energies are emitted at different times. Based on constant-initial-state spectroscopy on graphite, it has been suggested that band structure effects strongly influence the photoemission process only for final-state energies up to ≈ 90 eV, whereas for higher energies, the free-electron approximation is assumed to be valid [103]. For energies < 90 eV, the cross section for transitions from the σ and π initial states in the valence band to high-energy final states is governed by the joint density of states and the selection rule, while the transition cross sections are mainly determined by the atomic character of the initial states for energies > 90 eV.

Coulomb-laser coupling and Yukawa potentials In principle, a coupling of the laser field to the potential of the ion core after the photoexcitation of the electrons could result in a relevant contribution to the photoemission delay. However, the Coulomb-laser field is expected to be screened in the next layer and therefore, no strong effect is expected for HOPG. In addition to that, the electron gas within the same layer of the parent ion will screen the ion core quite efficiently. Coulomb-laser coupling (CLC) has been investigated in 1D, and ion potentials have been modeled by Coulomb and by Yukawa functions [41]. The resulting numerical streaking traces are displayed in Fig. 4.19, together with the data evaluation which was performed in the course of this thesis. In the evaluation, a negligible contribution of less than 1 as for Coulomb functions and a small contribution of ≈ 6 as for Yukawa functions with a sign opposite to the experiment was found. CLC is thus believed to be of minor importance in the forming of the observed delays.

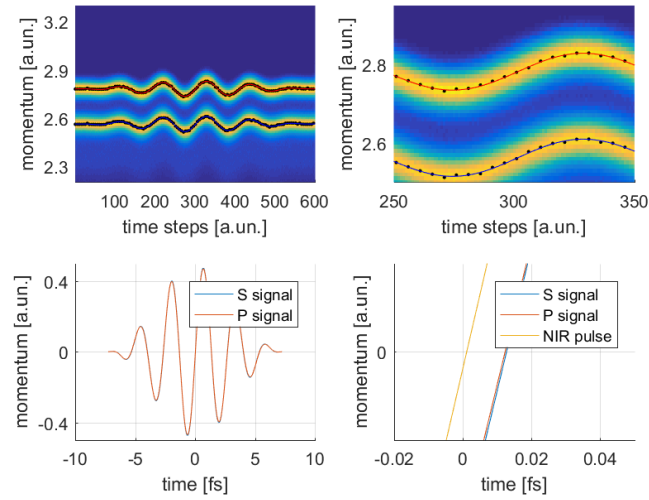


Figure 4.18: Numerical study on the influence of Coulomb-laser coupling (CLC) on HOPG streaking [41] with Coulomb ion potential. Delay analysis yields S delayed by 0.4 as.

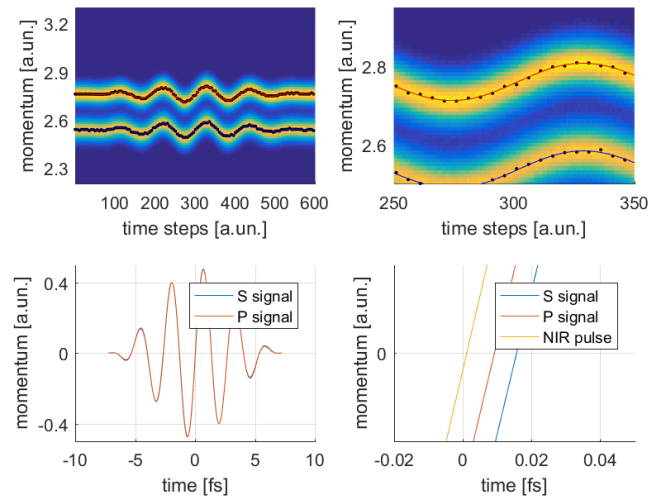


Figure 4.19: Numerical study on the influence of Coulomb-laser coupling (CLC) on HOPG streaking [41] with Yukawa ion potential. Delay analysis yields S delayed by 6.4 as.

Eisenbud-Wigner-Smith (EWS) delay Upon traversing the layers of HOPG, the photoexcited electron wave packet will acquire a shift of its phase Φ which translates into a time-shift $\delta\tau$ via $\delta\tau = 2\partial\Phi/\partial E$. The theoretical treatment of such induced time-shifts is well established. Eisenbud [111] and Wigner [112] have introduced a time delay as a quantum-dynamical observable for single-channel resonant scattering. This concept was later extended by Smith [113] to multi-channel contexts by introduction of a lifetime matrix. This time delay is called Eisenbud-Wigner-Smith (EWS) delay. Since photoemission is a half-scattering process, this concept can be applied [36]. In our context, this approach has been pursued by Lemell [41]. The EWS delay has been calculated as a function of the number of traversed layers and then scaled by the inelastic mean free path for HOPG. The EWS contribution from the parent atom can be neglected, as it turns out to be much smaller than the EWS-delay formed upon propagation. The calculation was performed in one dimension in the direction along the HOPG surface normal, and it was taken into account that there are two distinguishable axes in this direction: One axis, which has an atom in every layer, and one axis which has an atom in every second layer. For the latter, a velocity-independent delay of approximately 5-8 as is found, well below the relative delay observed in this thesis. For the former axis, the result is displayed in Fig. 4.20.

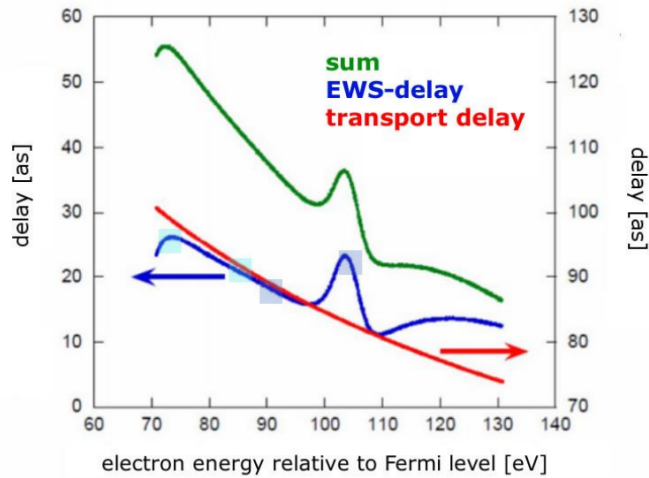


Figure 4.20: Calculation of absolute EWS-delays and transport-induced delays in HOPG as a function of electron kinetic energy [41]. The results for absolute EWS-delays and transport-induced delays in HOPG scaled by the IMFP as well as their sum are illustrated by lines. The experimentally relevant energies are indicated on the blue curve by shaded squares, from left to right: S peak and P peak for 93 eV XUV energy, and S and P peak for 112 eV excitation energy, respectively.

In Fig. 4.20, the transport delay, given as group velocity divided by IMFP of the electron, is shown in red. The EWS-delay scaled by IMFP is displayed in blue. The sum is drawn in green. As apparent from the blue curve, the EWS delay as formed upon traversing through the layers is generally monotonically increasing with electron energy, but exhibits a striking maximum around 105 eV. As seen from the cyan shaded squares in the blue curve, the EWS delay contribution is larger for S than for P peak electrons for 93 eV streaking, and hence suggests a time-ordering opposite to the experimental results. In contrast, for the 112 eV experiment, EWS yields indeed a small, but finite contribution which predicts S peak electrons to be emitted first by ≈ 10 as. In summary, the preliminary results of the calculation by C. Lemell suggest that CLC contributions to the delay are of minor importance and of opposite sign with respect to experimental result. Group velocity dispersion can account quantitatively for a delayed P emission in the 93 eV experiment, but predicts the wrong sign for 112 eV. EWS contributions give the wrong sign for 93 eV. However, for the 112 eV experiment, they support a delayed P emission. Further experiments with different photon energies and improved energy resolution are desirable to fully validate the theoretical approach.

4.4 Tungsten adsorbates on HOPG

The finite propagation time of the photoelectrons from the parent ion to the surface-vacuum interface, which depends on the speed of the electron and the inelastic mean free path can be different for electrons, which are launched from different initial states. Hence, the propagation can induce a relative photoemission delay between electrons from different levels. In 2D systems or small 2D clusters of the material of interest, the escape depth can be estimated by the monolayer thickness, if the contribution from back-scattering is negligible. Back-scattering involves trajectories where the photoelectron is reflected by the substrate layers before emission. In this limit, the propagation effect would be diminished and could thus be deconvoluted from the other influences by comparing the results from those 2D systems to the results of 3D samples of the same material. Attosecond spectroscopy experiments on tungsten crystals have provided a significant data basis [2, 3, 8, 9]. From these measurements, the photoemission timing between the W4f core state and the mostly 5d-derived valence band states is well-known in the three-dimensional case. Since measurements on tungsten in the gas phase are difficult to implement, last but not least due to the high gas densities needed for sufficient photoelectron flux, this thesis focussed on the preparation and characterization of 2D tungsten layers. HOPG has been suggested as a substrate before due to its well-defined surface structure [2]. Further, the contribution of back-scattering is expected to be minor for this system [114]. The HOPG sample was cleaved ex-

situ and then annealed in UHV in the preparation chamber of the low-temperature scanning tunneling microscope setup (LT-STM) which was described in Ch. 3. After annealing to 500 K for 60 minutes, the surface was checked by STM. Tungsten was then deposited from a tungsten ribbon of dimensions $10\text{mm}\times 1\text{mm}\times 0.025\text{mm}$ by resistive heating. Atom flux and adsorbate growth rate were monitored by a quartz micro-balance. By a water-cooling cycle, the evaporator was kept at a constant temperature to avoid excessive thermal drift of the crystal frequency. By STM, it was demonstrated that the tungsten adsorbates reproducibly form clusters of a few nm in diameter. Representative STM scans are shown in Fig. 4.21. STM topography of these clusters has been obtained and the electronic signatures of pure graphite and of tungsten have been obtained by scanning tunneling spectroscopy. The results are depicted in Fig. 4.22. The obtained average apparent height of around 2.5 nm is pretty close to the atomic diameter of tungsten and thus suggests that the clusters are truly two-dimensional.

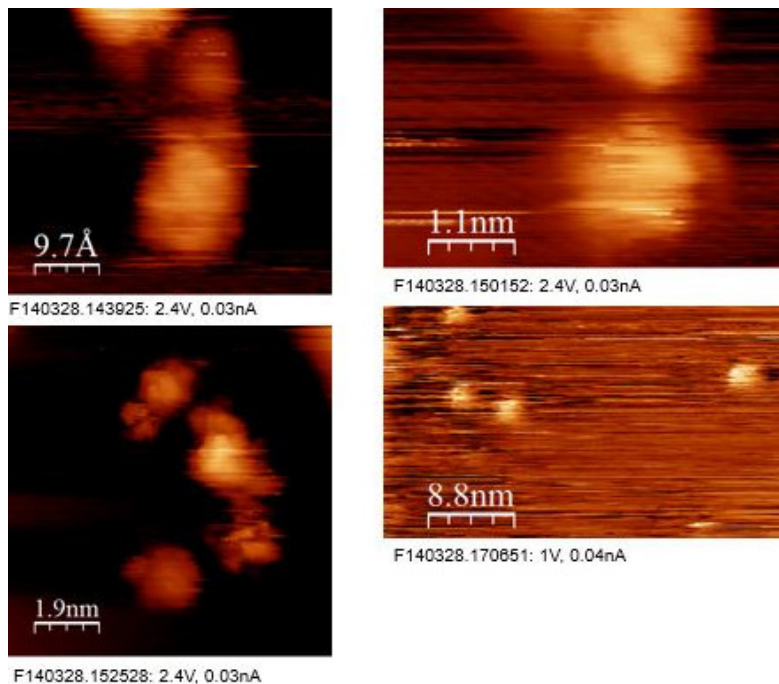
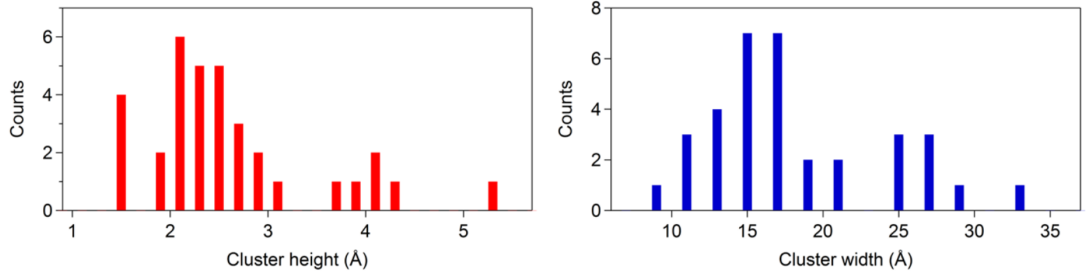


Figure 4.21: STM images of small tungsten clusters on HOPG.

STM topography



STS electronic signature

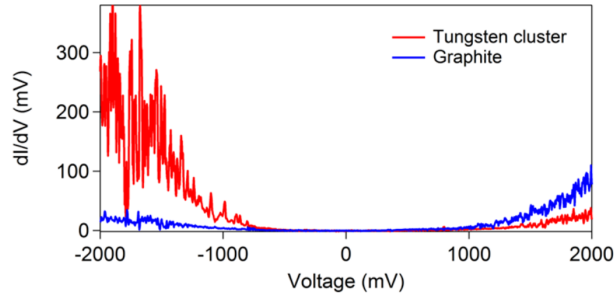


Figure 4.22: Statistical analysis of the tungsten cluster dimensions obtained by STS measurements. The upper left and right panels show the height and width statistics of the clusters (34 clusters measured). The clusters are two-dimensional (empirical atomic radius of tungsten is 1.4 Å), and their size varies between 10 and 100 atoms. The lower panel shows the differential conductance measurement of the tungsten cluster in comparison to clean HOPG.

4.5 Summary and outlook

In attosecond streaking measurements on HOPG, the photoemission timing from the valence band was investigated at XUV photon energies of 112 eV (5 eV FWHM) and 93 eV (4.5 eV FWHM). Excited by the used radiation, the photoelectron spectrum of the valence band exhibits two partially resolved peaks. From band structure calculations and ARPES, XPS and XES data, it could be inferred that mostly $C2p$ orbitals contribute to the peak structure at smaller binding energy and that the feature at larger binding energy is mostly formed by emission of $C2s$ electrons. The experimental results show a significant relative delay of the photoemission from the P peak with respect to the S peak emission of ≈ 30 as for both applied XUV energies. In parallel to this work, theoretical modeling has been tackled [41]. According to the model, at 93 eV excitation energy, the delay of the

P emission is suggested to be dominantly due to group velocity dispersion, whose influence is smaller at 112 eV. At 112 eV, however, the delay is indicated to be related to a relative maximum of the EWS-delay at the energies of the P spectral region. The quantitative agreement between experimental result and theoretical calculations is not satisfactorily so far, but the theoretical model provides promising arguments for the interpretation of the arising delays. We have demonstrated from an experimental point of view the existence of a relative photoemission delay between different spectral regions of the valence band of graphite and interpreted the results with the help of theoretical considerations [41]. The described HOPG project extends the attosecond streaking technique to the photoemission timing of valence shell electrons with different orbital character. It is recommended to perform further streaking studies on HOPG at different XUV photon energies to gain further understanding of the responsible mechanisms for the delay and to check the predictive power of the proposed theoretical model.

Chapter 5

Attosecond photoemission timing on magnesium

In this work, streaking spectroscopy was applied to Mg(0001) at XUV photon energies of 135 eV and 145 eV. This chapter first gives a brief review of prior experimental results and their theoretical interpretation, which formed the basis and motivation for these studies. It further reports the analysis of previous synchrotron data of the magnesium conduction band (CB), whose outcome proves essential in the interpretation of the obtained streaking data. Next, a 135 eV XUV stationary spectroscopy study is described. The remainder of the chapter is devoted to a detailed presentation of the streaking results. Here, the emphasis is on the obtained delays of the Mg2*p* core state photoemission signal relative to the CB signal and their dependence on both excitation energy and detection angle. Moreover, a characteristic dependence of the chirp of the outgoing electron wave packets on excitation energy and detection angle is demonstrated and discussed. In the light of these results, strong evidence for band structure influence on the photoemission timing in the measured energy range is obtained, and the experimental data are compared to the theoretical prediction.

5.1 Background and motivation

Previous attosecond streaking experiments on Mg(0001) films grown on W(110) have produced significant time-resolved information about the photoemission process in this material. For magnesium adlayers of 1-4 monolayers (ML), the delay of the photoemission signal from the Mg2*p* core level relative to the W 4f core level signal has been measured as a function of layer thickness [69]. Photoemission was induced by 118 eV XUV attosecond pulses. The obtained streaking results

suggest ballistic transport¹ of the photoelectrons through the ultra-thin film prior to their emission into the vacuum. In another study at the same excitation energy, thicker magnesium layers of 30 ML and more have been studied [2, 115], for which the influence of the tungsten substrate on the magnesium electronic band structure could be neglected. Here it has been demonstrated that photoelectrons excited from the magnesium $2p$ core level and those ejected from the magnesium conduction band are emitted into the vacuum almost simultaneously. This result could be reproduced and explained by different theoretical approaches [22, 26]. Specifically, in Ref. [26], the authors demonstrate a one-dimensional model which stresses the importance of the different nature of surface and bulk contributions to the CB photoemission signal.

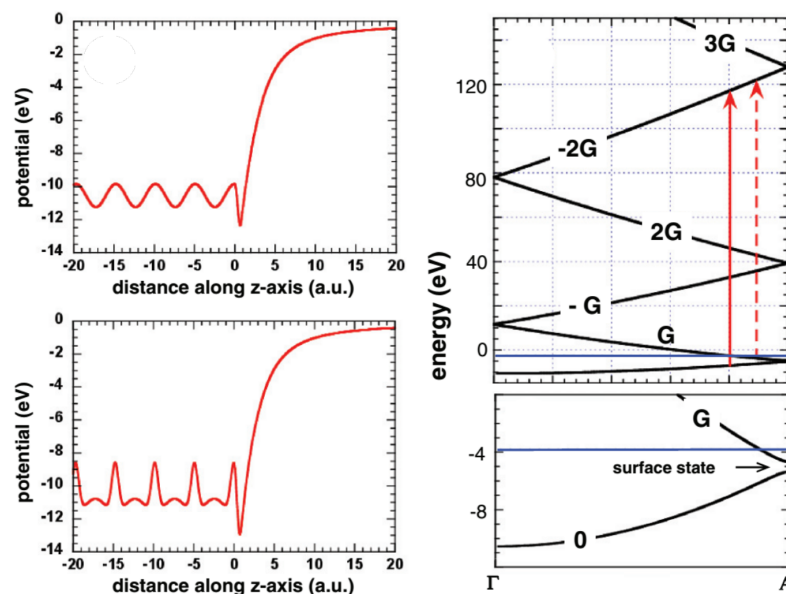


Figure 5.1: One-dimensional band structure calculations for free-electron-like metal. Left panels: Model potentials. Right upper panel: computed band structure (black), Fermi level (blue), vertical interband transitions (red). Right lower panel: Band gap and surface state. Figure adapted and modified from Ref. [26].

The nature of these contributions can be understood as follows. At the surface, a conduction band electron can be photoemitted via direct coupling of the electronic initial state to a continuum state. On the contrary, photoexcitation of a CB electron deeper inside the bulk first requires an interband transition from an initial

¹Propagation is ballistic on length scales smaller than the inelastic mean free path, i.e. in the absence of scattering on these scales.

state $E_i(\vec{k}_i)$ to a final state of energy $E_f(\vec{k}_f)$. This transition obeys energy and momentum conservation, thus $E_i(\vec{k}) + \Omega_X = E_f(\vec{k}_f)$, where Ω_X is the XUV photon energy, and $\vec{k}_i + \vec{G} = \vec{k}_f$, where \vec{G} is a reciprocal lattice vector². In Ref. [26], the authors state a strong dependence of the photoelectron intensity from this bulk contribution on the XUV photon energy and link it to a strong photon energy dependence of the relative delay between the photoemission signals from $2p$ core level and CB, respectively. The sketch of the calculated band structure shown in the upper right panel of Fig. 5.1 helps to elucidate this concept. For further details on the band structure of magnesium, see e.g. Ref. [116]. The photoexcitation probability for electrons deeper inside the bulk, and hence the photoemission signal from such electrons, will only be high if vertical interband transitions exist for the XUV pump photon energy.

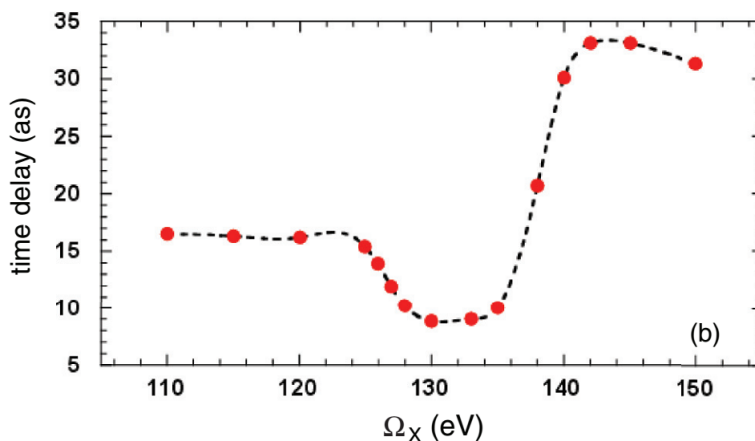


Figure 5.2: Photoemission time delay for electrons emitted from the core state relative to the electrons emitted from the conduction band as calculated for a one-dimensional array of atoms described by the pseudo-potentials shown in Fig. 5.1 as a function of the XUV excitation energy Ω_X [26].

The CB photoemission time averaged over the whole width of the band³, strongly correlates with the strength of the contribution from bulk electrons to the signal. Streaking accesses the relative photoemission delay between Mg $2p$ core level signal and CB signal. The authors of Ref. [26] calculated this delay as a function of XUV photon energy Ω_X in the range of 90 - 140 eV, which is experimentally accessible. The emission time of electrons excited from the Mg $2p$ core level was simply defined as the quotient of the inelastic mean free path by free-electron velocity. As shown

²The photon momentum is negligible in the XUV spectral range.

³Note that the XUV bandwidth (4-5 eV) is similar to the width of the conduction band.

in Fig. 5.2, they find the emission of $2p$ photoelectrons to be generally retarded with respect to the emission of CB electrons, in the entire photon energy range. The value obtained for excitation energies around 120 eV is 17 as in fair agreement with the small experimental value of 5 ± 20 as which was reported in Ref. [115] for 118 eV. The model also predicts a local minimum of the delay for energies around 130 eV and a substantial increase of its value for energies exceeding 140 eV. The minimum is explained by efficient vertical interband transitions at these energies, which increase the contribution of bulk electrons to the photoemission intensity and thus reduce the overall time advance of the conduction band electrons. Based on these considerations, streaking measurements on magnesium at XUV pump photon energies around 130 eV and well above are expected to provide an important test of the theory presented in Ref. [26].

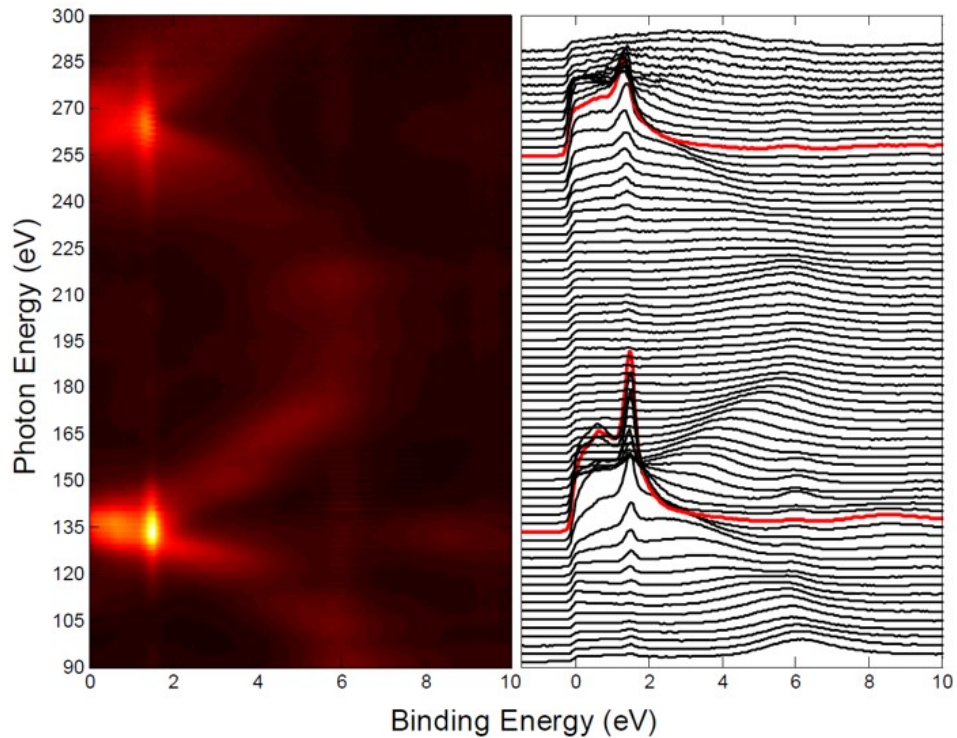


Figure 5.3: Mg(0001) CB synchrotron data as a function of XUV energy. Resonant enhancement of the photoelectron signal at ≈ 135 eV and ≈ 270 eV. Red lines in the right panel of the figure indicate maximum yield as a guide to the eye. Normal emission geometry (acceptance angle $\pm 3^\circ$). Figure provided by S. Neppl [42].

Streaking studies on magnesium in this XUV range are further motivated on the basis of synchrotron photoemission data from Mg(0001) which have been acquired

for a finely sampled energy window in the XUV range [42]. The photoemission yield from the CB region is shown in Fig. 5.3 as a function of the excitation energy at the Γ -point of the surface reciprocal space, i.e. for electrons detected in normal emission geometry (acceptance angle $\pm 3^\circ$). The sharp feature visible below 2 eV binding energy on the right panel of Fig. 5.3 corresponds to the Shockley surface state [117–119]. Its binding energy is independent of the excitation energy, as expected for a two-dimensional system with dispersion in the plane perpendicular to the surface normal [120], but the intensity of the photoemission signal shows a strong dependence on the excitation energy. The surface state peak resides on the photoemission signal from the conduction band states which extends from 0-5 eV. The latter shows a strong dependence on the XUV photon energy, and also the parabolic dispersion of the bands is clearly apparent in both the left and right panels. The intensities of both the surface state signal and the bulk states signal exhibit pronounced maxima at around 135 eV and 270 eV photon energy. This behavior repeats periodically at higher energies since a variation of the photon energy at a fixed normal emission geometry corresponds to a change of the perpendicular component of the electron wave vector. A similar effect has been reported in an experiment on aluminum [121].

To quantify the energy dependence observed in Ref. [42], analysis of the synchrotron data has been performed in the course of this thesis which is detailed in the next section of this chapter. From the left panel in Fig. 5.3, by a look at the parabolic dispersion curves, the projected band gap is clearly visible, and for XUV excitation energies near 130 eV and 270 eV, electrons can be efficiently excited from initial states with momenta close to the edge of the one-dimensional Brillouin zone in the direction perpendicular to the surface. Importantly, near to the zone boundary, the final bands exhibit very low dispersion. The effective mass of the electron in a given state in the final band is proportional to the inverse curvature of the band at this state [122] and hence is enhanced for a flat region of the band. This suggests that electrons excited inside the bulk by XUV photon photons with energies near these values travel to the surface at a reduced group velocity. From this argument, the photoemission time is expected to be higher for conduction band electrons excited in the bulk by XUV frequencies close to 135 eV or 270 eV, with respect to those excited by frequencies far from these values. Streaking spectroscopy enables to follow the electron dynamics in real time and is suitable to check for traces in the time domain of such band structure influence. In this thesis, streaking measurements have therefore been performed on Mg(0001) at 135 eV and 145 eV to allow for comparison between the temporal characteristics of the photoemission process within and 10 eV beyond the resonance. The results of these experiments will be presented and discussed later in this chapter.

5.2 Conduction band synchrotron data

The magnesium conduction band has a spectral width of about 5 eV. The photoemission of electrons which are photoexcited via different transitions and from different initial states can in principle show different temporal characteristics. Specifically, as discussed before, the interplay between emission from deeper inside the bulk via vertical interband transitions and direct emission from the surface is suggested to play a major role in the photoemission timing [26]. For an understanding of the results obtained in the magnesium streaking studies performed in this work, it is mandatory to know the relevant transitions which contribute to the conduction band photoemission as precisely as possible. This section is devoted to our analysis of the synchrotron data of Ref. [42].

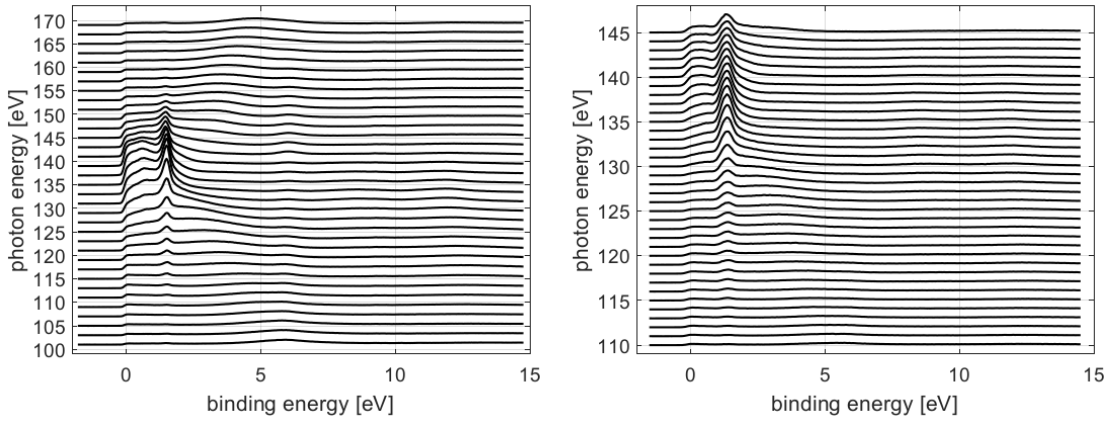


Figure 5.4: Synchrotron data of the Mg(0001) conduction band at varying photon energy. Left/right panel shows data acquired with acceptance angle of $\pm 3^\circ/\pm 0.3^\circ$, respectively.

Synchrotron data from the magnesium conduction band have been acquired at normal emission geometry and for emission angles up to $\pm 6^\circ$ against the surface normal. At normal emission, the XUV photon energy was varied in steps of 1 eV. To obtain the angular dependence of the signal for small angles around the surface normal, the detection angle has been varied in steps of 1-2° at fixed photon energy. The emphasis in this section is on the extraction of the parabolic relationship between detection angle and surface state binding energy, and the relative weight of the surface state in the total conduction band photoemission signal, as well as on the photon energy dependence of the bulk emission signal.

5.2.1 General evaluation

In normal emission geometry, data have been taken for two different values of the acceptance angle of the analyzer, $\pm 0.3^\circ$ and $\pm 3^\circ$. The data are displayed for a selected binding energy range in Fig. 5.4. For the smaller acceptance angle, the detected photoemission signal is generally much smaller. To still obtain meaningful statistics, the pass energy of the analyzer has been increased, at the expense of a decrease in energy resolution. This, in turn, is the reason for the apparently broader features in the data recorded at $\pm 0.3^\circ$ with respect to the $\pm 3^\circ$ data.

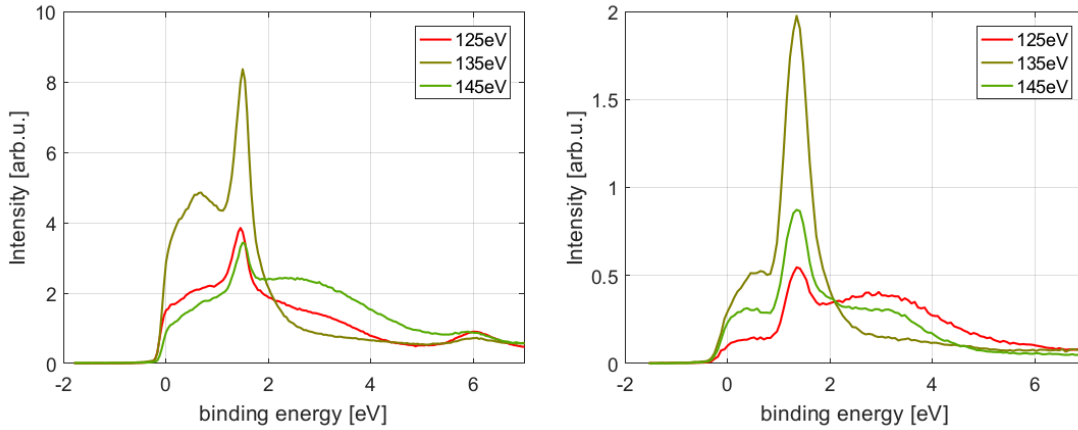


Figure 5.5: Photoemission energy distribution curves for the Mg(0001) conduction band for three distinct photon energies. Left/right panel shows data acquired with acceptance angle of $\pm 3^\circ/\pm 0.3^\circ$, respectively.

To get further insight into the strong dependence of the photoemission spectrum on the photon energy, it is instructive to zoom in and take a glance at Fig. 5.5, which shows the data for 125 eV, 135 eV and 145 eV. The intensity of the surface state varies strongly with the photon energy. The surface state peak appears broader in the curves of the right panel of Fig. 5.5 due to the increased pass energy in the $\pm 0.3^\circ$ data. As mentioned before, the surface state signal resides on the broad photoelectron intensity derived from conduction band states emission. These contributions show strong photon energy dependence in shape and strength. In particular, for 135 eV a very pronounced structure emerges on the low-energy side of the surface peak, which is considerably weaker for 125 eV and 145 eV. On the other hand, the photoelectron yield on the high-energy side is almost absent for 135 eV, while it is rather strong for 125 eV and 145 eV. This is an interesting finding. One might argue that the computation in Ref. [26] is indeed correct, and that the structure which develops at 135 eV originates from electrons excited deep

into the bulk via vertical interband transition. Under these premises, one could expect that this low-binding energy portion of the conduction band signal reaches the detector as the latest because the electrons first need to propagate through the bulk before they are emitted into the vacuum. This conjecture will be pursued further later in this chapter.

5.2.2 Surface state emission characteristics

From Fig. 5.3, Fig. 5.4 and Fig. 5.5, it is apparent that the surface state signal intensity depends strongly on the XUV excitation energy. For the interpretation of the photoemission timing experiments performed in the course of this thesis, it is important to quantify this dependence.

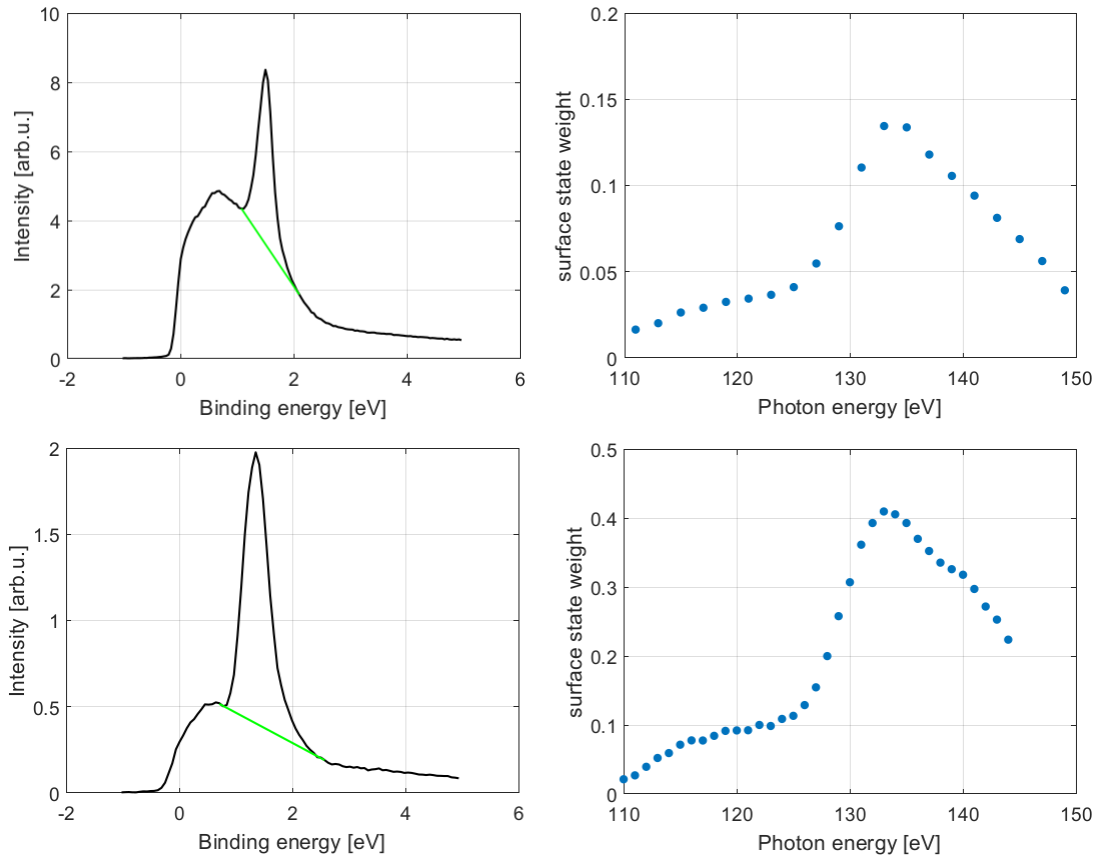


Figure 5.6: Calculation of the surface state relative weight. Disentanglement of the surface contribution and relative weight vs. photon energy is depicted for acceptance angle $\pm 3.0^\circ$ ($\pm 0.3^\circ$) in the upper (lower) panels of the figure.

Therefore, the relative weight of the surface state in the full conduction band photoemission spectrum has been determined as a function of XUV energy. The results are shown in Fig. 5.6. The surface state signal was extracted by defining the background via a straight line, as shown in green color in the left panels of Fig. 5.6. The relative weight of the surface state in the spectrum is then obtained by dividing the full conduction band signal intensity by the intensity of the deconvolved surface feature. The results for the relative weight of the surface state emission is shown as a function of photon energy in the right panels of Fig. 5.6. For both values of the acceptance angle, the relative weight of the surface state exhibits a strong maximum at 132 eV. However, while for the small acceptance window, the weight can be up to more than 40%, it does not exceed 15% for the larger window. It can then be inferred that the surface state emission is limited to a small solid angle around the surface normal. This result will be relevant for the discussion of the photoemission timing later in this chapter. In particular, since the maximum angular resolution of the TOF spectrometer used for the streaking experiments throughout this thesis is $\pm 2^\circ$, the influence of the surface state emission on the photoemission timing of the total conduction band signal will only be moderate or small.

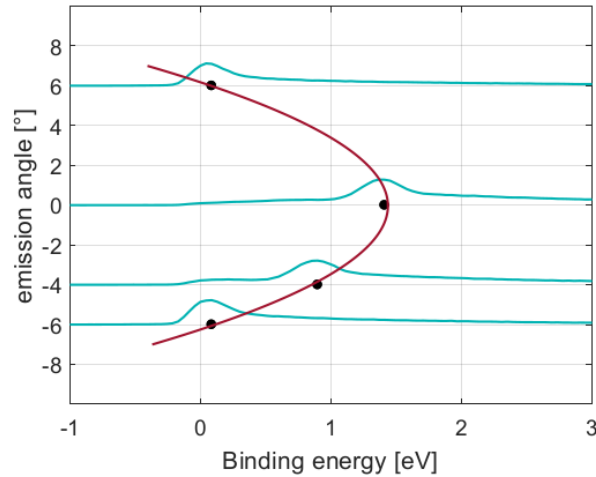


Figure 5.7: Parallel dispersion of the surface state. Spectra measured at 130 eV photon energy for various detection angles. Acceptance angle $\pm 0.3^\circ$.

Photoemission data have been acquired within the same synchrotron experiment for varied detection angle at the fixed photon energy 130 eV. In these measurements, the acceptance angle was set to $\pm 0.3^\circ$, and the detection angle was varied in the range $\pm 6^\circ$ against the surface normal. Evaluation of these data is beneficial, in particular, for the extraction of the dispersion relation for the surface state as

a function of the wave vector component parallel to the surface plane. The fitting result of the quadratic regression model applied to the data is shown in Fig. 5.7. The emission angle θ can be related to the parallel component of the electron wave vector k_{\parallel} via $k_{\parallel} = \sqrt{2mE/\hbar^2} \times \sin(\theta)$, where E is the kinetic energy of the detected electron and m is the free electron mass. Via this relationship, the electron effective mass was calculated to be $1.04 m_e$, a value which is in good agreement with the literature [123, 124], where the value was obtained from the evaluation of angle-resolved photoemission spectroscopy (ARPES). From the fitted parabolic dispersion, it is seen that the surface state emits only in a solid angle cone of $\pm 6^\circ$ around the surface normal. The spectral shape of the bulk contribution was also investigated but did not show noticeable dependence on the angle.

5.3 Conduction band XUV spectroscopy

As discussed above, the photoemission signal from the magnesium conduction band exhibits a significant emission angle dependence mainly originating from surface state dispersion. It is not a priori clear if such angular dependence is manifested on the attosecond timescale. In this section, results obtained in this work from stationary photoemission spectroscopy on magnesium with 135 eV attosecond pulses are presented, which show a strong angular dependence of the conduction band photoemission intensity.

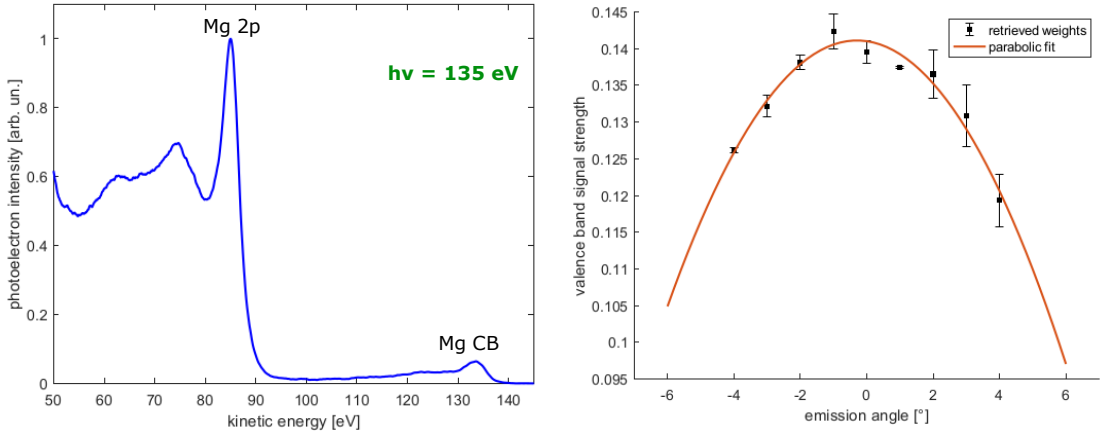


Figure 5.8: Stationary XUV (135 eV) spectroscopy of Mg(0001). Left panel: Representative magnesium spectrum. Right panel: Normalized conduction band signal intensity as a function of the detection angle (black). The parabolic fitting result is shown in red. 0° corresponds to normal emission geometry (acceptance angle $\pm 2^\circ$).

The sample has been aligned with the surface normal parallel to the spectrometer axis as accurately as possible by eye. In this orientation, a stationary XUV photoemission spectrum has been acquired. The sample was then rotated to change the detection angle in steps of 1° in both directions in a range of $\pm 4^\circ$. The acceptance angle of the TOF spectrometer was $\pm 2^\circ$. For each angle, at least two spectra have been recorded. A representative spectrum is shown in the left panel of Fig. 5.8. The spectra have been normalized to the intensity maximum of the respective $2p$ core level emission peak, and the energy axis in each spectrum has been calibrated using the binding energy of the $2p$ peak which equals to 49.6 eV for clean Mg(0001) systems [125]. The so normalized integrated intensity of the conduction band spectrum shows a parabolic dependence on the detection angle, which is shown in the right panel of Fig. 5.8. The value of the angle associated with the maximum of the parabola is identified with the normal emission geometry (0°) and then used for the accurate sample alignment in the streaking experiments to be shown and discussed later in this chapter.

5.4 Magnesium attosecond streaking

Motivated by the experimental and theoretical background described in the first section of this chapter, in this work attosecond streaking measurements have been conducted on magnesium. As discussed in the previous sections, the conduction band photoelectron yield exhibits a strong local maximum at around 132 eV. Therefore, streaking has been applied to thick Mg(0001) films on W(110) with the XUV pump photon energies 135 eV and 145 eV to measure the temporal characteristics of the photoemission both in and off the "resonant" regime. In this section, the experimental procedures and the results of these streaking measurements are presented in detail. The discussion and interpretation of the results constitute the core of the later sections of this chapter.

5.4.1 Sample preparation and characterization

Magnesium films have been deposited on tungsten in situ by epitaxial growth. The thickness of these film was 30-100 ML, i.e. thick enough so that the properties can be assumed to be bulk-like [118, 123]. Prior to the magnesium deposition, the W(110) single crystal has been thoroughly cleaned. This was accomplished by a combination of repeated sputtering and annealing cycles. The crystal was first sputtered for at least 45 mins using argon ions which are accelerated by a voltage of 1.1 kV. The sputter current was 20-30 μA . Thereafter, the tungsten sample was heated by electron bombardment and kept at a temperature of around 2400 K for 5-7 s to desorb residual contamination such as oxygen atoms. Carbon

contamination cannot be removed this way. Therefore, the crystal was exposed to molecular oxygen at a pressure of 1×10^{-6} mbar. Upon dissociation of O_2 , O atoms then bind to residual carbon atoms. After about 10 s the O_2 gas was pumped out, and the sample was flashed in UHV again to remove the carbon in form of mostly carbon dioxide. This procedure was usually repeated ten times.

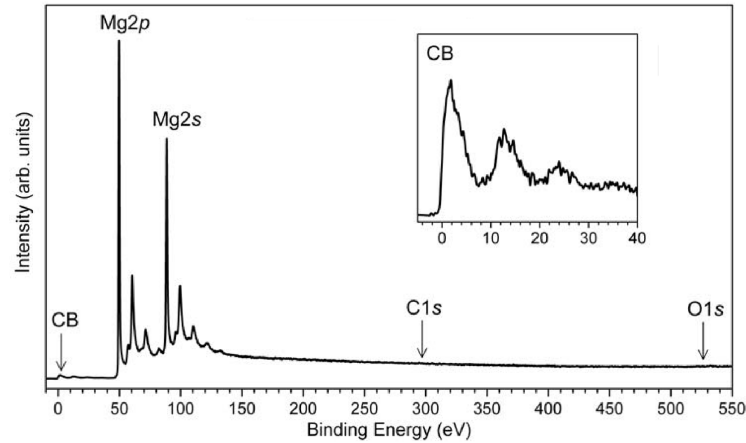


Figure 5.9: Photoemission spectrum of Mg(0001) evaporated on W(110), excited by 700 eV synchrotron radiation. Picture taken and modified from [2].

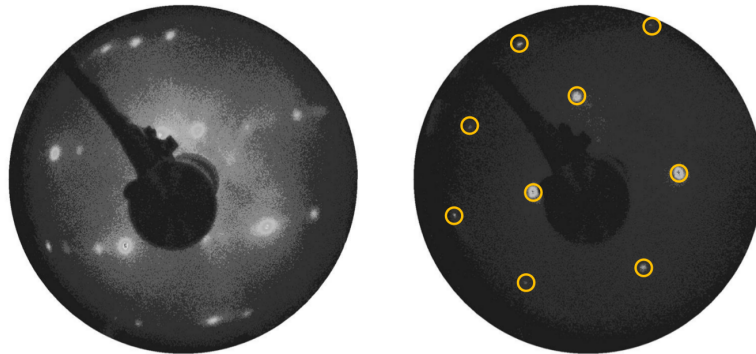


Figure 5.10: Mg(0001) films evaporated on W(110), recorded by LEED at 160 V electron energy. Left panel: If the magnesium film is too thin, the LEED pattern exhibits a superstructure formed by the film and the tungsten substrate. Right panel: A sufficiently thick, well-ordered film shows the characteristic hexagonal pattern corresponding to (1×1) -periodicity, highlighted by orange circles.

After cooling down to room temperature, the tungsten surface prepared in this way was exposed to magnesium vapor from a Knudsen cell evaporator for 2-3 mins. This evaporator consists of a crucible filled with magnesium grains which are heated resistively to 400 °C. This deposition method results in films as thick as 30-100 ML. After magnesium deposition, the sample is annealed for 2-3 mins at 150 °C to improve the quality of the long-range order. The cleanliness of both the freshly prepared tungsten surface and the adsorbed magnesium films have been checked by X-ray photoemission spectroscopy (XPS). The orientation and order of the Mg(0001) film were checked by low-energy electron diffraction (LEED). LEED can also serve as a check for the sufficient thickness of the film. At least 30 ML of magnesium are required to obtain a film with the characteristics of the Mg(0001) bulk lattice such as the sharp hexagonal LEED pattern [123]. If the film is not thick enough, the LEED picture would show a superstructure. Examples of representative LEED patterns are illustrated on the right side of Fig. 5.10, and a representative X-ray photoemission spectrum is shown on the left. In the upper right panel, the LEED picture of a thin film is displayed, which exhibits a rather blurry superstructure. On the contrary, the lower panel shows the sharp hexagonal pattern of a thick magnesium film with appropriate thickness for the present study.

5.4.2 Streaking measurement details

For the magnesium streaking measurements carried out in this work, a near-infrared streaking field has been employed with 4-5 fs laser pulse duration and 1.6 eV photon central energy. The NIR pulses were produced by the laser setup FP3 discussed in the second chapter. Two different XUV mirrors have been used, of which one reflects attosecond pulses with 135 eV central photon energy (FWHM: 3 eV) and the other pulses with 145 eV (FWHM: 3 eV). The geometry of the streaking experiments was chosen such that the laser beams impinge on the magnesium surface at a glancing angle of $75^\circ - 79^\circ$ measured relative to the surface normal, and with the polarization parallel to the plane spanned by incident beam and surface normal. The TOF spectrometer was aligned such that its axis was parallel to the surface normal. In this way, electrons emitted in normal emission are mainly detected. The accurate sample alignment was ensured by the XUV spectroscopy method described in Sec. 5.3. As discussed earlier in this chapter, the photoelectron yield from the conduction band at 135 eV is pronounced at normal emission and the surface state disperses strongly with the angle. The theoretical calculation of the photoemission timing in Ref. [26] is based on a one-dimensional model and hence describes only electrons emitted parallel to the surface normal [26]. A difference in the photoemission timing characteristics is expected to show up between the cases of photoelectron detection mainly in normal emission direction

and of detection from larger angles as well, respectively. In fact, for narrow as well as broad acceptance angles, the contribution from the surface state is minor as discussed earlier in this chapter with the help of the synchrotron data analysis. The surface state contribution in the narrow-angle streaking measurements is less than 10-15%, and even smaller for the broad angle geometry. Therefore, the main contribution to the photoemission signal stems from bulk electrons. For these, however, as discussed before, the two scenarios of resonant bulk emission and direct surface emission must be distinguished. Here, it was assumed that the resonant bulk emission signal is pronounced in normal emission, and its weight decreases with increasing emission angle. Therefore, the absolute photoemission delay of the CB electrons is supposed to be smaller for larger detecting angle. To check this assertion, angle-resolved streaking measurements are indicated. Here, however, due to experimental constraints, a different strategy has been put forward. A significant number of streaking spectrograms has been recorded in normal emission geometry for narrow ($\pm 2^\circ$) and wide (up to $\pm 20^\circ$) acceptance angles of the TOF spectrometer. For the wide acceptance angle situation, where the contribution from the vertically emitted electrons to the full detected signal is much smaller, the retrieved CB delay is considerably smaller than for narrow acceptance angle. As described in the second chapter, $\pm 2^\circ$ is the default acceptance angle of the spectrometer, which can be enlarged to up to $\pm 20^\circ$ via application of the electrostatic lens. These two sets of data, one each for narrow and wide detection angle, have been acquired for both 135 eV and 145 eV XUV photon energy.

5.4.3 Streaking results at 135eV excitation energy

Detection in narrow acceptance angle

To obtain temporal information about the photoelectron signal emitted from the Mg(0001) film mainly in normal emission direction, a set of 29 streaking spectrograms was collected with the TOF spectrometer aligned parallel to the surface normal with the TOF spectrometer acceptance angle set to $\pm 2^\circ$, i.e. the electrostatic lens was set to 0 V. A representative streaking spectrogram is shown in Fig. 5.11. The laser setup FP3 was used for all magnesium measurements which produced 4-5 fs NIR laser pulses at a repetition rate of 4 kHz. To block the intense NIR laser beam ($10^8 - 10^9$ W/cm²) from the XUV mirror in the double-mirror assembly, filters of 200 nm Pd and Zr have been used in the pellicle filter setup. These filters additionally act as a high-pass filter for the high harmonics in the XUV spectrum. For the evaluation of the streaking data, the method described in Ch. 3 was used. The relative photoemission time delay of the conduction band electrons was retrieved from the data with respect to the Mg2*p* core-level electrons.

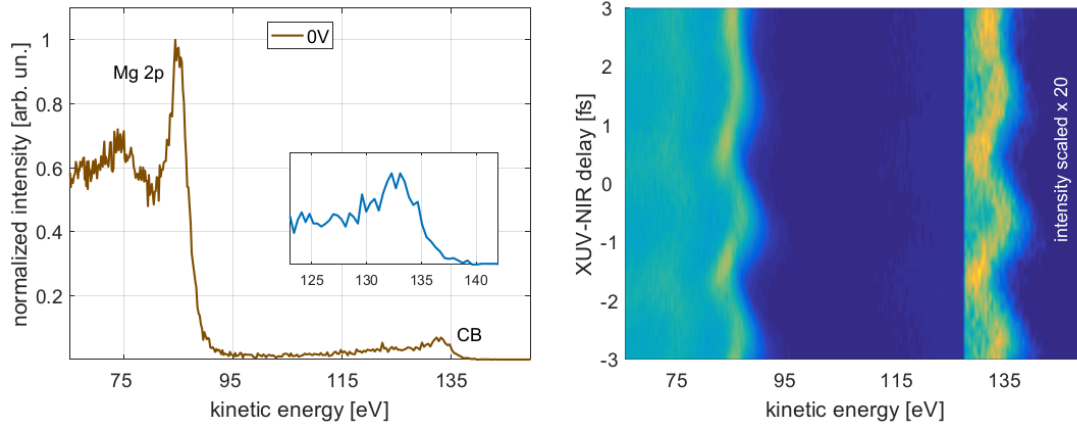


Figure 5.11: Mg(0001). (135 eV). Left panel: Stationary XUV+NIR spectrum. Mg2*p* core state signal at 85 eV and first-order plasmon loss at 75 eV. The CB signal intensity was scaled for clarity. The 0V legend entry refers to the default setting of the TOF spectrometer with a detection angle of $\pm 2^\circ$. Right panel: Streaking spectrogram.

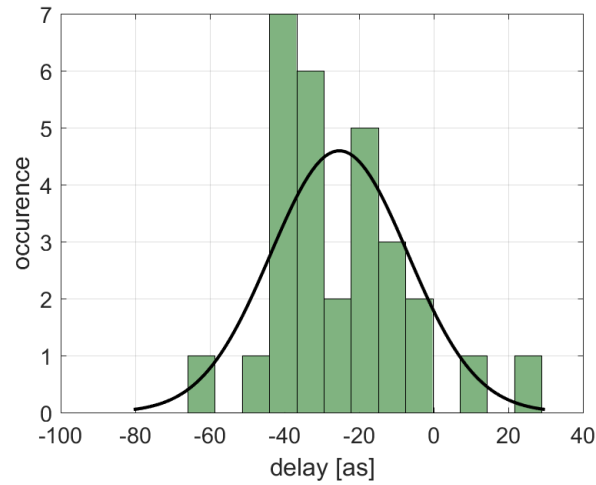


Figure 5.12: Mg(0001). (135 eV). Detection angle $\pm 2^\circ$. CB photoemission delay relative to the 2*p* signal. Black curve shows the normal distribution fit which results in an average delay value of -25 ± 18 as.

By the here adopted convention, a negative delay implies that the conduction

band electrons are emitted earlier⁴. The results obtained by the delay retrieval procedure are presented in Fig. 5.12 below in the form of a histogram summarizing the statistical analysis. As shown in Fig. 5.12, the photoemission of the $2p$ core state electrons is delayed on average by 25 ± 18 as, which is clearly non-zero. This seems to be at odds with the results reported in Refs. [2, 115]. Here, the authors found minor delay of the core state emission (5 ± 20 as) in streaking measurements from Mg(0001) at 118 eV. Within the error bars, though, the results overlap. It is important to observe that the 118 eV data have been acquired at large acceptance angles. The dependence of the delay on acceptance angle and excitation energy will be discussed later in this chapter.

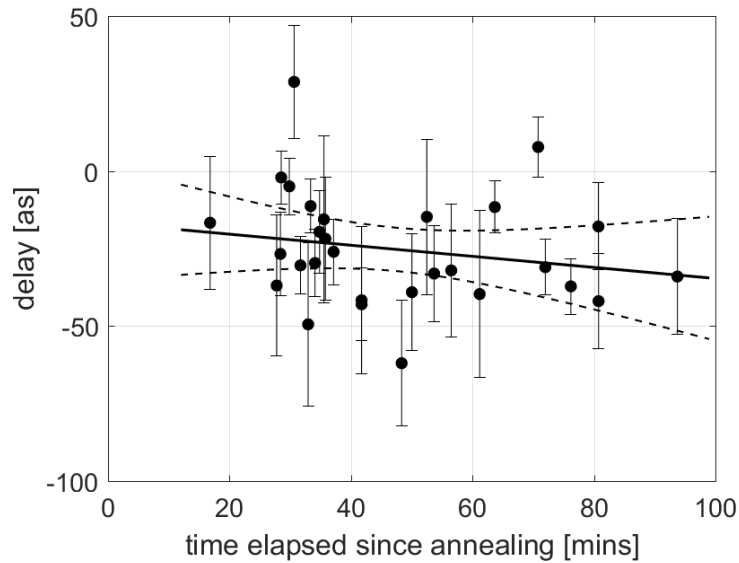


Figure 5.13: Mg(0001). (135 eV). Detection angle $\pm 2^\circ$. CB photoemission delay relative to $2p$ signal, as a function of time elapsed since film preparation.

It is also to be remarked that due to the high surface sensitivity of photoemission spectroscopy, preservation of a clean well-ordered surface during the streaking measurement is crucial. Here, this is a difficult task to achieve due to the high reactivity of magnesium in particular with oxygen. During the experiments, background pressures of less than 1×10^{-10} mbar have been maintained in the measurement chamber. Even under these generally good UHV conditions, a monolayer of atoms/molecules from the residual gas can adsorb on the surface within two hours

⁴This convention is consistent with those adopted by Refs. [2, 26, 115], which count a delay of the $2p$ electrons relative to the CB electrons as positive.

under the assumption of sticking coefficient equal to one. Therefore, the time window for streaking experiments is limited. The influence of contamination on the attosecond photoemission timing has been investigated before [3]. Motivated by these considerations, in this thesis the absence of significant influence of contamination from the residual gas on the delay result was demonstrated by evaluation of the photoemission delay as a function of elapsed time since last surface preparation. This dependence is displayed in Fig. 5.13. Here, the linear regression shows indeed no significant slope. Therefore, as long as the exposition time does not exceed the mentioned limit, significant influence of the exposition time on the delay is not observed. The maximum time for streaking experiments after surface preparation was strictly kept below two hours for all Mg(0001) experiments within this work, accordingly. In addition to the photoemission delay, the chirps of the outgoing photoelectron wave packets have been determined for both $2p$ and conduction band electrons.

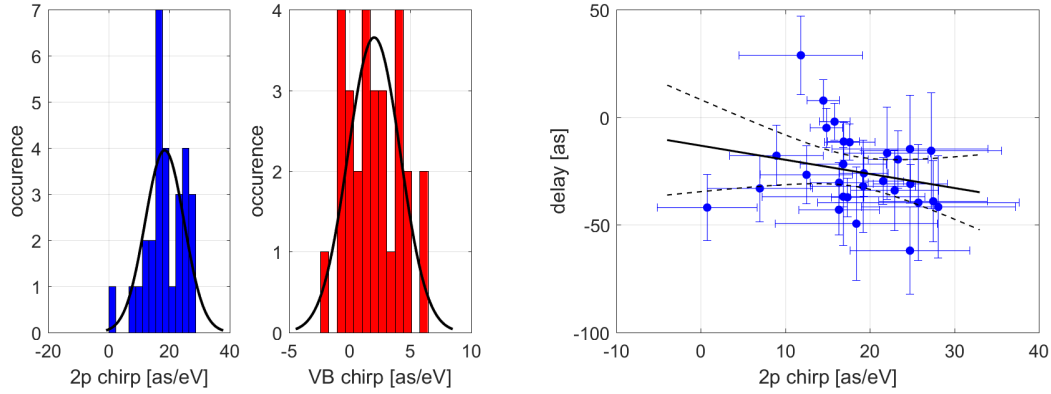


Figure 5.14: Mg(0001). (135 eV). Detection angle $\pm 2^\circ$. Left two panels: Statistical analysis of Mg $2p$ wave packet chirp (blue) and CB wave packet chirp (red). Results: (18 ± 7) as/eV and (2 ± 2) as/eV for $2p$ and CB wave packet, respectively. Right panel: $2p$ wave packet chirp vs. CB photoemission delay. 95%-confidence interval defined as described in caption of Fig. 4.10.

The chirps have been retrieved by assigning chirp fitting parameters to both wave packets independently. An overview of the chirp evaluation results is displayed in Fig. 5.14 below. A negative sign of the chirp in units of as/eV corresponds to a positive value in units of $1/\text{fs}^2$, i.e. that higher energies arrive later. The results of the chirps of both the $2p$ core state electron wave packets and the conduction band electron wave packets can be seen in the left two panels of Fig. 5.14. The retrieval yields a significant difference between the chirps of the two wave packets. This chirp difference will play a major role in the interpretation of the experimental

results and will be addressed in detail below. The evaluation of the delay as a function of the chirps and the conduction band chirp as a function of $2p$ chirp show no significant correlations. As a representative illustration of this finding, the correlation between Mg $2p$ chirp and CB photoemission delay, together with the linear regression model, is displayed in the right panel of Fig. 5.14. The demonstration of the absence of correlations is important in the light of previous work, where it was shown that non-negligible values for the chirp can lead to artifacts in the delay retrieval procedure [8].

Detection in wide acceptance angle

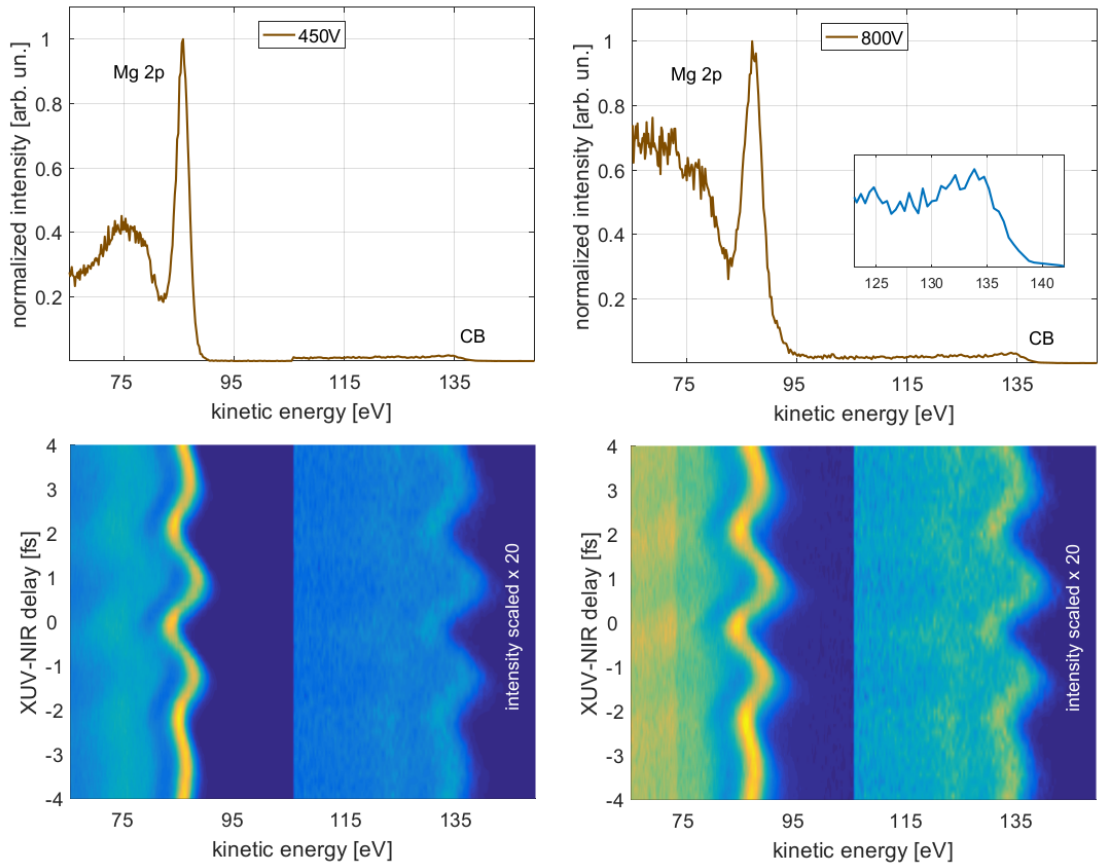


Figure 5.15: Mg(0001). (135 eV). Detection angle $\pm 20^\circ$. Upper panels: Stationary XUV + NIR spectra. Lower panels: streaking spectrograms. The left two panels correspond to a voltage of 450 V, and the right panels are obtained at 800 V.

From the one-dimensional theoretical framework of Ref. [26], resonant behavior of the photoemission delay of electrons ejected in normal emission is expected for XUV energies around 135 eV. In this range, also the synchrotron data presented above indicate a strong contribution to the CB photoemission signal coming from electrons emitted from deeper inside the bulk along the surface normal. This contribution should manifest itself in the photoemission time delays accessible in the streaking experiments. If the acceptance angle is large, however, the contribution is expected to average out, as will be discussed later in the chapter. It is reasonable to assume that if the streaking study presented above is repeated with considerably increased acceptance angle, this should leave traces in the measured photoemission timing. Thus motivated, a broad acceptance angle streaking study has been performed. The geometry of the just described narrow acceptance angle measurements was unaltered, but the acceptance angle itself was increased up to $\pm 20^\circ$ by the application of the electrostatic lens equipped to the TOF spectrometer. To obtain data with good quality, the switching technique which was devised in the course of this thesis and described in Ch. 3 was used for the first time. In Fig. 5.15, representative spectrograms are shown.

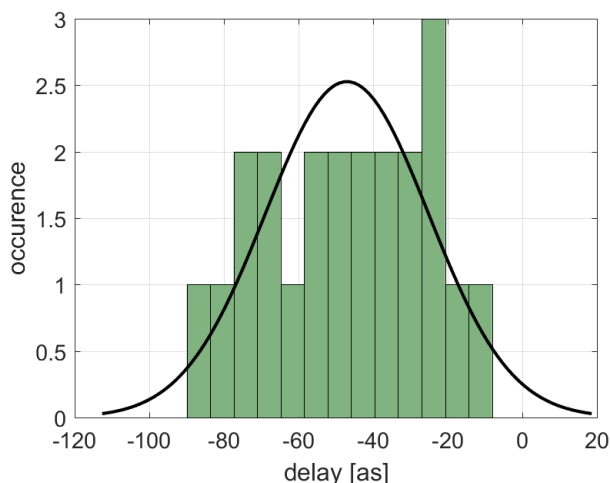


Figure 5.16: Mg(0001). (135 eV). Detection angle $\pm 20^\circ$. CB photoemission delay relative to the $2p$ signal. Black curve shows the normal distribution fit which results in an average delay value of -47 ± 22 as.

In the switching setting, the $2p$ spectral region was recorded with voltages of 440-480 V, at a voltage at the micro channel plates (MCP) of 1.8-1.9 kV. The conduction band region was recorded with voltages at 800-900 V, with MCP voltages around 2.2 kV. In this fashion, 22 streaking spectrograms have been acquired. The

data evaluation yields a delay result of -47 ± 22 as, as shown in Fig. 5.16.

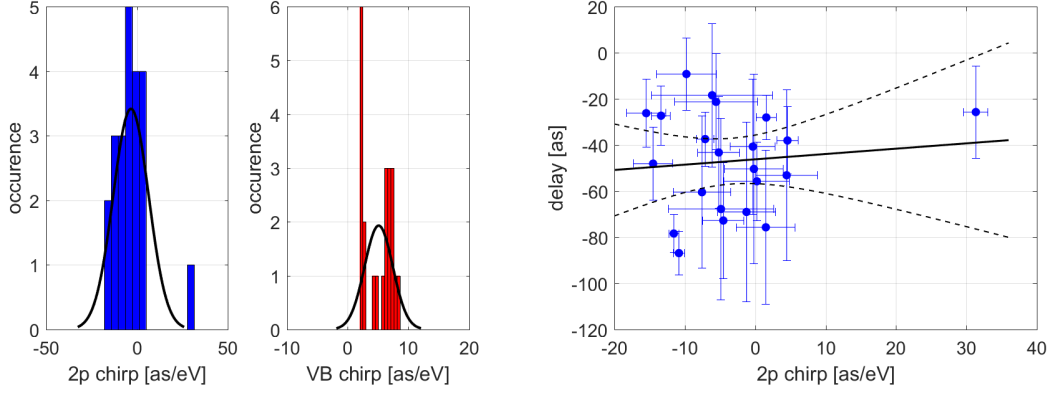


Figure 5.17: Mg(0001). (135 eV). Detection angle $\pm 20^\circ$. Left two panels: Statistical analysis of Mg 2*p* wave packet chirp (blue) and CB wave packet chirp (red). Results: (-3 ± 10) as/eV and (5 ± 2) as/eV for 2*p* and CB wave packet, respectively. Right panel: 2*p* wave packet chirp vs. CB photoemission delay. 95%-confidence interval defined as described in caption of Fig. 4.10.

Hence, for enlarged acceptance angle, an increase of the delay is indicated, by comparison with the average value of 25 as obtained in the narrow-angle study discussed before. The chirp analysis of the data set is presented in Fig. 5.17. Again, as in the $\pm 2^\circ$ measurements, there is a notable difference between 2*p* and CB wave packet chirps. In fact, the difference changes sign. The magnitude of the difference is negligible within error, though. The analysis shows no correlation between delay and chirps.

5.4.4 Streaking results at 145eV excitation energy

To obtain comparative data to the measurements taken at 135 eV, the experiments carried out at 135 eV were repeated with the excitation energy of 145 eV. For the measurement, an ion-beam-deposited chromium/scandium (Cr/Sc) multilayer mirror designed and manufactured by Alexander Guggenmos was used, which reflects attosecond pulses at 145 eV central energy with 3 eV FWHM [79]. The current stage of development of the FP3 femtosecond laser setup used throughout this experiment does not provide high XUV high-harmonic flux at 145 eV. It was not possible to take as many data as the case of 135 eV described above. Nevertheless, the statistics obtained still allows to draw the meaningful conclusions aimed for in this experiment.

Detection in narrow acceptance angle

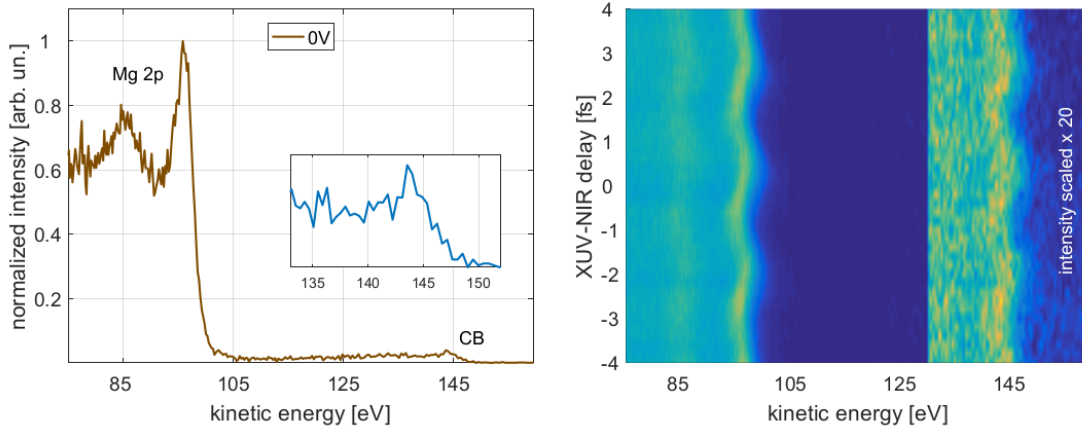


Figure 5.18: Mg(0001). (145 eV). Detection angle $\pm 2^\circ$. Left: Stationary XUV+NIR spectrum. Mg2p core state signal at 95 eV and first-order plasmon loss at 85 eV. The CB signal intensity was scaled for clarity. 0V legend entry refers to the default setting of the TOF spectrometer, which amounts to a detection angle $\pm 2^\circ$. Right panel: Streaking spectrogram.

In the narrow acceptance angle setting, 11 streaking spectrograms have been recorded. A representative spectrogram is shown in Fig. 5.18. The lower S/N ratio in the CB spectral region, as compared to the 135 eV experiment, is due to the lower XUV flux at 145 eV and to the lower ionization cross section of the CB at this energy.

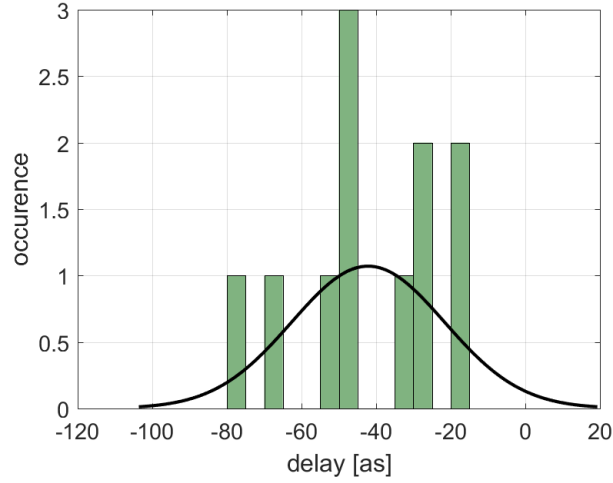


Figure 5.19: Mg(0001). (145 eV). Detection angle $\pm 2^\circ$. CB photoemission delay relative to the $2p$ signal. Black curve shows the normal distribution fit which results in an average delay value of -42 ± 20 as.

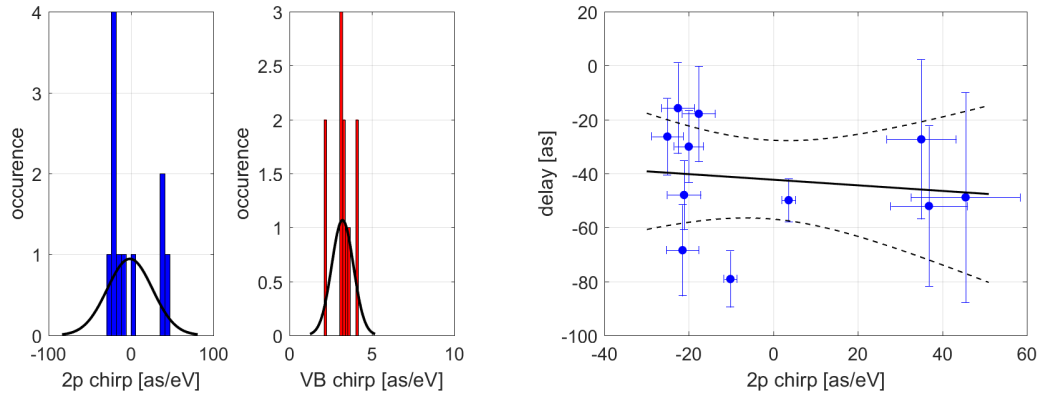


Figure 5.20: Mg(0001). (145 eV). Detection angle $\pm 2^\circ$. Left two panels: Statistical analysis of Mg $2p$ wave packet chirp (blue) and CB wave packet chirp (red). Results: (-2 ± 28) as/eV and (3 ± 1) as/eV for $2p$ and CB wave packet, respectively. Right panel: $2p$ wave packet chirp vs. CB photoemission delay. 95%-confidence interval defined as described in caption of Fig. 4.10.

The results for the delay and chirp analysis are shown in Fig. 5.19 and Fig. 5.20, respectively. The average relative CB photoemission delay is considerably larger than in the narrow-angle experiment at 135 eV. No significant difference between

the average values for the chirps of $2p$ electron and CB wave packets was found, again in contrast to the narrow acceptance angle study at 135 eV. These findings underline the conjecture drawn earlier in this chapter, as will be elucidated later.

Detection in wide acceptance angle

At the increased acceptance angle of up to $\pm 20^\circ$, a set of 16 streaking spectrograms has been obtained. A representative spectrogram is presented in Fig. 5.21

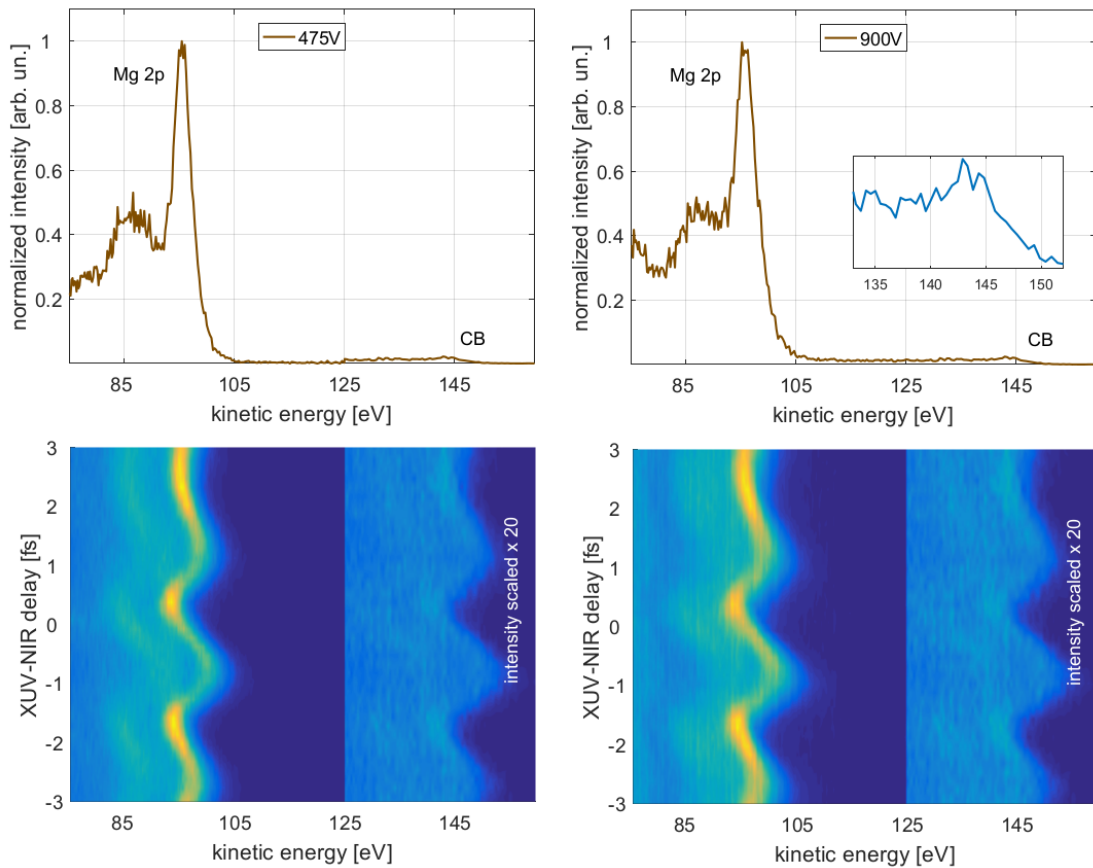


Figure 5.21: Mg(0001). (145 eV). Detection angle $\pm 20^\circ$. Upper panels: Stationary XUV + NIR spectra. Lower panels: streaking spectrograms. The left two panels correspond to a voltage of 475 V, and the right panels are obtained at 900 V.

In the acquisition of these data, the switching technique was applied. The voltage for the electrostatic lens was set to 450-500 V (800-900 V) for the even (odd) shots focussing at the $Mg2p$ (CB) spectral region. The results of the data processing is shown below.

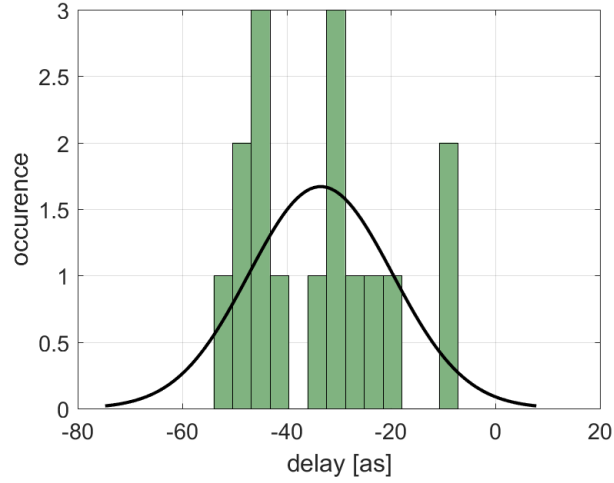


Figure 5.22: Mg(0001). (145 eV). Detection angle $\pm 20^\circ$. CB photoemission delay relative to the $2p$ signal. Black curve shows the normal distribution fit which results in an average delay value of -33 ± 14 as.

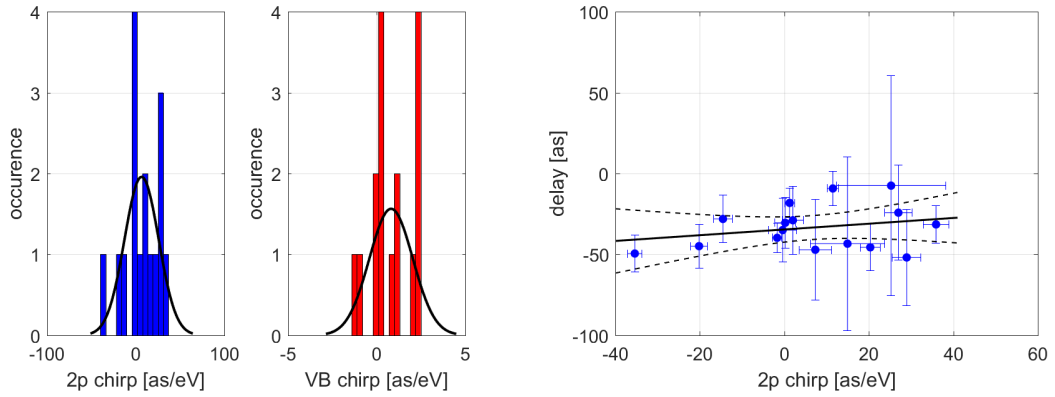


Figure 5.23: Mg(0001). (145 eV). Detection angle $\pm 20^\circ$. Left two panels: Statistical analysis of Mg $2p$ wave packet chirp (blue) and CB wave packet chirp (red). Results: (6 ± 19) as/eV and (1 ± 1) as/eV for $2p$ and CB wave packet, respectively. Right panel: $2p$ wave packet chirp vs. CB photoemission delay. 95%-confidence interval defined as described in caption of Fig. 4.10.

The delay statistics are presented in Fig. 5.22, and the chirp evaluation is illustrated in Fig. 5.23. The data show no significant difference to the data obtained for narrow acceptance angle at 145 eV, while there is a profound such difference

in the case of the 135 eV data sets. The average delay value of -33 as is smaller than for the narrow-angle experiment at 145 eV, but not distinguishable within error margins.

5.4.5 Discussion of the experimental results

Overall, a total of four distinct data sets have been acquired. Two of these four sets consist of streaking spectrograms recorded with 135 eV XUV attosecond pulses for both a narrow ($\pm 2^\circ$) and a broad ($\pm 20^\circ$) detection cone around the surface normal, the other two groups of spectrograms were taken at 145 eV for the narrow and broad cone, respectively. In the analysis of each of the four data bases, the photoemission delay of the conduction band signal with respect to the $2p$ core state signal has been retrieved, and the chirps of the electron wave packets emitted from both $2p$ states and conduction band states have been determined. The summary of the results of all four data sets is shown in Tab. 5.1 and Fig. 5.24.

XUV energy	angle	scans	delay	Mg2 <i>p</i> chirp	CB chirp
135 eV	$\pm 2^\circ$	29	(-25 \pm 18) as	(18 \pm 7) as/eV	(2 \pm 2) as/eV
135 eV	$\pm 20^\circ$	22	(-47 \pm 22) as	(-3 \pm 10) as/eV	(5 \pm 2) as/eV
145 eV	$\pm 2^\circ$	11	(-42 \pm 20) as	(-2 \pm 28) as/eV	(3 \pm 1) as/eV
145 eV	$\pm 20^\circ$	16	(-33 \pm 14) as	(6 \pm 19) as/eV	(1 \pm 1) as/eV

Table 5.1: Magnesium streaking results. XUV excitation energy, acceptance angle, CB photoemission delay relative to Mg2*p* signal, Mg2*p* wave packet chirp and CB wave packet chirp.

Tab. 5.1 summarizes all experimental results. In Fig. 5.24, the results are arranged such that the block of four plots in Fig. 5.24a and the block of four plots in Fig. 5.24b correspond to the results taken at 135 eV and 145 eV photon energy, respectively. Within both of these two blocks, the results obtained for narrow-angle are placed directly above the results for broad angle, to emphasize possible differences between the results for the two geometries. The delay plots show the time difference of the conduction band photoemission signal with respect to the $2p$ core state signal, and the chirp plots display the values of the conduction band wave packet chirps and the $2p$ wave packet chirps, respectively. In this fashion, a relative conduction band chirp can be introduced, by using the $2p$ wave packet as a reference value. This will be discussed further in the next subsection. From inspection of Fig. 5.24, several key results are apparent. First, in all of the four scenarios, the conduction band signal comes with a negative delay, which means

that the conduction band electrons are throughout emitted prior to the core state electrons, as predicted in Ref. [26].

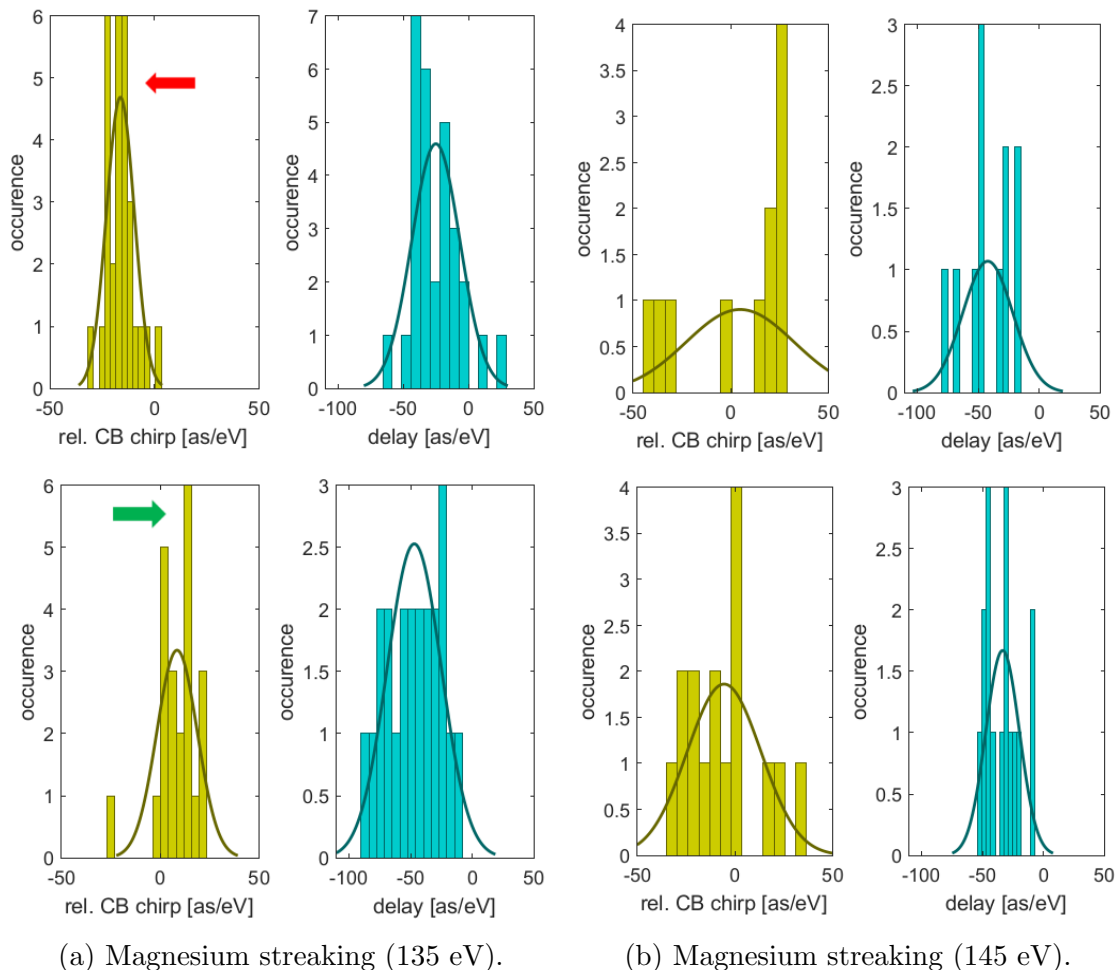


Figure 5.24: Magnesium streaking results. a) 135 eV. CB photoemission delay relative to the $\text{Mg}2p$ signal and and CB chirp relative to $2p$ chirp for narrow (upper panels) and broad acceptance cone (lower panels. b) Results for 145 eV, displayed according to a). Green (red) arrows indicate positive (negative) average values of the relative chirp, to highlight the dependence of this value on acceptance angle and photon energy.

Further, for the experiment conducted at 135 eV, changing the acceptance angle makes a considerable difference. The delay value is smaller for the narrow-angle, and the chirp difference is well negative for the narrow-angle scenario but comes out slightly positive upon increasing the acceptance cone. For the 145 eV measure-

ments, no such profound differences are found. The difference between the relative chirps in the narrow and broad situation is much smaller. Still, even though it is well within statistical error, it can be stated that the mean of the relative chirp changes signs in an opposite way to the 135 eV data. This effect is pictorially highlighted by the green and red arrows in Fig. 5.24. The summarized chirp result is displayed below in Fig. 5.25. As mentioned before, a negative value of retrieved chirp in units of as/eV corresponds to a time-frequency dependence of the wave packet which exhibits positive slope.

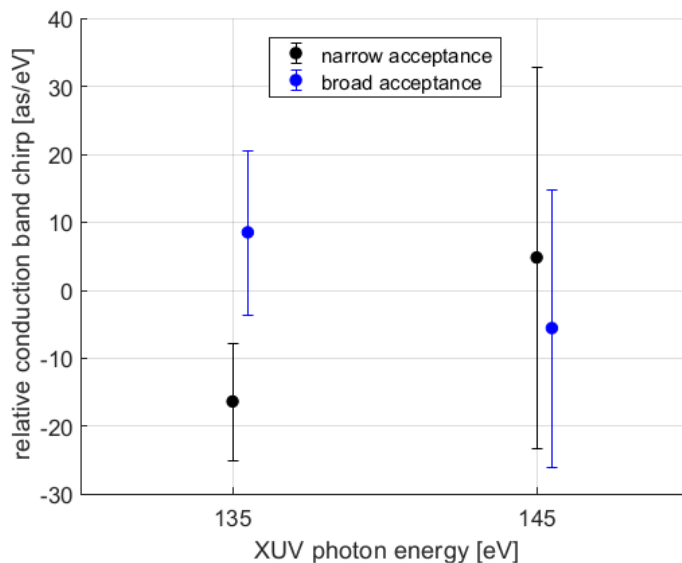


Figure 5.25: Mg(0001) streaking data. Chirp difference between conduction band and $2p$ core state wave packet chirps, obtained in narrow $\pm 2^\circ$ (black) and broad $\pm 2^\circ$ (blue) detection cones.

The large (small) chirp value in narrow (broad) acceptance angle measurement at 135 eV indicates a very different temporal structure of the conduction band photoemission for the two measurement sets. This result supports the conjecture that at 135 eV, a strong contribution to the signal comes from electrons which are excited "resonantly" deep into the bulk and thus are emitted later than those emitted directly from the surface, due to their propagation time to the surface-vacuum interface. Their contribution is expected large only for normal emission along the $\Gamma-A$ direction and would smear out in the case of large acceptance angle. The surface state contribution smears out as well, but its absolute contribution to the photoemission signal is small, as discussed before. In the case of 145 eV, this profound difference is absent, a finding which agrees with the expectation from the

synchrotron data analysis and the theoretical model. In fact, for the energy which is off the resonant value by 10 eV, it is reasonable to assume that the contribution from the resonant bulk emission is minor because vertical interband transitions are not as efficiently triggered at this energy. In Fig. 5.26, the delay results of the magnesium experiments are summarized.

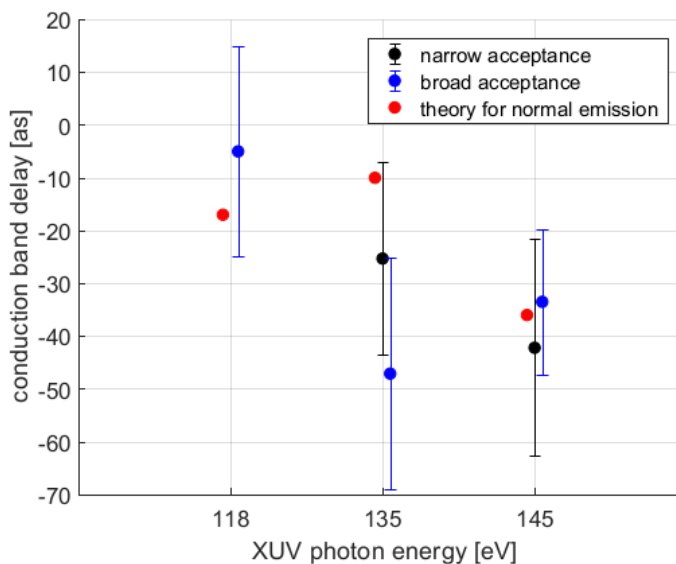


Figure 5.26: Mg(0001) streaking data. Delay of conduction band photoemission with respect to $2p$ core state emission. Comparison of the results acquired for broad (blue) and narrow (black) detection cones, to the theoretical predictions in Ref. [26] (red).

For direct comparison with the theoretical predictions in Ref. [26] and with prior experimental results on magnesium [2, 115], the corresponding values are shown in Fig. 5.26 together with the data obtained within this thesis. As apparent from this overview, the theoretical numbers (red) agree within statistical error with the narrow acceptance angle data (black) for both 135 eV and 145 eV. For the broad acceptance data, the agreement is clearly satisfactory for 118 eV and 145 eV, but not for 135 eV. This finding corroborates the hypothesis that the delay at 135 eV is very strongly affected by the resonant bulk emission in the $\Gamma - A$ direction, whereas this effect is negligible for energies well separated from this resonant value. Taken together, the experimental results and their comparison to the theoretical framework underline that band structure can play a major role in the forming of attosecond delays in photoemission from solids.

5.5 Conclusion

Magnesium streaking spectroscopy has been applied to Mg(0001) films deposited on W(110) at the XUV photon energies 135 eV and 145 eV, in order to study the temporal characteristics of the photoemission from Mg2*p* core level electrons and Mg conduction band electrons. The choice of the energy value 135 eV for the XUV pump photon energy was motivated by synchrotron data which show a very strong and rather sharp enhancement of the photoelectron yield in normal emission at ≈ 135 eV, and by theoretical calculations which predict a local minimum of the 2*p* core-level photoemission delay relative to the emission of the conduction band electrons at ≈ 135 eV. The 145 eV measurements were performed to obtain comparative data 10 eV beyond the resonance.

For both 135 eV and 145 eV, a significant number of streaking spectrograms has been acquired with detection axis parallel to the surface normal and with two different acceptance angles. For one part of the measurements, the angle was set to $\pm 2^\circ$, which amounts to the default value of the employed TOF spectrometer. For the other part of the scans, the angle was enlarged up to $\pm 20^\circ$ by application of voltages of several hundred volts in the electrostatic lens which is attached to the TOF spectrometer. For the measurements with larger acceptance angle, the switching technique was used, which was conceived in the course of this thesis. It allows switching both the electrostatic lens voltage and the voltage at the micro channel plates (MCP) in the detector for every shot of the laser (repetition rate 4 kHz), between two prescribed values. These values are chosen such that for every even shot, the Mg2*p* core state signal is recorded in good quality while the conduction band spectrum is only acquired with weak signal, and for every odd shot, the conduction band signal is recorded in good quality at expense of the distortion of the Mg2*p* spectrum by strong saturation. This way, two spectrograms are acquired from the odd and even shots, respectively. In the data processing after the measurement, the good quality parts of both even and odd spectrogram are merged into one spectrogram and evaluated by the standard retrieval methods. As a result, good signal-to-noise ratios were achieved in the absence of saturation effects.

The evaluation of the data set acquired at 135 eV XUV energy showed a remarkable difference between the delays obtained for broad and narrow acceptance cones. Specifically, the delay of the Mg2*p* core state emission with respect to the conduction band emission is smaller for the narrow acceptance measurements. This result agrees well with conclusions drawn from the synchrotron data and the theoretical model discussed earlier in this chapter, according to which the contribution from electrons from deep inside the bulk to the overall conduction band signal is strong

only in $\Gamma - A$ direction, i.e. parallel to the surface normal. The weight of these electrons is much larger for measurements with small acceptance angle and their influence smears out in large acceptance angle measurements. The chirp evaluation of these data set showed a large relative chirp of the conduction band wave packets for the narrow acceptance angle study, but only a marginal relative chirp in the broad acceptance angle data. This finding is also consistent with the reasoning above because chirp describes the time-frequency dependence of the wave packet, and hence a large chirp is a signature of contributions to the wave packet which are emitted at different times. Conversely, at 145 eV both the pronounced chirp difference and delay difference seen in the 135 eV data are absent. For the narrow acceptance angle measurements, the Mg2*p* core state emission delay is smaller for 135 eV, in accordance with the conjectures drawn earlier in this chapter. Importantly, for both 135 eV and 145 eV, the narrow acceptance angle results agree well with the theoretical predictions in Ref. [26]. The results of the magnesium experiment performed in this thesis provide strong evidence for an influence of band structure effects on the photoemission timing from metals, a major achievement in this context.

It is recommended to carry out measurements at other photon energies in this energy range, to check the accuracy of the theoretical predictions. In general, further investigation of the possible influence of band structure effects in other materials is envisaged, and in this context, angle-resolved streaking spectroscopy is particularly promising as a natural improvement of the approach followed in this thesis.

Chapter 6

Summary and Outlook

The presented work was designed to further improve the understanding of the time evolution of photoemission from solids. The major goal was the investigation of possible band structure influence on the photoemission timing at high final-state energies. The main content of this thesis is formed by experimental work on the condensed matter systems highly-oriented pyrolytic graphite (HOPG) and magnesium. Attosecond streaking spectroscopy was performed on both systems and the obtained results were discussed, interpreted, and compared to recent theoretical work.

For the two XUV photon energies 93 eV and 112 eV, streaking spectrograms have been acquired from the HOPG valence band. For these energies, the valence band spectrum exhibited two partially resolved peaks. Characteristics of these two spectral contributions could be deduced from X-ray photoemission spectroscopy (XPS), X-ray emission spectroscopy (XES) data and band structure considerations. The spectral density in the lower binding energy peak was shown to predominantly arise from the photoemission of electrons from C2*p*-derived electronic states (P peak), while the spectral feature at higher binding energy was shown to be mainly due to emission from C2*s*-derived states (S peak). In the evaluation of the obtained streaking data, the relative timing between the signals corresponding to the two peaks was measured. A significant delay of ≈ 30 as was found in the emission of the P peak electrons with respect to the S peak electrons. This result could be quantitatively interpreted with the help of theoretical work [41]. In this model, the observed delay is discussed in terms of the combined influences of two effects: The group velocity dispersion on the one hand, and the Eisenbud-Wigner-Smith (EWS) delay which the photoelectron acquires upon its transport through the graphite layers on the other hand.

In a related study conducted in this thesis, two-dimensional nanoclusters of tungsten were successfully prepared on HOPG. This demonstrates the possibility to study two-dimensional tungsten systems in the future to disentangle propagation effects from the various causes of the photoemission timing delays in this material. Within this thesis as well, a strong experimental contribution was made towards achieving optimum spectral resolution in attosecond streaking. Streaking was successfully carried out on gallium arsenide and tungsten at 112 eV at a spectral width of the attosecond pulses of 1.8 eV (FWHM) [44, 45]. Furthermore, work contributed within the period of this thesis helped to pave the way towards absolute photoemission timing, by using iodine adatoms adsorbed on tungsten as a reference clock [43]. Contribution was also made to the acquisition of attosecond streaking data at 112 eV and 135 eV on tungsten, which form a significant part of a streaking data basis for this material at varying excitation energy [46].

Motivated by synchrotron data and theoretical calculations of the photoemission delays in magnesium, streaking measurements have been carried out on this free-electron-like metal at the XUV photon energies of 135 eV and 145 eV. For the measurements at 145 eV, an XUV mirror was used which was built in a new design based on chromium/scandium multilayers [79]. Streaking data sets have been obtained for both energies for narrow ($\pm 2^\circ$) as well as broad ($\pm 20^\circ$) acceptance angles. By a careful chirp and delay analysis in all these four data sets and by comparison of these results to the theoretical considerations in Ref. [26], strong evidence of band structure influence on the measured delays was found.

The work in this thesis thus gives further insight into the dynamics of the photoemission process in solids in the time domain. It strongly indicates that band structure plays a significant role in forming of the observed photoemission delays measured in magnesium and HOPG. For future studies, it is particularly recommended to pursue angle-resolved streaking spectroscopy to further quantify band structure influences on the photoemission timing. Certainly, for high XUV energies such as achieved in this work, the technique is yet severely limited by the low photon flux. However, the continuation of the effort in laser system optimization will hopefully allow setting this promising approach to work soon.

Bibliography

- [1] A.L. Cavalieri et al. “Attosecond spectroscopy in condensed matter”. *Nature* 449 (2007).
- [2] S. Neopl. “Attosecond Time-Resolved Photoemission from Surfaces and Interfaces”. *PhD Thesis, Technical University Munich* (2012).
- [3] M. Gerl. “Time-resolved investigation of photoelectron dynamics by Attosecond Streaking Spectroscopy on solids”. *Master’s thesis, Technical University Munich* (2013).
- [4] C. Chen et al. “Distinguishing attosecond electron–electron scattering and screening in transition metals”. *Proc. Nat. Academy of Sciences of the U.S.* 114, 27 (2017).
- [5] Z. Tao et al. “Direct time-domain observation of attosecond final-state lifetimes in photoemission from solids”. *Science, publ. online* (2016).
- [6] R. Locher et al. “Energy-dependent photoemission delays from noble metal surfaces by attosecond interferometry”. *Optica* 2, 5 (2015).
- [7] F. Siek et al. “Angular momentum–induced delays in solid-state photoemission enhanced by intra-atomic interactions”. *Science* 357, 6357 (2017).
- [8] A. Kim. “Attosecond time-resolved photoemission from solid samples”. *PhD Thesis, Technical University Munich* (2015).
- [9] M. Jobst. “Attosecond Dynamics in Molecules and on Interfaces”. *PhD Thesis, Technical University Munich* (2014).
- [10] M. Fanciulli et al. “Spin Polarization and Attosecond Time Delay in Photoemission from Spin Degenerate States of Solids”. *Phys. Rev. Lett.* 118, 067402 (2017).
- [11] j. Li, E. Saydanzad, and U. Thumm. “Attosecond time-resolved streaked photoelectron spectroscopy of transition-metal nanospheres”. *Physical Review A* 95, 043423 (2017).
- [12] J. Schötz. “Attosecond Experiments on Plasmonic Nanostructures”. *Best-Masters. Springer Spektrum, Wiesbaden* (2016).

- [13] M. Nisoli et al. “Attosecond Electron Dynamics in Molecules”. *Chem. Rev.*, 2017, 117 (16) (2017).
- [14] M. Drescher et al. “Time-resolved atomic inner-shell spectroscopy”. *Nature* 419 (2002).
- [15] M. Schultze et al. “Delay in Photoemission”. *Science* 328, 5986, 1658-1662 (2010).
- [16] M. Sabbar et al. “Resonance Effects in Photoemission Time Delays”. *Phys. Rev. Lett* 115, 133001 (2015).
- [17] B. Manschwetus et al. “Two-photon double ionization of neon using an intense attosecond pulse train”. *Phys. Rev. A* 93, 061402 (2016).
- [18] A.J. Verhoef et al. “Attosecond streaking of shake-up and Auger electrons in xenon”. *EPJ Web of Conferences* 41 02003 (2013) (2013).
- [19] M. Ossiander et al. “Attosecond correlation dynamics”. *Nature Physics* 13, 280 (2016).
- [20] C. Palatchi et al. “Atomic delay in helium, neon, argon and krypton”. *Journal of Physics B: Atomic, Molecular and Optical Physics* 47, 24 (2014).
- [21] C.-H. Zhang and U. Thumm. “Effect of wave-function localization on the time delay in photoemission from surfaces”. *Physical Review A* 84 (2011).
- [22] Q. Liao and U. Thumm. “Attosecond time-resolved streaked photoemission from Mg-covered W(110) surfaces”. *Phys. Rev. A* 92, 031401 (2015).
- [23] S. Naegele et al. “Time-resolved photoemission by attosecond streaking: extraction of time information”. *Journal of Physics B: Atomic , Molecular and Optical Physics*, 44, 8 (2011).
- [24] E.E. Krasovskii. “Attosecond spectroscopy of solids: streaking phase shift due to lattice scattering”. *Physical Review B* 84, 19 (2011).
- [25] E.E. Krasovskii, C. Friedrich, and P.M. Schattke W.and Echenique. “Rapid propagation of a Bloch wave packet excited by a femtosecond ultraviolet pulse”. *Physical Review B* 94, 19 (2016).
- [26] A. G. Borisov et al. “Resonant and nonresonant processes in attosecond streaking from metals”. *Physical Review B* 87 (2013).
- [27] J. Feist et al. “Time delays for attosecond streaking in photoionization of neon”. *Phys. Rev. A* 89, 033417 (2014).
- [28] R. Kienberger et al. “Atomic transient recorder”. *Nature* 427 (2004).
- [29] J. Itatani et al. *Phys. Rev. Lett.* 88 173903 (2002).
- [30] M. Hentschel et al. “Attosecond metrology”. *Nature* 414, 6863 (2001).

- [31] P. Eckle et al. “Attosecond angular streaking”. *Nature Physics* 4 (2008).
- [32] L. Castiglioni et al. “Attosecond Transversal Streaking to Probe Electron Dynamics at Surfaces”. *Yamanouchi K., Katsumi M. (eds) Multiphoton Processes and Attosecond Physics. Springer Proceedings in Physics, vol 125. Springer, Berlin, Heidelberg* (2012).
- [33] L. Cattaneo et al. “Comparison of attosecond streaking and RABBITT”. *Optics Express* 24, 25 (2016).
- [34] P.M. Paul et al. “Observation of a train of attosecond pulses from high harmonic generation”. *Science* 292, 5522 (2001).
- [35] H.G. Muller. “Reconstruction of attosecond harmonic beating by interference of two-photon transitions”. *Phys. B.* 74, S1 (2002).
- [36] R. Pazourek, S. Nagele, and J. Burgdörfer. “Attosecond chronoscopy of photoemission”. *Reviews of Modern Physics* 87 (2015).
- [37] F. Calegari et al. “Advances in attosecond science”. *J. Phys. B: Atom. Mol. Opt. Phys.* 49, 062001-1-27 (2016).
- [38] A.G. Borisov, A.K. Kazansky, and J.P. Gauyacq. “Finite Time Effect in the Charge Transfer Process during a Ion-Metal Surface Collision”. *Physical Review Letters* 80, 9 (1998).
- [39] A.G. Borisov, A.K. Kazansky, and J.P. Gauyacq. “Resonant charge transfer in ion-metal surface collisions: Effect of a projected band gap in the H⁻-Cu(111) system”. *Physical Review B* 59, 16 (1999).
- [40] A.R. Canario et al. “Nonadiabatic effects in atom-surface charge transfer”. *Physical Review B* 71, 121401 (2005).
- [41] Ch. Lemell. “private communication” (2017).
- [42] P. Feulner and S. Neupl. *private communication* (2015).
- [43] M. Ossiander et al. “Towards the Absolute Timing of Photoemission from Condensed Matter Systems”. *Conference Paper, International Conference on Ultrafast Phenomena* (2014).
- [44] A. Guggenmos et al. “Attosecond photoelectron streaking with enhanced energy resolution for small-bandgap materials”. *Optics Letters*, 3714 Vol.41 No.16 (2016).
- [45] A. Guggenmos et al. “Attosecond Electron Streaking with Enhanced Energy Resolution”. *Conference Paper, CLEO* (2016).
- [46] M. Jobst et al. “Excitation Energy Dependent Attosecond Photoemission Timing in Tungsten”. *Conference Paper, CLEO* (2015).

- [47] R.W. Wood. “A new form of Cathode Discharge and the Production of X-Rays, together with some Notes on Diffraction”. *Phys. Rev.* 5, 1 (1897).
- [48] A. McPherson et al. “Studies of multiphoton production of vacuum-ultraviolet radiation in the rare gases”. *J. Opt. Soc. Am. B* 4 (1987).
- [49] P.B. Corkum. “Plasma perspective on strong field multiphoton ionization”. *Physical Review Letters* 71 (1993).
- [50] M. Lewenstein et al. “Theory of high-harmonic generation by low-frequency laser fields”. *Physical Review A* 49 3 (1994).
- [51] P. Salieres et al. *J.Phys.B* 27 L217 (1994).
- [52] P. Salieres et al. *J.Phys.B* 29 4771 (1996).
- [53] S. Ghimire et al. “Observation of high-order harmonic generation in a bulk crystal”. *Nature Phys.* 7, 138-141 (2011).
- [54] S. Ghimire et al. “Strong-field and attosecond physics in solids”. *J. Phys. At. Mol. Opt. Phys.* 47, 204030 (2014).
- [55] O. Schubert et al. “Sub-cycle control of terahertz high-harmonic generation by dynamical Bloch oscillations”. *Nature Photon.* 8, 119 (2014).
- [56] G. Ndabashimiye et al. “Solid-state harmonics beyond the atomic limit”. *Nature* 534, 520 (2016).
- [57] H. Liu et al. “High-harmonic generation from an atomically thin semiconductor”. *Nature Phys.* 13, 262 (2017).
- [58] G. Vampa et al. “Theoretical analysis of high-harmonic generation in solids”. *Phys. Rev. Lett.* 113, 073901 (2014).
- [59] C.R. McDonald et al. “Interband Bloch oscillation mechanism for high-harmonic generation in semiconductor crystals”. *Phys. Rev. A* 92, 033845 (2015).
- [60] G. Vampa et al. “Semiclassical analysis of high harmonic generation in bulk crystals”. *Phys. Rev. B* 91, 064302 (2015).
- [61] T. Higuchi, M.I. Stockman, and P. Hommelhoff. “Strong-Field Perspective on High-Harmonic Radiation from Bulk Solids”. *Phys. Rev. Lett.* 113, 213901 (2014).
- [62] D. Golde, T. Meier, and S.W. Koch. “Microscopic analysis of high-harmonic generation in semiconductor nanostructures”. *Phys. Status Solidi C* 6, 420 (2009).
- [63] J. Itatani et al. “Attosecond streak camera”. *Physical Review Letters* 88 173903 (2002).

- [64] M. Kitzler et al. *Phys. Rev. Lett.* *88* 173904 (2002).
- [65] F. Quere, Y. Mairesse, and J. Itatani. *J. Mod. Opt.* *52* 339 (2005).
- [66] D.M. Volkow. *Zeitschrift für Physik A94* 250 (1935).
- [67] C.N. Berglund and W.E. Spicer. “Photoemission Studies of Copper and Silver: Theory”. *Phys. Rev.* *136* A1030 (1964).
- [68] A. Zangwill. “Physics at Surfaces”. *Cambridge University Press* (1988).
- [69] S. Neppl et al. “Direct observation of electron propagation and dielectric screening on the atomic length scale”. *Nature* *517* (2015).
- [70] E. Zaremba and W. Kohn. “Van der Waals interaction between an atom and a solid surface”. *Physical Review B*, *13*, 6 (1976).
- [71] E.M.L. Bothschafter. “Femtosecond and Attosecond Electron Dynamics in Semiconductors and Dielectrics”. *PhD Thesis, Technical University Munich* (2014).
- [72] H.W. Schweinberger. “A Laser Source for the Generation of Intense Attosecond Pulses and its First Applications”. *PhD Thesis, Ludwig-Maximilians-Universität München* (2014).
- [73] T. Fuji et al. “Attosecond control of optical waveforms”. *New Journal of Physics* *7* Nr.1 (2005).
- [74] D. Strickland and G. Mourou. “Compression of amplified chirped optical pulses”. *Opt. Commun.* *55.6*, pp. 447–449 (1985).
- [75] T. Clausnitzer et al. “Highly efficient transmission gratings in fused silica for chirped-pulse amplification systems”. *Appl. Opt.* *42.34* (2003).
- [76] F. Lücking et al. “Long-term carrier-envelope-phase-stable few-cycle pulses by use of the feed-forward method”. *Optics letters* *37*, Nr. 11 (2012).
- [77] E. Magerl et al. “A flexible apparatus for attosecond photoelectron spectroscopy of solids and surfaces”. *Review of Scientific Instruments* *82*, 063104 (2011).
- [78] E. Magerl. “Attosecond photoelectron spectroscopy of electron transport in solids”. *PhD Thesis, Technical University Munich* (2011).
- [79] A. Guggenmos et al. “Chromium/scandium multilayer mirrors for isolated attosecond pulses at 145 eV”. *Optics Letters*, *2846* Vol.40 No.12 (2015).
- [80] A. Guggenmos et al. “Ion polished Cr/Sc attosecond multilayer mirrors for high water window reflectivity”. *Optics Express*, *22*, 22 (2014).

- [81] L.M. Fellingner. “Photoemissionsmessungen der Elektronen-Transportdynamik in Metallen mit Attosekunden-Zeitauflösung: Entwicklung und Test einer Methode zur Unterdrückung magnetischer Störfelder”. *Master’s thesis, Technical University Munich* (2016).
- [82] D. Shirley. “High-Resolution X-Ray Photoemission Spectrum of the Valence Bands of Gold”. *Phys. Rev. B* 5.12 (1972).
- [83] M. Ossiander. “On the Expansion of Attosecond Streaking Spectroscopy towards Ultrafast Surface Dynamics”. *Master’s thesis, Technical University Munich* (2014).
- [84] G. Binnig et al. “Tunneling through a controllable vacuum gap”. *Appl. Phys. Lett.*, vol. 40, pp. 178–180 (1982).
- [85] G. Binnig et al. “Surface studies by scanning tunneling microscopy”. *Phys. Rev. Lett.*, vol. 49, pp. 57–61 (1982).
- [86] A. Selloni et al. “Voltage-dependent scanningtunneling microscopy of a crystal surface: Graphite”. *Phys. Rev. B*, vol. 31, pp. 2602–2605 (1985).
- [87] A.C. Wiengarten. “Scanning tunneling microscopy investigation of structure and electronic properties of surface-confined tetrapyrrolic species”. *PhD Thesis, Technical University Munich* (2015).
- [88] IUPAC. “Highly oriented pyrolytic graphite”. *Compendium of Chemical Terminology, 2nd ed. (the ”Gold Book”)* (1997).
- [89] A.W. Moore. “Highly oriented pyrolytic graphite”. *Chemistry and physics of carbon*. 11 (1973).
- [90] S. Hembacher et al. “Revealing the hidden atom in graphite by low-temperature atomic force microscopy”. *Proc. Natl. Acad. Sci.* 100, 12539 (2003).
- [91] T. Takahashi, H. Tokailin, and T. Sagawa. “Angle-resolved ultraviolet photoelectron spectroscopy of the unoccupied band structure of graphite”. *Physical Review B*, 32, 8317 (1985).
- [92] L.C.F. Blackman and A.R. Ubbelohde. “Stress Recrystallization of Graphite”. *Proceedings of the Royal Society of London*. A266 (1962).
- [93] R.V. Lapshin. “Automatic lateral calibration of tunneling microscope scanners”. *Review of Scientific Instruments*. USA: AIP. 69 (9) (1998).
- [94] R.V. Lapshin. “Drift-insensitive distributed calibration of probe microscope scanner in nanometer range: Approach description”. *Applied Surface Science*. Netherlands: Elsevier B. V. 359 (2015).
- [95] I.P. Dolbnya et al. “Focusing parabolic pyrolytic graphite X-ray monochromator”. *Nucl. Instr. Meth.*, Vol. A359 (1995).

- [96] A.B. Djurisić and E. Herbert Li. “Optical properties of graphite”. *Journal of Appl. Physics*, 85, 10 (1999).
- [97] G. E. Jellison, J. D. Hunn, and H.N. Lee. “Measurement of optical functions of highly oriented pyrolytic graphite in the visible”. *Phys. Rev. B* 76, 085125 (2007).
- [98] S. Tanuma et al. “Experimental determination of electron inelastic mean free paths in 13 elemental solids in the 50 to 5000 eV energy range by elastic-peak electron spectroscopy”. *Surf. Interface Anal.* 2005, 37, 833–845 (2005).
- [99] J Parker and C. W. Clark. “Study of a plane-wave final-state theory of above-threshold ionization and harmonic generation”. *Journal of Opt. Soc. Am.*, 13(2), 271 (1996).
- [100] Emma Louise Catton. “Photoelectron Spectroscopy of Highly Oriented Pyrolytic Graphite using Intense Ultrashort Laser Pulses”. *PhD Thesis, University of Birmingham* (2010).
- [101] J. Kanasaki et al. “Formation of sp^3 -Bonded Carbon Nanostructures by Femtosecond Laser Excitation of Graphite”. *Phys. Rev. Lett.* 102, 087402 (2009).
- [102] A.M. Beltaos et al. “Femtosecond laser induced periodic surface structures on multi-layer graphene”. *Journal of Applied Physics* 116, 204306 (2014).
- [103] A. Bianconi, S.B.M. Hagström, and R.Z. Bachrach. “Photoemission studies of graphite high-energy conduction-band and valence-band states using soft-x-ray synchrotron radiation excitation”. *Physical Review B* 16 (1977).
- [104] K. Endo et al. “Analysis of XPS and XES of Diamond and Graphite by DFT Calculations Using Model Molecules”. *Journal of Computational Chemistry* 22(1), 102-108 (2001).
- [105] P. Hohenberg and W. Kohn. “Inhomogeneous Electron Gas”. *Phys. Rev.* 136, B864 (1964).
- [106] W. Kohn and L.J. Sham. “Self-Consistent Equations Including Exchange and Correlation Effects”. *Phys. Rev.* 140, A1133 (1965).
- [107] R.G. Parr and W. Yang. “Density-Functional Theory of Atoms and Molecules”. *New York: Oxford University Press. ISBN 0-19-504279-4* (1989).
- [108] C. Lechner et al. “First-Principles Study of the Structural, Electronic, Dynamic, and Mechanical Properties of HOPG and Diamond: Influence of Exchange-Correlation Functionals and Dispersion Interactions”. *J. Phys. Chem. C* 2016, 120, 5083-5100 (2016).

- [109] Hae Kyung Jeong et al. “Valence band of graphite oxide”. *EPL* 92 (2001).
- [110] S. Tanuma, C.J. Powell, and D.R. Penn. “Calculations of electron inelastic mean free paths. V. Data for 14 organic compounds over the 50–2000 eV range”. *Surf.Int.Anal.* 21, 3 (1994).
- [111] L. Eisenbud. “Formal properties of nuclear collisions”. *Ph.D. thesis, Princeton University* (1948).
- [112] E.P. Wigner. “Lower Limit for the Energy Derivative of the Scattering Phase Shift”. *Phys. Rev.* 98,1,145 (1955).
- [113] F.T. Smith. “Lifetime Matrix in Collision Theory”. *JPhys. Rev.* 118,1,349 (1960).
- [114] David Duncan. *private communication* (2015).
- [115] S. Neppel et al. “Attosecond Time-Resolved Photoemission from Core and Valence States of Magnesium”. *Physical Review Letters* 109 (2012).
- [116] U.O. Karlsson et al. “Surface electronic structure of Mg(0001)”. *Phys. Rev. B* 26, 1852 (1982).
- [117] F. Schiller et al. “Surface State Scattering at a Buried Interface”. *Phys. Rev. Lett.* 95, 126402 (2005).
- [118] F. Schiller and C. Laubschat. “Surface states at close-packed surfaces of simple metals”. *Phys. Rev. B* 74, 085109 (2006).
- [119] R. A. Bartynski et al. “Angle-resolved photoemission study of the surface and bulk electronic structure of Mg(0001) and Mg(112-0)”. *Phys. Rev. B* 33, 3644 (1986).
- [120] E. Jensen et al. “Angle-resolved photoemission study of the electronic structure of beryllium: Bulk band dispersions and many-electron effects”. *Phys. Rev. B* 30, 5500 (1984).
- [121] Ph. Hofmann et al. “Unexpected surface sensitivity at high energies in angle-resolved photoemission”. *Phys. Rev. B* 66 (2002).
- [122] N.W. Ashcroft and N.D. Mermin. “Solid State Physics”. *Holt, Rinehart and Winston* (1976).
- [123] F. Schiller et al. “Electronic structure of Mg: From monolayers to bulk”. *Phys. Rev. B* 70, 125106 (2004).
- [124] T.K. Kim et al. “Electron-phonon coupling on the Mg(0001) surface”. *Phys. Rev. B* 72, 075422 (2005).
- [125] The value for the Mg 2p binding energy was obtained as an average of the numbers given in the NIST data base: <https://srdata.nist.gov/xps/> (2017).

Acknowledgements

My deep gratitude goes to my doctoral advisor Johannes V. Barth for the opportunity to conduct this thesis at his chair and for his steady support and fruitful discussions. I am very grateful to Ferenc Krausz and Reinhard Kienberger for the opportunity to conduct the attosecond experiments presented in this thesis at the attosecond beamline AS 3. I am indebted to a very large measure to Peter Feulner and Francesco Allegretti for countless inspiring and fruitful discussions, continuous support and in particular for their strong backing in the final period of this work.

Many thanks to Stefan Neppl and Michael Gerl, who introduced me to the tricks and intricacies at the AS 3 beamline in the early stage of this thesis. I am especially grateful to Johann Riemensberger, a colleague of significant personal integrity, dedication and talent, for the strong and productive cooperation during all experiments conducted in the course of this thesis. Many thanks to Marcus Ossiander, Michael Jobst, Ayman Akil, Sebastian Jarosch and Maximilian Schnitzenbaumer for their profound contributions to the streaking experiments which were conducted in a continuously positive, funny and motivating working atmosphere. I would like to thank Alissa Wiengarten and Carlos-Andres Palma for their support in the STM study, Lisa Bothschafter, Wolfgang Schweinberger, Nick Karpowicz, Clemens Jakubeit and Annkathrin Sommer for their strong aid on the femtosecond laser tuning and optimization and Alexander Guggenmos for fabricating the high-quality XUV mirrors used in the streaking experiments. I would like to thank the theoreticians Andrey Kazansky and Christoph Lemell for many fruitful discussions and their very significant contribution to the magnesium and HOPG experiment, respectively. Many thanks to Reinhold Schneider, Karl Eberle and Karl Kölbl for their valuable technical support on countless occasions. My sincere gratitude goes to Peter Feulner, whose vast and sharp experimental expertise was of inestimable value in the realization of all the conducted experiments.

For their love, their trust and their constant support, I would like to thank my dear parents Petra and Helmut, my brother Thomas and my girlfriend Ravenn from the bottom of my heart. I dedicate this thesis to them.